Flexible Light-Emitting Diode Application of Polyfluorene-based Conjugated Polymers

A Dissertation for the Degree of Doctor of Philosophy

Dai-Hua, Jiang

National Taiwan University and Hokkaido University (Double Degree Program)

September 2021 (Hokkaido University)

Contents

Chapter 1

General Introduction

1.1 Fundamental Principle of Light-Emitting Diode (LED)

1.1.1 The basic light-emitting principle of LED

In the simplest terms, a light-emitting diode (LED) is a semiconductor device that emits light when an electric current is flowing through it. Currently, LEDs are the latest development in the lighting industry. Made popular by their efficiency, range of color, and long lifetime, LED lights are ideal for numerous applications including night lighting, art lighting, and outdoor lighting. To further comprehend the LED fundamental principle, the basic LED architecture and function of each layer are essential objects to know. Typically, the LED architecture is based on sandwich structure, in which the hole transport layer (HTL), electron transport layer (ETL), and sandwich light-emitting layer (EML), as shown in **Figure 1.1**. The right and left parts are the negative (cathode) and positive (anode) electrodes, respectively. The anode is composed of a transparent or semi-transparent conductor, generally using indium tin oxide (ITO) (4.8 eV) with a high work function; the cathode is usually composed of a metal or alloy with a low work function, such as silver (Ag) (4.3 eV), aluminum (Al) (4.3 eV), indium (In) (4.1 eV), magnesium (Mg) (3.7eV), lithium (Li) (2.9 eV), and calcium (Ca) (2.9eV). From left to right, there is the hole transport layer (HTL), light-emitting layer (EML), an electron transport layer (ETL).

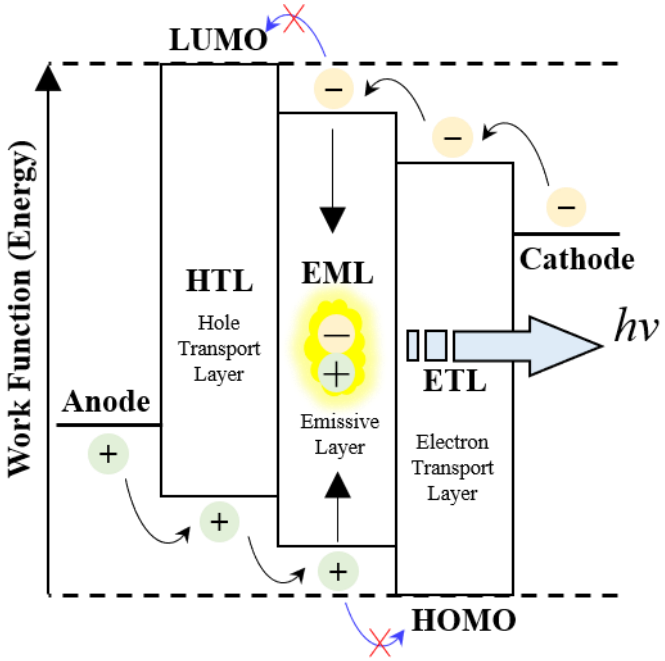

Figure 1.1. The basic electroluminescence (EL) device architecture.

The luminous mechanism of LED is a kind of carrier injection type. Under the applied direct current (DC) voltage, electrons are injected from the cathode into the lowest unoccupied molecular orbital (LUMO) of ETL; holes are injected from the anode into the highest occupied molecular orbital (HOMO) of the HTL. The work function difference caused by the external electric field results in the electrons and holes migrating in the EML. Finally, the electrons and holes recombine and generate excitons (excited state) in the EML **(Figure 1.2)**.

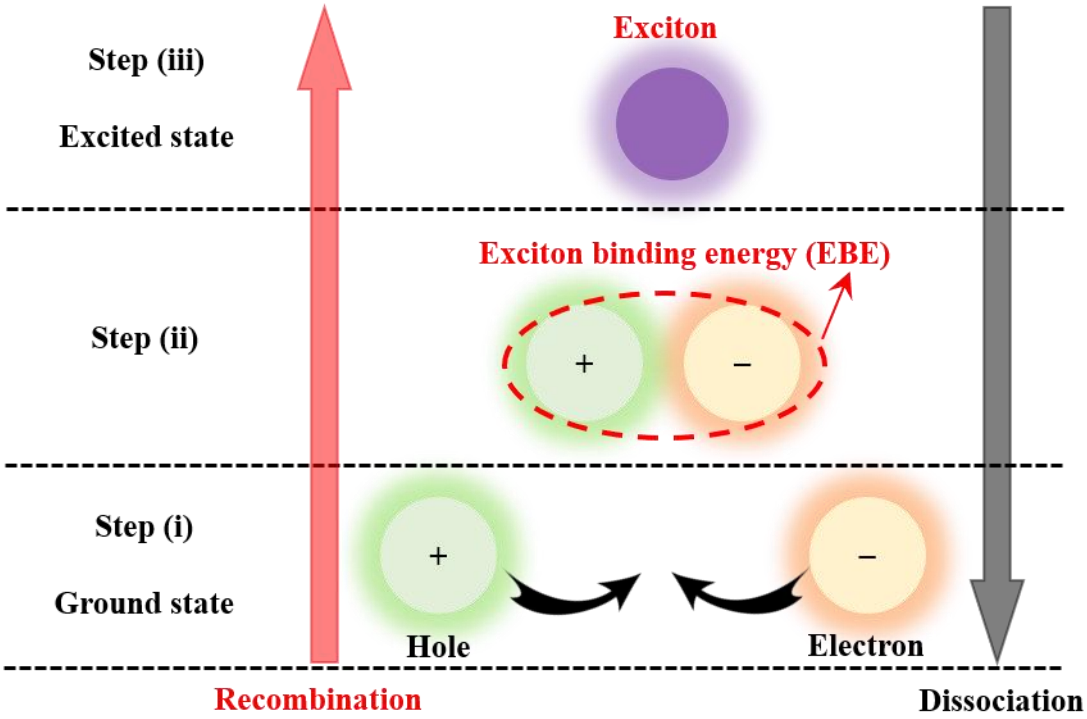

Figure 1.2. Origin of charge transfer exciton recombination in light-emitting diode (LED).

An exciton is a bound state of an electron and a hole that are attracted to each other by the electrostatic Coulomb force. The excited state is any quantum state that has higher energy than the ground state in quantum mechanics. The electrons will quickly relax back to the ground state and release energy without stable energy input to maintain the higher energy level; thus, the excited state is unstable. Typically, the release of energy from the excited state to the ground state can be taken from following forms: (i) non-radiative relaxation, which releases energy through non-luminous ways such as molecular vibrations and thermal effects, (ii) radiative relaxation, which energy will be released in the form of photons. There are two common ways that light can be emitted by photons. The general way, the light emitted is determined by spin configuration of excimer, which is a short-lived dimeric, formed by two fluorophore atoms or molecules. If the excimer electron spin configuration is a singlet state (S1 → S0 + *hv*), it is

called fluorescence; another is phosphorescence, where the light emits when the excimer electron spin configuration is a triplet state **(Figure 1.3)**.

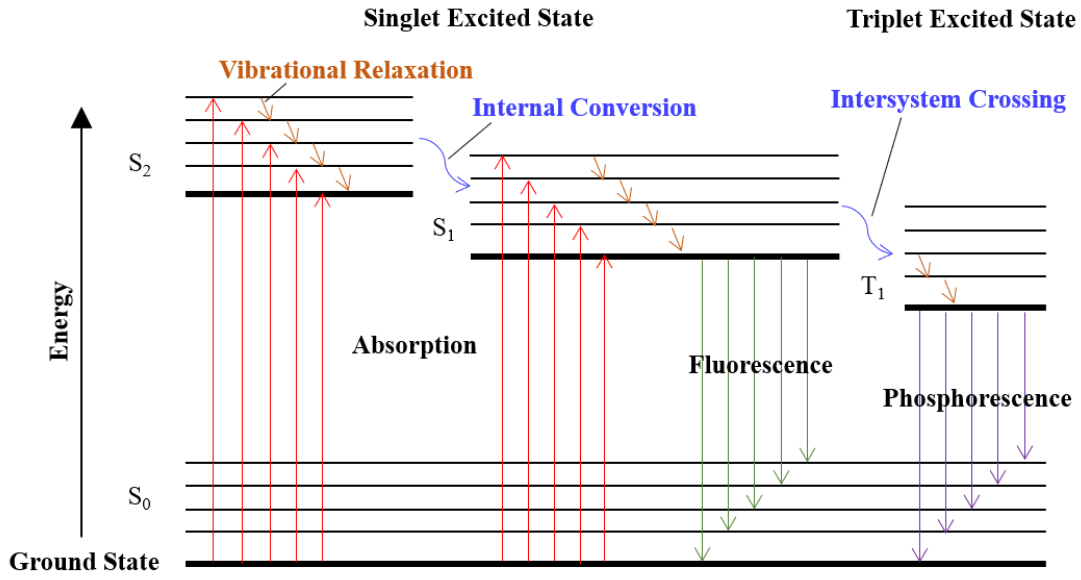

Figure 1.3. Jablonski diagram to illustrate the electronic state of a molecule and the transitions.

In the ideal state, the cathode and anode have a good injection, and the carrier mobility of electrons and holes in the EML is equivalent. Here, an EL device with a high external quantum efficiency (EQE) can be achieved. However, in reality, there are few electron and hole carriers with similar mobility. When the recombination area of the electron and hole is close to the electrode, it will be quenched by the metal surface and reduce the EQE. To achieve highly efficient LEDs, most researchers are focused on adjusting the work function from the device's architectures, aiming at balancing the electron and the hole. Methods to balance electron and hole transport include surface modification to enhance the mobility of charge,[1-3] introducing an electron-blocking layer (EBL) to prevent reverse electron transport,[4,5] modification of the injection contacts to suppress leakage currents,[6] and utilizing more robust HTL to increase the

hole mobility.[7] Because the electron injection rate can be greatly slowed down by adding a high physical barrier from the blocking material; thus introducing an EBL between EML and ETL becomes the most promising way to improve the balance of charge transport **(Figure 1.4)**. For example, Li *et al*. have reported a soluble *tert*-butyldimethylsilyl chloride-modified poly(*p*-phenylene benzobisoxazole) (TBS-PBO) as an EBL for simultaneous good charge transport balance while keeping a high current density in quantum dot light-emitting diode (QLED) system. The results indicate that the versatile TBS-PBO blocks excess electron injection into the EML, thus leading to better charge carrier transfer balance.[8] Another example, Meng *et al*. have developed an all-solution-processing method to introduce the EBL in polymer light-emitting diode (PLED) system. By adding an EBL to balance the electron and hole currents of LED, the efficiency is improved to nearly the theoretical limit.[9]

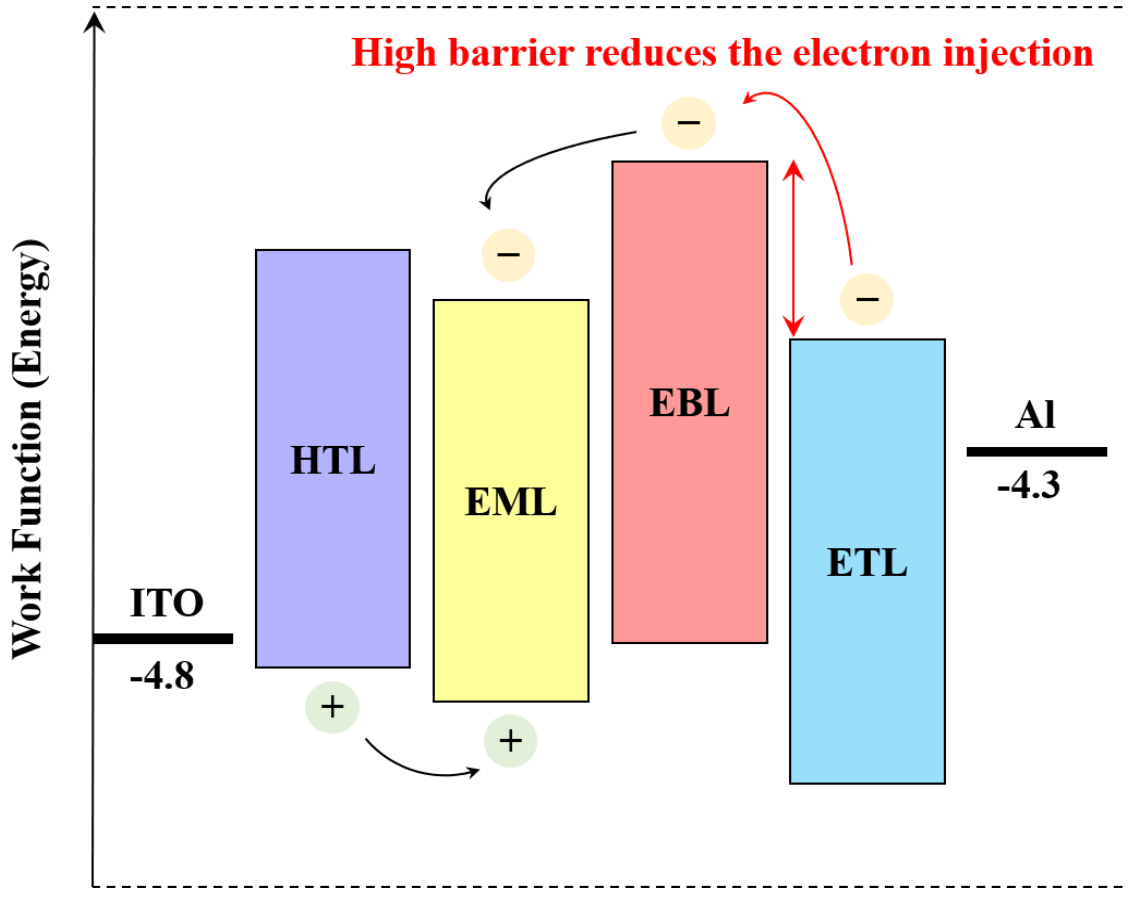

Figure 1.4. Schematic of the energy levels with an electron blocking layer (EBL).

On the other hand, driving current of the LED is mainly determined by two factors. The first is how much space charge inside can be injected into the organic material;[10,11] the second is the injection limited current.[12-14] The solution of the former is to reduce the thickness of the organic film (<1000Å), the latter must choose an electrode with appropriate work function, and cooperate with the contact surface of the organic material to reduce the energy barrier.[15,16] Thus, usually, the anode uses ITO, while the cathode uses low work function metals. For example, Forrest and Burrows *et al*. have proved the current is controlled by trap-limited transport of electrons injected into EML by the dependence of the current-voltage characteristics and luminescence efficiency on layer thickness and HTL composition.[17] Friend and Cacialli *et al*. have merged ultrathin (<100 Å) charge-injection interfacial layers in PLEDs. The results show these interlayers can better control hole injection and electron leakage at the contact between the ITO and the EML.[6] These devices exhibit nearly balanced injection and highlight the importance of adhesion between the polymer films. From the above, it is known that the main factors affecting the characteristics of PLED are the balance of charges in organic materials.

1.2.2 Evolution of polymer light-emitting diode (PLED)

The research on PLED started serval decades ago when the research group of Cambridge University in the United Kingdom (UK) emerged, but the results have not attracted public attention because the used materials are not conjugated polymer. In 1990, Cambridge University, by J. H. Burroughes *et al*.[18] have exploited conjugated polymer materials, which made poly(phenylene vinylenes) (PPV) into a single-layer PLED by using spin-coating. The device architecture is ITO/PPV/Al single-layer device, and the EQE can reach 0.05%. Because of its simple manufacturing process, it has attracted the attention of academic and industrial

circles. In 1992, the research group with Cambridge professor added a polymer layer of 2-(4-biphenylyl)-5-(4-*tert*-butylphenyl)-1,3,4-oxadiazole (butyl-PBD) dispersed in poly(methy1 methacrylate) (PMMA) as an ETL due to the low efficiency of single-layer ITO/PPV/Ca diodes.[19] The architecture of the component is ITO/PPV/PBD-PMMA/ Ca to increase the conductivity of electrons and limit the holes through the polymer layer. Besides, the holes accumulated in the PPV/PBD-PMMA interface will induce the transfer of electrons, which greatly increases its EQE from 0.05% to 0.80%.[20] In 1995, Heeger *et al*. developed the device architecture for ITO/ polyaniline protonated with camphor sulfonic acid in a low molecular weight polyester resin (PANI-CSA-PES)/poly(2-methoxy-5-(2'-ethyl-hexyloxy)-l,4-phenylene vinylene) (MEH-PPV)/Li:Al (alloy),[21] where the doped polyanilines functioned as a composite electrode to enhance the emission of holes. The initial voltage is only 1.7 V and the brightness exceeds 400 cd m^{-2} at 3V, and EQE is 2.23%. Subsequent researchers have aware of the importance of having a multi-layer, and results show that adding a layer of doped conductive polymer between the ITO and EML will greatly help the stability of the device; for example, Parker *et al*. reported a blue light device with five-layer architectures based on ITO/ poly(*N*-vinyl carbazole) (PVK)/ polyquinoline (PQ)/PBD-PMMA/Ca. Since the electronic energy band of this device is a quantum well structure, carriers are easy to combine in the EML (PQ layer) with low energy gap in the middle and emits light with a high EQE of over 4.00%.[22] Due to the difficult manufacturing process and poor device reproducibility of the multi-layer architecture, there is currently no practical applications. Around 2000, the components of the blend structure have regained attention.[23-27] The blend technology has developed highly efficient color-stable white polymer light-emitting diodes (WPLEDs). The WPLEDs can be prepared by blending emissive materials with different emission colors. For example, Wang *et al*. have successfully developed efficient pure-white-light LED by using single, polyfluorene derivatives with 1,8-naphthalimide (NA). The devices exhibit quite stable color coordinates at

different driving voltages with a high EQE of 1.50%.[28] Peng *et al*. have reported a triplet emitter with sky-blue poly[(9,9-bis(4-(2-ethylhexyloxy) phenyl)fluorene)-*co*-(3,7-dibenziothiene-*S*,*S*-dioxide10)] (PPF-3,7SO10) which dually functions as host material with appropriate blending ratio with two emissive polymers, green-emitting poly[2-(4-(30,70-dimethyloctyloxy)-phenyl)-*p*-phenylenevinylene] (P-PPV) and orange-red emitter poly[2-methoxy-5- (20-ethyl-hexyloxy)-1,4-phenylene vinylene] (MEH–PPV) to fabricate efficient WPLEDs. Optimized devices exhibit not only good color quality but also high efficiency (EQE = 6.90%).[29] Although there are already many kinds of research about changing the component materials or device architectures to improve the EQE and lifetime of LED devices in recent years **(Figure 1.5)**.[28,30-36] Typical device architectures mainly rely on inflexible materials such as metal or ITO electrodes and rigid polymer. Consequently, the development and optimization of electroluminescent materials for flexible LED has been the focus of researchers around the world.

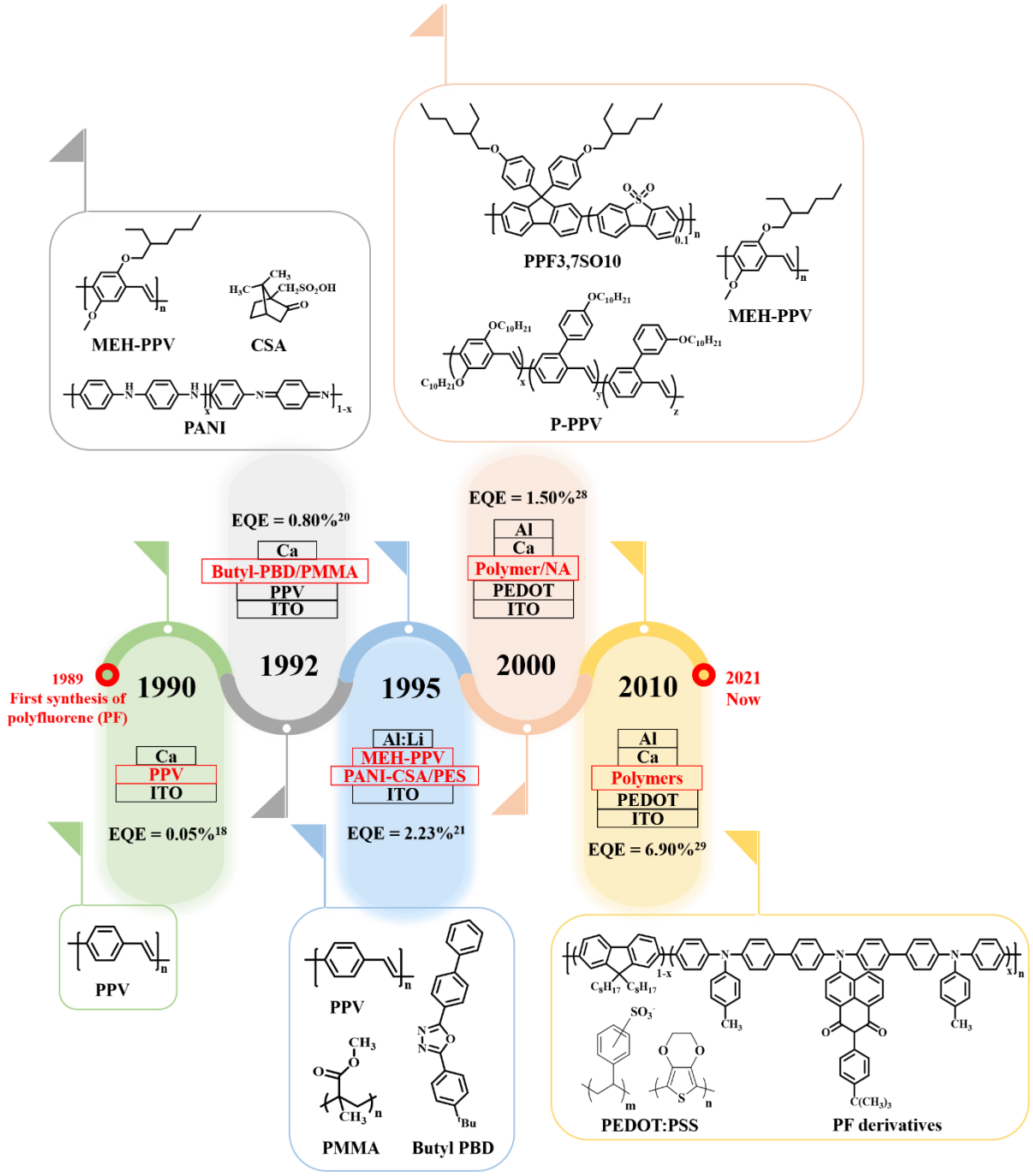

Figure 1.5. Evolution of polymer light-emitting diode (PLED) devices.[3,4,6,14,15]

1.2.3 Current issues of polymer electroluminescent materials

The polymers used in LED devices have many basic requirements.[34,36] Firstly, in terms of operability, a good film formation and injection contact are required to reduce the probability

of leakage current. Secondly, it must have good heat resistance to ensure that the materials will not deteriorate under long-term high temperature operating during the mass production process. Regarding the photoelectric properties, the EML materials must have appropriate ionization energy and electron affinity to reduce the energy barrier of charge transport. The materials are excited with high efficiency of light emission as the device can achieve high performance. It is well-known that photoluminescence quantum yield (PLQY) is a critical index regarding the material's optical performance of LED.[31,37-40] The PLQY of a material is defined as the number of photons emitted as a fraction of the number of photons absorbed. Therefore, the materials with high PLQY imply the potential of being a high efficiency of the device due to the effective recombination between an electrode and a hole.

In the past years, wearable and flexible electronics have been predicted as an alternative technology for the realization of the next generation of electronic applications.[41-44] To apply in flexible electronics, many researchers have been studying the use of flexible substrates (*i.e.* poly(dimethylsiloxane) with silver nanowires (PDMS@AgNWs), polyurethane with silver nanowires (PU@AgNWs), and poly(ethylene terephthalate) coating indium tin oxide (PET@ITO)) to replace rigid metal and ITO substrates.[45-52] Considering the flexible electrode demand and importance, the author will provide another novel method to prepare high flexible and conductive electrodes in Chapter 2 **b**ased on polyfluorene (PF) homopolymer. However, the fabrication of a stretchable electronic based on these LED architectures still constitutes significant obstacles due to the low electroluminescent performance, the limited stretchability of EML, and complicated processing method. The practical applications in flexible PLED are still rare based on the current technology. To overcome the flexibility and electroluminescent problems, in Chapter 3, the author provides a novel strategy combining PF rod-coil block copolymers (BCPs), and the LED exhibits high flexibility and performance. Unexpectedly, the author found that the rod-coil BCPs possess higher PLQY than homopolymer, which implies

the high potential to apply in LED. It is very challenging to develop highly stretchable and high PLQY materials for PLED. To fully utilize the optoelectronic and multifunctionality of organic polymer for wearable applications, the selection of organic materials is essential for developing future high-performance wearable devices. Based on the above-mentioned points, the researchers seek to design a conjugated polymer that possesses high PLQY with good elasticity and mechanical properties.

1.2 Conjugated Polymers on LED

The development of conjugated polymers, also referred to as π-conjugated polymers, has long been established as a new class of materials that can interface electrically active devices with living tissues and organs of the human body.[53-57] Despite the inferior charge carrier mobility and conductivity when compared to inorganic semiconductor and metals, conjugated polymers possess distinct advantages[58-61] such as, (a) low-cost synthesis and process, (b) easy functional versatility through molecular design, (c) lightweight, and (d) simple fabrication of thin film by spin-coating or printing technologies. The integral synthetic process of conjugated polymers is considered more environmentally friendly than the mining process for inorganic semiconductors and metals. Also, conjugated polymer possesses a unique molecular structure, which varies their optical, electrical, and electrochemical properties. Therefore, conjugated polymers have become a focus of interest amongst academic research to carry out a wide variety of novel applications, including skin-mounted sensors, wearable devices, human-machine interfaces, and soft robotics. To achieve these applications, the devices are required to adhere and conform to soft surfaces, while being able to bend, compress, stretch and even self-heal, as like the human skin. One of the main features that make these materials highly suitable for stretchable electronics is the chemically-tunable mechanical properties that allow structural deformation without significantly affecting the electronic function.

In general, conjugated polymers are organic macromolecules that are characterized by a backbone chain of alternative double and single bonds. Radicals, carbenium, or carbanion may be a part of system, which may be cyclic, linear, or mixed, as shown in **Figure 1.6**. A conjugated system has a region of overlapping *p* orbitals and creates a system of delocalized π-electrons in a molecule which lowers the overall energy of the molecule and increases stability. Besides, the π-conjugated backbone facilitates the movement of electrons or holes

when the polymers are reduced or oxidized, resulting in interesting and useful optical and electronic properties.

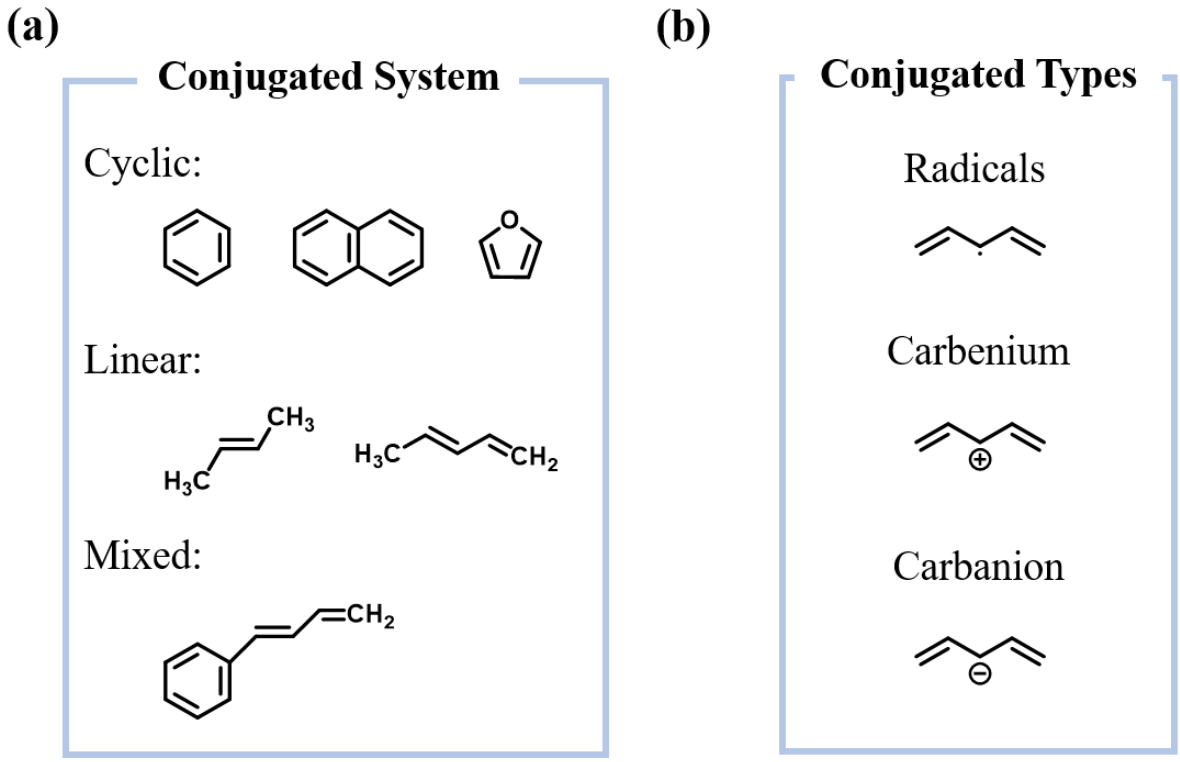

Figure 1.6. Some examples of (a) conjugated systems and (b) conjugated types.

Conjugated polymers for LED has attracted much attention from scientific and technological viewpoints since the first discovery in 1989.[62] The performance and stability of PLED device is highly dependent upon their efficient photoluminescence (PL), charge transport, and good solubility in common organic solvents. The suitable selection of active materials is therefore critical to enhancing these crucial capacities. Several conjugated polymers, such as derivatives of PPVs, polythiophenes (PTs), and PFs have received the most attention in the field of the PLED.[63-68] **Figure 1.7** shows the molecular structure of three

conjugated polymers. In particular, PFs are an excellent candidate for PLED because they show strong blue light-emitting with a high PLQY,[69-71] so that they can be applied as an emissive layer in PLEDs and as host materials for internal color conversion techniques.

Various PF copolymers have been synthesized with emission colors covering the entire visible spectrum[72-74] and the liquid crystalline nature[75-77] of the PFs allow for specific orientations and thereby enable the realization of PLEDs generating polarized light emission. Since the first report on the synthesis of soluble poly(9,9-dialkylfluorene) in 1989 by Fukuda *et al.*, PFs and their copolymers have evolved as a major class of emitting materials for PLEDs.[62] In fact, PLEDs fabricated from PF homopolymer exhibit bright blue emission with efficiencies not reached when using other conjugated polymers. A second important property of PF is their thermotropic liquid crystallinity as first reported by Grell *et al*. in 1997.[78] These researchers have demonstrated that thin layers of well-aligned PFs can be prepared on rubbed polyimide. Thus, the potential of PF as emitting materials in blue PLEDs and the fully conjugated PF polymer backbone open strategies to construct ultrathin layers with highly anisotropic optical, electrooptical and electric properties.[76,79-82]

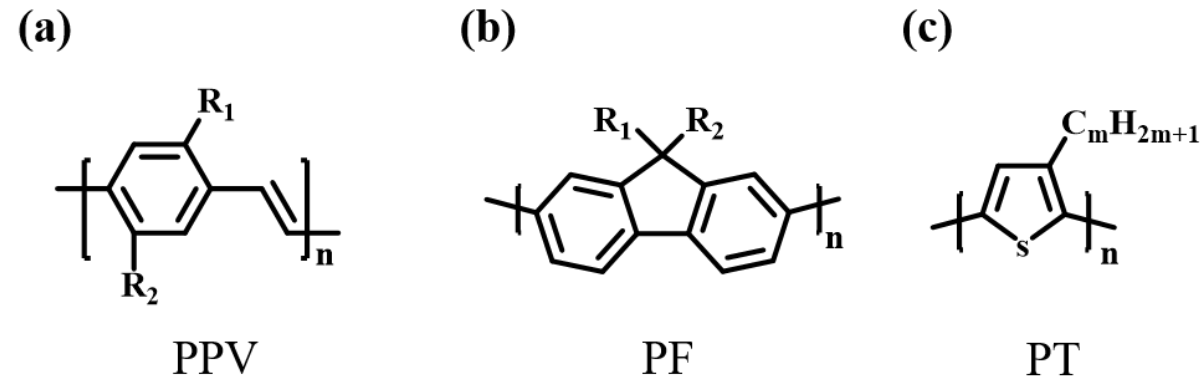

Figure 1.7. General structures of (a) poly(phenylene-vinylene) (PPV), (b) polyfluorene (PF), and (c) polythiophene (PT) used for light-emitting diode (LED).

1.3 Polyfluorene-Based (PF-based) Conjugated Block Copolymers (BCPs)

PF-based conjugated polymers have been the subject of extensive studies due to their unusual morphologies and photophysical behavior in both solution and solid state. Among the complex architectures of PF-based conjugated polymers **(Figure 1.8)**, block copolymers (BCPs) have generated significant interest in the scientific community in recent years not only from their potential technological advantages but also from their ability to naturally self-assemble into periodic ordered nanostructures, which could lead to improved performance of PLED.[83-91] BCPs are macromolecules obtained from two or more blocks of different segments that are covalently connected. Interactions between the blocks generally render them incompatible and drive a microphase separation process, as microphase separation is prohibited by the presence of the covalent bonds. Hence, polymer chains self-assemble into nanoscopic ordered domains with morphology that depends on the ratio of each block lengths (or volume fraction between blocks), strength of interaction, and number of blocks. Precise synthesis provides possibilities to design BCP macromolecules with specific length scales and geometries. Such macromolecular systems can self-assemble hierarchically on multiple length-scales ranging from nanometers to macroscopic sizes leading to a vast variety of nanostructures that can target, in addition to fundamental studies, and applications.

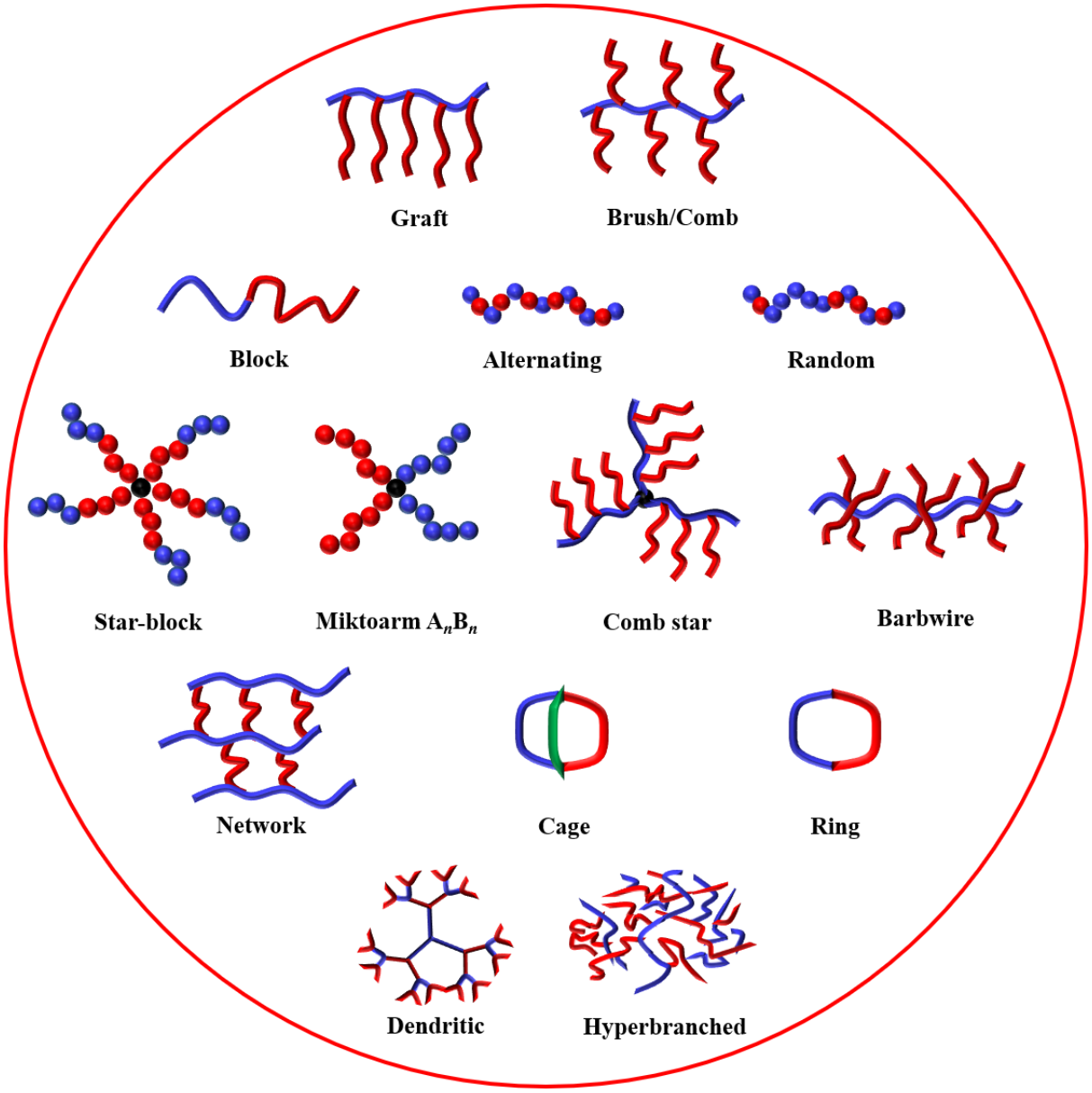

Figure 1.8. Examples of various complex architectures that can be achieved by utilizing PF conjugated polymers.

For electroactive polymers on LEDs, the two major options available to PF-based conjugated BCP engineers in this field are (i) rod-rod BCPs,[86,88,92-102] which have high charge-carrier mobility in both blocks, but lack conformational flexibility **(Figure 1.9)** or (ii) rod-coil BCPs,[91,103-118] conductive block are placed in the backbone along with the coil segment to

enhance overall flexibility **(Figure 1.10)**. Many reports have been published by using rod-rod BCPs. For example, Scherf *et al*. have reported the synthesis of a novel class of rod-rod BCPs with rather different electronic properties and revealed spontaneous formation of meso- and nanostructures.[119-122] However, all conjugated rod-rod BCPs have reported that it again limits their potential applications in aqueous or biomimetic environment due to all hydrophobic blocks. Therefore, Scherf *et al*. further report the first amphiphilic, all conjugated rod-rod BCPs which are based on PF and polar poly(3-alkylthiophene) (PAT) blocks. They described the formation of supramolecular aggregates in two solvent mixtures (tetrahydrofuran/water and tetrahydrofuran/hexane) driven by the different polarity and solubility properties of the blocks.[123] Hereafter, most researches of PF-based rod-rod BCPs mainly focused on the medium used in the self-assembly process to control supramolecular nanostructures with their applications in stiff devices. Despite rapid advances that have been witnessed in conjugated rod-rod BCPs in the past decade, there are still some limitations for practical applications. One vital property of the wearable device is flexibility, which is deficient in the rod-rod conjugated BCPs. It is very important to endow the devices with flexibility and optoelectronic functionalities for any wearable optoelectronic applications. As such, a combination of complementary properties from both rod and coil can be envisioned. Also, most organic electronics rely on the thin film architecture of rod-coil conjugated BCPs. PF-based rod-coil conjugated BCPs containing coil blocks are reported to have enhanced PF crystallinity,[106,124] structural ordering,[104,106,108] and flexibility.[103,104,106] The control over domain size of nanostructures to achieve effective recombination between the electron and hole is known to optimize device performance levels.[125,126] Satoh and Chen *et al*. designed and synthesized rod-coil BCPs consisting of electron-donating poly[2,7-(9,9-dihexylfluorene)] (PFN) rods and electron-withdrawing poly(pendent isoindigo) (Piso) coils through a click reaction.[127] The surface structures and polymer properties were ably tuned by controlling the PF/Piso coil-to-

rod ratio. The stable resistance switching behavior for memory device applications were achieved through thermal annealing process due to forming self-assembled fibrillar nanostructures as well as effective charge transport channels in the polymer thin films. The results indicate that stable digital information storage electronics could be achieved and charge storage volatility was easily manipulated by tuning the PF/Piso ratio.[127] Afterward, rod-coil BCPs start to be utilized in wearable devices because flexibility and nanostructures could be easily manipulated by tuning rod/coil ratio. In 2018, Satoh and Chen *et al*. reported new conjugated rod-coil BCPs consisting of PFN rods and poly(*n*-butyl acrylate) (PBA) coils for stretchable light-emitting device applications.[106] The annealed PFN-*b*-PBA thin film surprisingly exhibited pure blue emission with high photoluminescence quantum yield (PLQY) of over 22.5% under 100% strain, validating the excellent stretchability and promising stability. Besides, the as-cast PFN-*b*-PBA thin films exhibited higher PLQY than their respective homopolymers.[106] Recently, Chiu *et al*. utilized block copolymer with rod poly(9,9-di-*n*-octyl-2,7-fluorene) (PFO) and coil poly(isoprene) (PI) as a model compounds for elastic luminescent.[104] Not only intense mechanical stress but also their stretching associated with high stable luminescence were demonstrated due to the molecular-level rigid island structure of self-assembly nanostructured of PFO domains bridged by PI blocks. Finally, the PFO-*b*-PI copolymer could form an excellent elastic luminescent with stable mechanical performance of the bulk film at 300% strain over 100 cycles, and its thin-film state had a stable PLQY of 19.6% after 1000 cycles of strain = 150%, which is only 7% lower compared to the neat film. Interestingly, their results also showed that the rod-coil BCP's thin film state had higher PLQY than their respective conjugated homopolymer.[104,106] As mentioned earlier, higher PLQY is known to optimize device performance due to the effective recombination between the electron and hole. Therefore, rod-coil BCPs are likely significant advantages to using as light-emitting materials for wearable devices.

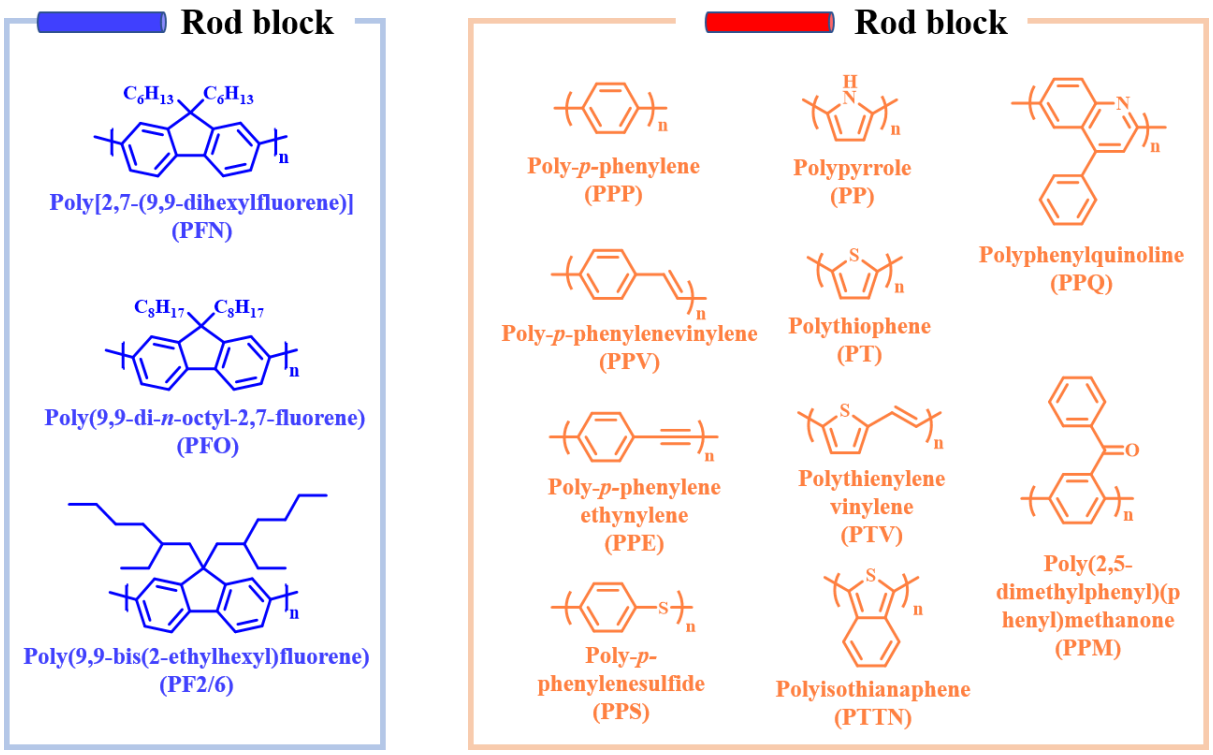

Figure 1.9. The General from the polymer structures of PF-based conjugated rod-rod block copolymers (BCPs).

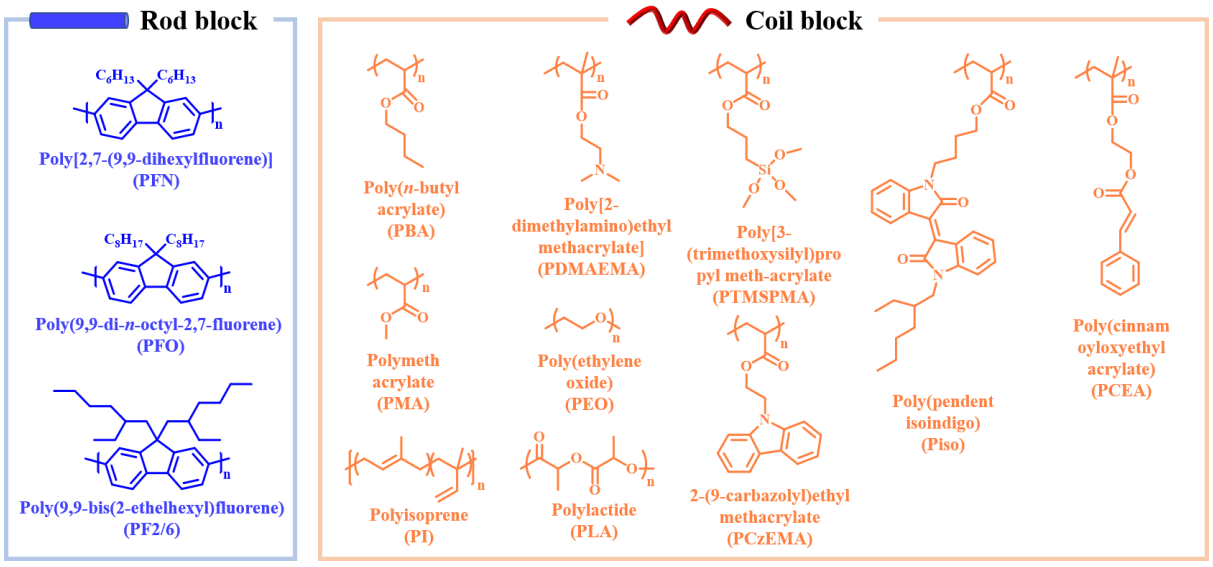

Figure 1.10. The general form on the polymer structures of PF-based conjugated rod-coil block copolymers (BCPs).

1.4 Synthesis of PF-Based Conjugated BCPs

The synthesis of PF-based conjugated rod-coil BCPs generally requires the combination of two different polymerization methods. A two-stage approach is commonly used to synthesize such BCPs. The first stage involves the synthesis of soluble conjugated block with proper another reaction, such as living polymerization. The critical issue for such synthesis is the preparation of soluble conjugated rods with desired chain-end functionality for a stepwise synthesis. Typically, the synthetic way of conjugated rod-coil BCPs can be classified into mainly two categories: (i) polymerization using macroinitiator (the macroinitiator methods) and (ii) condensation of two performed rod and coil blocks (the coupling methods). Typically, PF block has been widely prepared by conventional coupling reactions via Suzuki-Miyaura or Yamamoto coupling polymerization, as summarized in **Scheme 1.1**. For the macroinitiator method, the end-capping procedures of conjugated polymers have been applied for controlling the molecular weight as well as modifying the reactive functionality at the chain end. Then the end-functionalized conjugated block could be used as a macroinitiator in further polymerization to generate coil blocks, like hydroxyl chain end for ring-opening polymerization (ROP), or bromide/chloride chain end for atom transfer radical polymerization (ATRP). On the other hand, the end-functionalized coil blocks are also employed to generate rod blocks by the macroinitiator methods. For the second method, rod and coil blocks with specific functional end groups are prepared individually first and then coupled together by further coupling.

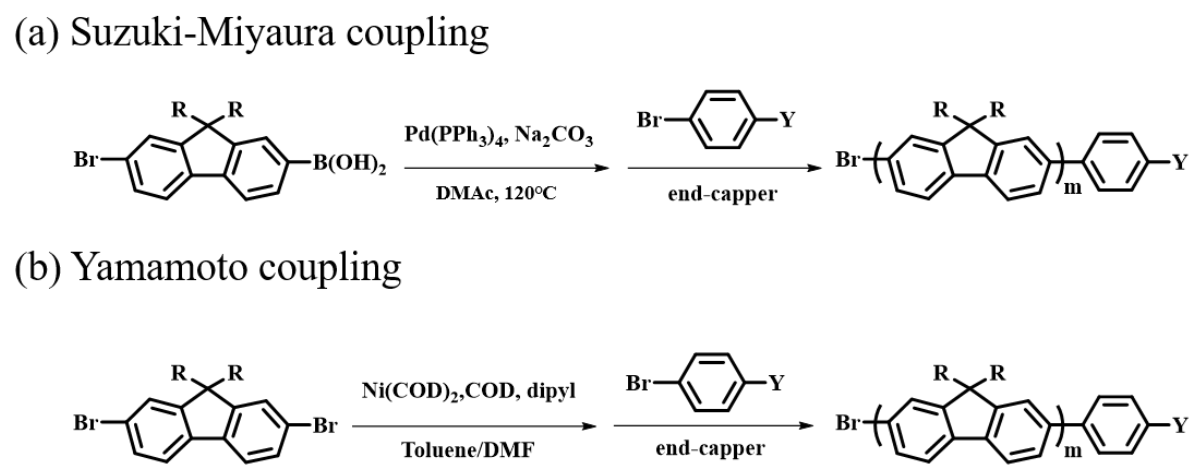

Scheme 1.1. Synthetic approaches of PF homopolymers with the end-cappers following by (a) Suzuki-Miyaura coupling and (b) Yamamoto coupling polymerization.

1.4.1 The macroinitiator method

The ATRP method has been widely employed to prepare rod-coil BCPs through the macroinitiator method due to simple, conventional, and useful for a wide selection of monomers with tolerant reaction conditions. The ATRP method can generate the versatile coil segments from the bromide/chloride chain end, which is from the conjugated block macroinitiator. **Scheme 1.2a** shows the synthesis of rod-coil BCPs by ATRP method through the macroinitiator method, including poly[2,7-(9,9-dihexylfluorene)]-*block*-poly(*tert*-butyl acrylate) (PFN-*b*-P*t*BA),[116] PFN-*b*-poly(methyl methacrylate) (PFN-*b*-PMMA),[114] PFN-*b*-poly(2-(dimethylamino)ethyl methacrylate) (PFN-*b*-PDMAEMA),[128] and PFN-*b*-poly[3-(trimethoxysilyl)propyl methacrylate] (PFN-*b*-PTMSPMA).[129] In addition, a bromo-functionalized terfluorene has also been used as an ATRP macroinitiator to prepare rod-coil BCPs.[118,130-132]

Recently ROP method has been commonly used to prepare rod-coil BCPs from hydroxyl chain-end PF macroinitiator, as shown in **Scheme 1.2b**. For example, Müllen *et al*. have

presented the synthesis of poly(9,9-di-*n*-octyl-2,7-fluorene)-*block*-poly(ethylene oxide) (PFO-*b*-PEO) by perfect mono-end-functionalization, which enabled us to synthesize various kinds of rod-coil BCPs through the macroinitiator method.[133] Satoh *et al*. have reported the rod-coil copolymers consisting of PFN and polylactide (PLA) via ROP from a PFN macroinitiator.[108] Such BCPs exhibited various morphologies of spheres,[89,134] hexagonal closed packed cylinders,[108,134] lamellae,[89,126] and nanofibers[104,106] by varying the rod/coil ratio.

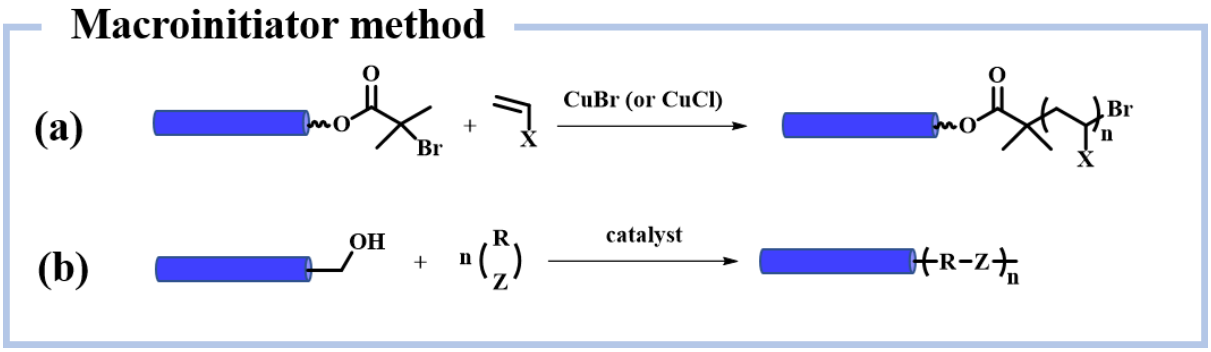

Scheme 1.2. Synthesis of PF-based rod-coil block copolymers through the macroinitiator method: (a) atom transfer radical polymerization (ATRP), and (b) ring-opening polymerization (ROP).

1.4.2 The coupling method

For the coupling method, rod and coil blocks are synthesized individually and then the two blocks having specific functional end groups are coupled together by further cross coupling reactions (**Scheme 1.3**). Satoh *et al*. have been separately synthesized alkylene-terminated rod PF block and azido-terminated coil block, and then two functionalized polymers are undergoing click reaction to obtain copolymers. **Scheme 1.3a** shows the synthesis of rod-coil BCPs by the click reaction through the coupling method, including PFN-*b*-Piso,[127] PFN-*b*-PLA,[108] and PFN-*b*-PBA.[103,106] Another successful way is presented by Leclere and his

coworkers, in which they successfully link copolymers (PFO-*b*-PEO) through an ester linkage between a carboxyl group of the PFO rod end and a hydroxyl group of the PEO coil end (**Scheme 1.3b**).[133]

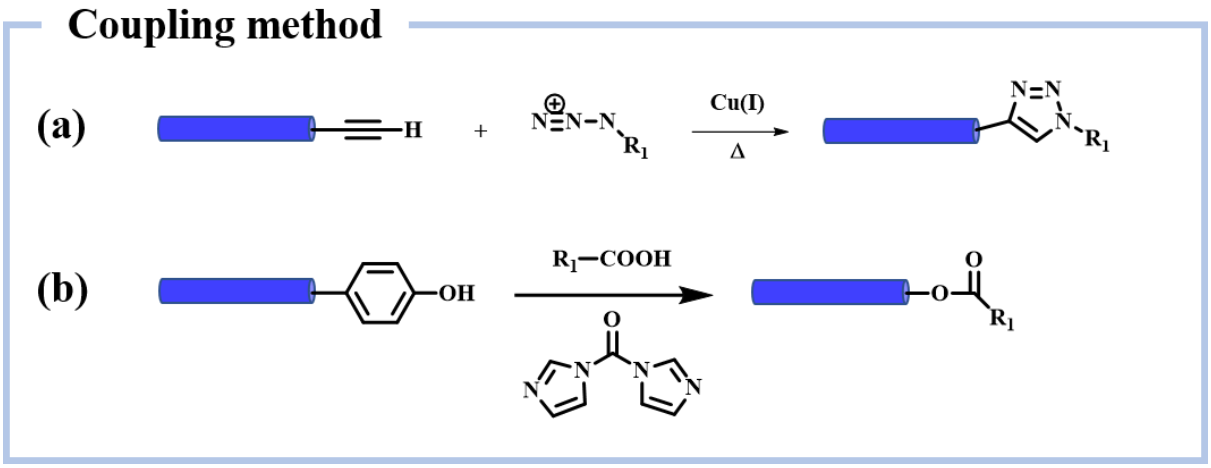

Scheme 1.3. Synthesis of PF-based rod-coil block copolymers through the coupling method: (a) click chemistry and (b) esterification between the carboxyl and hydroxyl end groups.

1.4.3 The LED applications of PF-based conjugated BCPs

Owing to the progress of synthetic approaches based on the macroinitiator and coupling methods, the conjugated rod-coil BCPs have been recognized as a class novel material in optoelectronic devices. Many studies have utilized those methods to demonstrate successful LED applications of rod-coil BCPs. Various rod-coil BCPs, with one conjugated block that derived from PF, have been reported. Such BCPs self-assemble into a variety of ordered structures (spherical, lamellae, cylinder, and bicontinuous, *etc*.) and possess interesting optoelectronic properties that could be used in PLED fabrication. Early examples, Wei Huang *et al*. have reported a novel well-defined PF-based rod-coil BCPs, poly(2-(9-carbazolyl)ethyl methacrylate)-*b*-poly(2,7-dihexylfluorene)-*b*-poly(2-(9-carbazolyl)ethyl methacrylate) (PCzEMA-*b*-PFN-*b*-PCzEMA), which synthesized through the macroinitiator method. The

series of PFN-*b*-PCzEMA copolymers have been synthesized for LED via combining Yamamoto coupling and ATRP. The results indicated that the presence of the PCzEMA block effectively raises the HOMO level, suggesting better hole injection properties. First implied that rod-coil BCP with optoelectronic functionality is promising candidates for LED applications.[117] Subsequently, Huang *et al*. published the same strategy using the rod- coil BCP for fabricating pixelated displays. The BCP, poly(2-trimethylsilyloxyethylacrylate)-*b*-poly(2,7-dihexylfluorene)-*b*-poly(2-trimethyl silyloxyethyl acrylate) (PCEA-*b*-PFN-*b*-PCEA) is prepared by same synthetic method. The results indicate that the coil block may induce longer lifetimes and stability in PLED fabrication due to the better stability under thermal stress and ultraviolet-visible (UV-visible) irradiation.[135] Recently, Chiu *et al*. have fabricated an intrinsically stretchable LED by using rod-coil poly[2,7-(9,9-dioctylfluorene)]-*block*-poly(isoprene) (PFO-*b*-PI). The PFO-*b*-PI block copolymer with various PFO/PI ratios is synthesized through macromolecular chain transfer agent (PFO-CTA) through the reversible addition-fragmentation chain transfer (RAFT) technique, which revealed a new synthetic procedure for PF-based polymers and exhibited excellent exceptional stretchability and high stability of LEDs.[136] Above reports demonstrate that such a rod-coil BCPs exhibited high flexibility when incorporated in PLEDs, leading to high stability as well. Combining the optoelectronic functionality of rod-coil BCPs with control overall morphology on block ratio (rod/coil) relevant to charge mobility, radiative recombination, and PLQY leads to idealized active layers with potentially improved device performance. This is still a nascent area of research, and coming years are sure to unfold additional unforeseen insights and applications for this exciting intersection of materials technology.

1.5 Objective and Outline of the Dissertation

Currently, stretchable electronics have been received extensive attention as an alternative technology for the realization of the next generation to replace the conventional stiff devices. Stretchable displays and solid-state lighting systems would enable expandable and foldable screens for smartphones,[137,138] collapsible or rollable lamps,[139] biocompatible fluorescence sources in vivo or epidermal medical devices,[140] and wearable electronic clothes[141,142] due to combining elastic interconnects with discrete rigid LED. To realize the stretchable and wearable LED, a high conductive and flexible electrode is indispensable element. The flexible electrodes must be highly flexible to survive the mechanical deformation of the malleable host materials.

It is critical to study the use of flexible substrates to replace the rigid ITO or metal electrodes, as described in **Section 1.1.3**. As mentioned above, the organic conjugated polymer in LED has attracted much attention to replacing the conventional inorganic or metal due to distinct advantages **(Section 1.2)**. In Chapter 2, the author is providing a novel method to prepare highly flexible and conductive electrodes based on copper/silver (Cu/Ag) metal and PFO homopolymer. However, there still exist some limitations in the development of a fully flexible electronic. Even using a highly flexible and conductive electrodes, the low luminance and rigid PFO as an EML showed unfavorable to be utilized for flexible LED. Therefore, research finding the emissive material with high PLQY and flexibility is lacking in the current scientific area. The rod-coil BCPs, combining with rigid conjugated block as a rod and soft block as a coil, are the most reasonable and widely accepted materials to achieve highly flexible wearable devices because of their feature nanostructures and tunable electronic properties by varying rod/coil ratio, as described in **Section 1.3**. As a consequence of this, over the last decade, the significant knowledge about organic conjugated polymer and the advanced synthesis, represented by the macroinitiator and coupling methods, have been remarkably built-up

(Section 1.4). However, the practical applications are rarely realized due to several unmet requirements. For example, in general, the insulating property of coil blocks considerably dampens the interchain charge transport properties, which is unfavorable for achieving efficient electroluminescent devices. Therefore, a tradeoff exists in the molecular design of conjugated BCPs and it is of urgent need to solve this tradeoff to develop stretchable electronics. To address this point, the author demonstrates a facile strategy based on PF-based rod-coil BCPs to enhance high performance and flexibility LED in Chapter 3. As another interesting discovery, aforementioned studies have shown that rod-coil BCPs exhibit higher PLQY than their respective homopolymers.[104,106] The PLQY is a vital index about the EQE of LED, and therefore, high PLQY of rod-coil BCPs imply that they are potential candidates for LED applications. However, specific discussions regarding higher PLQY in rod-coil BCP systems has not been reported yet. Thereby, the goal of this dissertation is to establish the facile synthetic method of the PF-based rod-coil BCPs, which could be used for the substantial LED applications due to high PLQY value, and will be discussed in-depth in Chapter 4. Regarding practical applications, the author is focused on the development of wearable devices with highly flexible and stable performance and explained the high PLQY phenomenon in rod-coil BCP systems.

An outline of this dissertation is as follows:

Chapter 2 describes a novel copper/silver (Cu)/Ag core/shell nanofibers (NFs) as a transparent conductive electrode (TCE) with a deep blue PFO as EML for flexible LEDs. Various architectures of Cu/Ag core/shell NFs, *i.e.*, random, aligned, and crossed types, are fabricated by using the Ag electroless plating process to coat onto the electrospun Cu-NFs. The results indicate that the Ag protective layer enhanced the stability of the fibers oxidation and improved its conductivity. The author provides a novel method that a critical advantage for Cu/Ag-NFs to replace rigid ITO in the industry and commercial uses owing to the extraordinary performance and the cost-effectiveness of electrospun Cu/Ag-NFs as TCE. The Cu/Ag-NF electrodes exhibit not only high transparency but also stretchability. Moreover, the novel Cu/Ag-NF electrodes could easily be transferred to any other substrate for versatile shape and a flexible PLED with blue emitter PFO can be produced **(Figure 1.11)**.

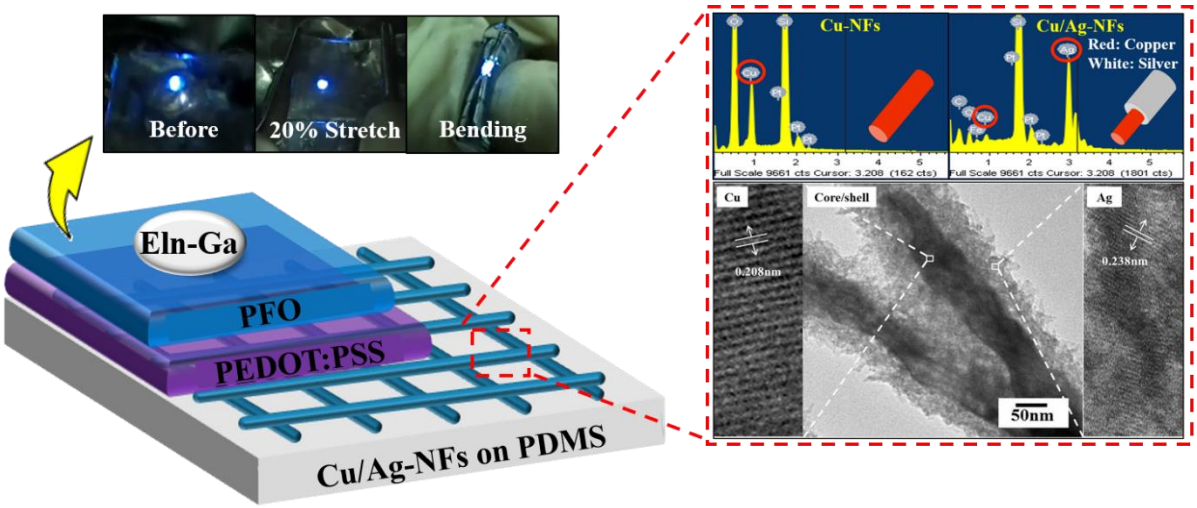

Figure 1.11. The application of Cu/Ag core/shell NF electrodes in semitransparent and flexible light-emitting diode (LED) with blue emitter poly(9,9-di-*n*-octyl-2,7-fluorene) (PFO).

Chapter 3 describes the comprehensive examination of a series PF-based rod-coil BCPs of poly[2,7-(9,9-dihexylfluorene)] (PFN) and poly(*n*-butyl acrylate) (PBA) via the click reaction. The author demonstrates a novel strategy for preparing NF films of light down-converter LEDs by combining rod-coil BCPs with perovskite quantum dots (QDs) through a simple electrospinning method. The results show that polymer deformability can be promoted by incorporating a coil block (PBA) and controlled by varying the rod/coil (PFN/PBA) ratio, and the color can be adjusted by controlling the ratio between QD and PFN due to energy transfer from PFN block (donor) to perovskite QD (acceptor) **(Figure 1.12)**. Furthermore, high luminance white-light-emitter can be achieved by only a single layer without traditional multilayers. The above-established blending approach reveals the potential of using PF-based rod-coil BCP to fabricate high luminance and color-tunable light down-converter LEDs.

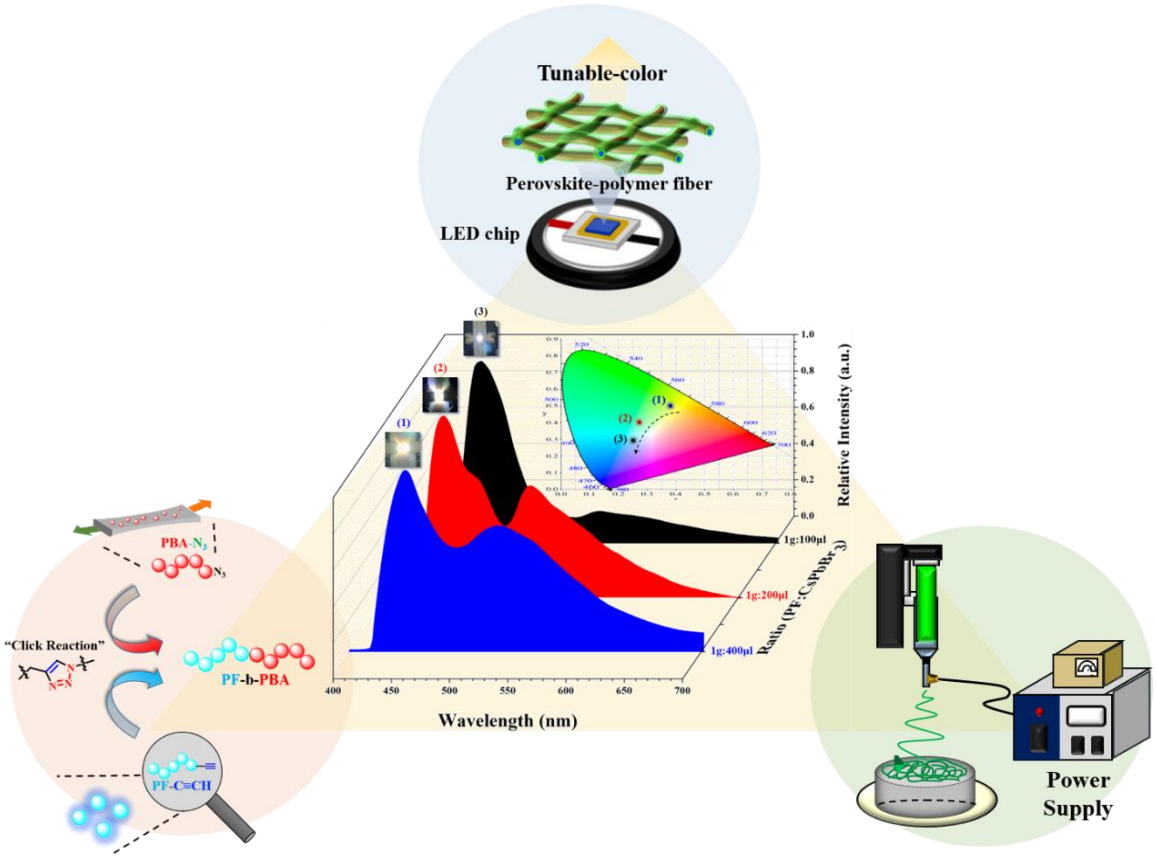

Figure 1.12. Schematic representation of using PF-based rod-coil block copolymers (BCPs) to fabricate color-tunable light down-converter light-emitting diodes (LEDs).

Chapter 4 describes a smart one-pot synthetic approach for preparing PF-based BCPs that involves simple purification for fabricating touch-responsive LED devices **(Figure 1.13)**. A series of PF-based BCPs are synthesized by using Suzuki–Miyaura catalyst transfer polymerization (SCTP) and ROP. Moreover, the author successfully explains the phenomenon that rod-coil BCPs possess high PLQY by a model material of poly(9,9-di-*n*-hexyl-2,7-fluorene)-*block*-poly(*δ*-decanolactone) (PFN-*b*-PDL). The PFN-*b*-PDL BCP system specifically exhibits high EQE higher than PF homopolymer. Furthermore, the BCPs device exhibits higher carrier recombination efficiency, flex-stretch stability, and mechanical endurance highlighting the brighter potential of rod-coil BCPs for fabricating highly durable wearable stretchable nano and microelectronic devices.

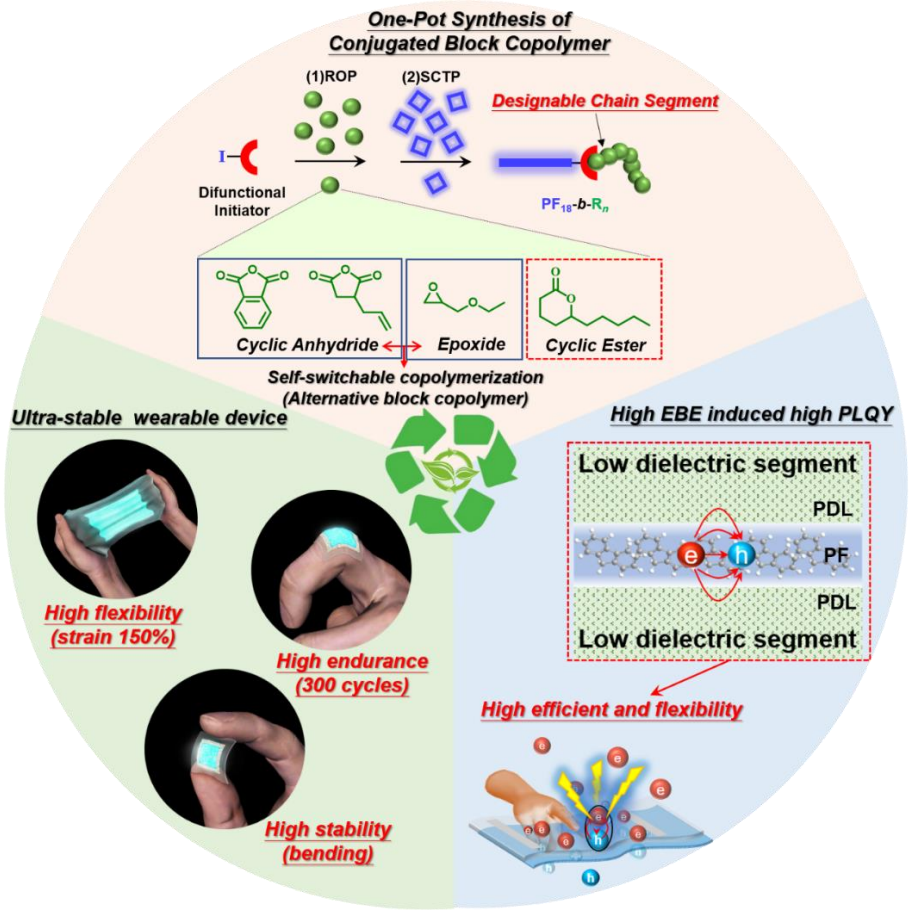

Figure 1.13. Demonstration of smart one-pot procedure for facile preparing fully stretchable touch-responsive light-emitting diode (LED) devices.

The concluding Chapter 5 summarized the novel (one-pot) synthetic methodology of polyfluorene-based conjugated polymers and the facile preparation of wearable and stretchable polyfluorene-LED devices, as the overall conclusions of this dissertation.

1.6 References

1. Sun, Y.; Wang, W.; Zhang, H.; Su, Q.; Wei, J.; Liu, P.; Chen, S.; Zhang, S., High-performance quantum dot light-emitting diodes based on Al-doped ZnO nanoparticles electron transport layer. ACS Appl. Mater. Interfaces 2018, 10 (22), 18902-18909.

2. Kim, J.-H.; Han, C.-Y.; Lee, K.-H.; An, K.-S.; Song, W.; Kim, J.; Oh, M. S.; Do, Y. R.; Yang, H., Performance improvement of quantum dot-light-emitting diodes enabled by an alloyed ZnMgO nanoparticle electron transport layer. Chem. Mater. 2015, 27 (1), 197-204.

3. Liang, X.; Ren, Y.; Bai, S.; Zhang, N.; Dai, X.; Wang, X.; He, H.; Jin, C.; Ye, Z.; Chen, Q., Colloidal indium-doped zinc oxide nanocrystals with tunable work function: rational synthesis and optoelectronic applications. Chem. Mater. 2014, 26 (17), 5169-5178.

4. Peng, H.; Wang, W.; Chen, S., Efficient quantum-dot light-emitting diodes with 4, 4, 4-tris (N-carbazolyl)-triphenylamine (TcTa) electron-blocking layer. IEEE Electron Device Lett. 2015, 36 (4), 369-371.

5. Sun, Q.; Subramanyam, G.; Dai, L.; Check, M.; Campbell, A.; Naik, R.; Grote, J.; Wang, Y., highly efficient quantum-dot light-emitting diodes with DNA− CTMA as a combined hole-transporting and electron-blocking layer. ACS Nano 2009, 3 (3), 737-743.

6. Ho, P. K.; Kim, J.-S.; Burroughes, J. H.; Becker, H.; Li, S. F.; Brown, T. M.; Cacialli, F.; Friend, R. H., Molecular-scale interface engineering for polymer light-emitting diodes. Nature 2000, 404 (6777), 481-484.

7. Ji, W.; Lv, Y.; Jing, P.; Zhang, H.; Wang, J.; Zhang, H.; Zhao, J., Highly efficient and low turn-on voltage quantum dot light-emitting diodes by using a stepwise hole-transport layer. ACS Appl. Mater. Interfaces 2015, 7 (29), 15955-15960.

8. Jin, X.; Chang, C.; Zhao, W.; Huang, S.; Gu, X.; Zhang, Q.; Li, F.; Zhang, Y.; Li, Q., Balancing the electron and hole transfer for efficient quantum dot light-emitting diodes by employing a versatile organic electron-blocking layer. ACS Appl. Mater. Interfaces 2018, 10 (18), 15803-15811.

9. Tseng, S.-R.; Meng, H.-F.; Yeh, C.-H.; Lai, H.-C.; Horng, S.-F.; Liao, H.-H.; Hsu, C.-S.; Lin, L.-C., High-efficiency blue multilayer polymer light-emitting diode fabricated by a general liquid buffer method. Synth. Met. 2008, 158 (3-4), 130-134.

10. Campbell, I.; Smith, D.; Neef, C.; Ferraris, J., Consistent time-of-flight mobility measurements and polymer light-emitting diode current–voltage characteristics. Appl. Phys. Lett. 1999, 74 (19), 2809-2811.

11. DeMello, J.; Tessler, N.; Graham, S.; Friend, R., Ionic space-charge effects in polymer light-emitting diodes. Phys. Rev. B 1998, 57 (20), 12951.

12. Haque, S. A.; Koops, S.; Tokmoldin, N.; Durrant, J. R.; Huang, J.; Bradley, D. D.; Palomares, E., A Multilayered Polymer Light-Emitting Diode Using a Nanocrystalline Metal-Oxide Film as a Charge-Injection Electrode. Adv. Mater. 2007, 19 (5), 683-687.

13. O'Brien, D.; Giebeler, C.; Fletcher, R.; Cadby, A.; Palilis, L.; Lidzey, D.; Lane, P.; Bradley, D.; Blau, W., Electrophosphoresence from a doped polymer light emitting diode. Synth. Met. 2001, 116 (1-3), 379-383.

14. Carter, S.; Angelopoulos, M.; Karg, S.; Brock, P.; Scott, J., Polymeric anodes for improved polymer light-emitting diode performance. Appl. Phys. Lett. 1997, 70 (16), 2067-2069.

15. Shaheen, S.; Jabbour, G.; Morrell, M.; Kawabe, Y.; Kippelen, B.; Peyghambarian, N.; Nabor, M.-F.; Schlaf, R.; Mash, E. A.; Armstrong, N. R., Bright blue organic light-emitting diode with improved color purity using a LiF/Al cathode. J. Appl. Phys. 1998, 84 (4), 2324-2327.

16. Son, D. I.; Kim, H. H.; Hwang, D. K.; Kwon, S.; Choi, W. K., Inverted CdSe–ZnS quantum dots light-emitting diode using low-work function organic material polyethylenimine ethoxylated. J. Mater. Chem. C 2014, 2 (3), 510-514.

17. Burrows, P.; Forrest, S., Electroluminescence from trap-limited current transport in vacuum deposited organic light emitting devices. Appl. Phys. Lett. 1994, 64 (17), 2285-2287.

18. Burroughes, J. H.; Bradley, D. D.; Brown, A.; Marks, R.; Mackay, K.; Friend, R. H.; Burns, P.; Holmes, A., Light-emitting diodes based on conjugated polymers. Nature 1990, 347 (6293), 539-541.

19. Braun, D.; Heeger, A., Visible light emission from semiconducting polymer diodes. Appl. Phys. Lett. 1991, 59 (7), 878-878.

20. Brown, A.; Bradley, D.; Burroughes, J.; Friend, R.; Greenham, N.; Burn, P.; Holmes, A.; Kraft, A., Poly (p-phenylenevinylene) light-emitting diodes: Enhanced electroluminescent efficiency through charge carrier confinement. Appl. Phys. Lett. 1992, 61 (23), 2793-2795.

21. Yang, Y.; Westerweele, E.; Zhang, C.; Smith, P.; Heeger, A., Enhanced performance of polymer light-emitting diodes using high-surface area polyaniline network electrodes. J. Appl. Phys. 1995, 77 (2), 694-698.

22. Parker, I.; Pei, Q.; Marrocco, M., Efficient blue electroluminescence from a fluorinated polyquinoline. Appl. Phys. Lett. 1994, 65 (10), 1272-1274.

23. Berggren, M.; Inganäs, O.; Gustafsson, G.; Rasmusson, J.; Andersson, M. R.; Hjertberg, T.; Wennerström, O., Light-emitting diodes with variable colours from polymer blends. Nature 1994, 372 (6505), 444-446.

24. Thompson, J.; Blyth, R.; Mazzeo, M.; Anni, M.; Gigli, G.; Cingolani, R., White light emission from blends of blue-emitting organic molecules: A general route to the white organic light-emitting diode? Appl. Phys. Lett. 2001, 79 (5), 560-562.

25. Moons, E., Conjugated polymer blends: linking film morphology to performance of light emitting diodes and photodiodes. J. Phys. Condens. Matter 2002, 14 (47), 12235.

26. Chen, Y.; Chen, J.; Zhao, Y.; Ma, D., High efficiency blue phosphorescent organic light-emitting diode based on blend of hole-and electron-transporting materials as a co-host. Appl. Phys. Lett. 2012, 100 (21), 114.

27. Zhang, L.; Cai, C.; Li, K. F.; Tam, H. L.; Chan, K. L.; Cheah, K. W., Efficient organic light-emitting diode through triplet exciton reharvesting by employing blended electron donor and acceptor as the emissive layer. ACS Appl. Mater. Interfaces 2015, 7 (45), 24983-24986.

28. Tu, G.; Mei, C.; Zhou, Q.; Cheng, Y.; Geng, Y.; Wang, L.; Ma, D.; Jing, X.; Wang, F., Highly Efficient Pure-White-Light-Emitting Diodes from a Single Polymer: Polyfluorene with Naphthalimide Moieties. Adv. Funct. Mater. 2006, 16 (1), 101-106.

29. Zou, J.; Liu, J.; Wu, H.; Yang, W.; Peng, J.; Cao, Y., High-efficiency and good color quality white light-emitting devices based on polymer blend. Org. Electron. 2009, 10 (5), 843-848.

30. Zhang, X.; Zheng, Q.; Tang, Z.; Li, W.; Zhang, Y.; Xu, K.; Xue, X.; Xu, J.; Wang, H.; Wei, B., Tunable hole injection of solution-processed polymeric carbon nitride towards efficient organic light-emitting diode. Appl. Phys. Lett. 2018, 112 (8), 083302.

31. Nimith, K.; Satyanarayan, M.; Umesh, G., Enhancement in fluorescence quantum yield of MEH-PPV: BT blends for polymer light emitting diode applications. Opt. Mater. 2018, 80, 143-148.

32. Zhang, Y.; Lee, J.; Forrest, S. R., Tenfold increase in the lifetime of blue phosphorescent organic light-emitting diodes. Nat. Commun. 2014, 5 (1), 1-7.

33. Li, G.; Fleetham, T.; Li, J., Efficient and stable white organic Light-Emitting diodes employing a single emitter. Adv. Mater. 2014, 26 (18), 2931-2936.

34. Zheng, H.; Zheng, Y.; Liu, N.; Ai, N.; Wang, Q.; Wu, S.; Zhou, J.; Hu, D.; Yu, S.; Han, S., All-solution processed polymer light-emitting diode displays. Nat. Commun. 2013, 4 (1), 1-7.

35. Kamtekar, K. T.; Monkman, A. P.; Bryce, M. R., Recent advances in white organic light-emitting materials and devices (WOLEDs). Adv. Mater. 2010, 22 (5), 572-582.

36. Geffroy, B.; Le Roy, P.; Prat, C., Organic light-emitting diode (OLED) technology: materials, devices and display technologies. Polym. Int. 2006, 55 (6), 572-582.

37. Jakubiak, R.; Rothberg, L.; Wan, W.; Hsieh, B., Reduction of photoluminescence quantum yield by interchain interactions in conjugated polymer films. Synth. Met. 1999, 101 (1-3), 230-233.

38. Van Dijken, A.; Perro, A.; Meulenkamp, E.; Brunner, K., The influence of a PEDOT: PSS layer on the efficiency of a polymer light-emitting diode. Org. Electron. 2003, 4 (2-3), 131-141.

39. Smith, L. H.; Wasey, J. A.; Samuel, I. D.; Barnes, W. L., Light out-coupling efficiencies of organic light-emitting diode structures and the effect of photoluminescence quantum yield. Adv. Funct. Mater. 2005, 15 (11), 1839-1844.

40. do Nascimento Neto, J. A. n.; Valdo, A. K. S. M.; da Silva, C. C.; Guimarães, F. F.; Queiroz Júnior, L. H. K.; Maia, L. J. Q.; de Santana, R. C.; Martins, F. T., A Blue-Light-Emitting Cadmium Coordination Polymer with 75.4% Photoluminescence Quantum Yield. J. Am. Chem. Soc. 2019, 141 (8), 3400-3403.

41. Rogers, J. A.; Someya, T.; Huang, Y., Materials and mechanics for stretchable electronics. Science 2010, 327 (5973), 1603-1607.

42. Kim, D. H.; Lu, N.; Huang, Y.; Rogers, J. A., Materials for stretchable electronics in bioinspired and biointegrated devices. MRS Bull. 2012, 37 (3), 226-235.

43. Fan, J. A.; Yeo, W.-H.; Su, Y.; Hattori, Y.; Lee, W.; Jung, S.-Y.; Zhang, Y.; Liu, Z.; Cheng, H.; Falgout, L., Fractal design concepts for stretchable electronics. Nat. Commun. 2014, 5 (1), 1-8.

44. You, I.; Kong, M.; Jeong, U., Block copolymer elastomers for stretchable electronics. Acc. Chem. Res. 2018, 52 (1), 63-72.

45. Jiang, D.-H.; Liao, Y.-C.; Cho, C.-J.; Veeramuthu, L.; Liang, F.-C.; Wang, T.-C.; Chueh, C.-C.; Satoh, T.; Tung, S.-H.; Kuo, C.-C., Facile Fabrication of Stretchable Touch-Responsive Perovskite Light-Emitting Diodes Using Robust Stretchable Composite Electrodes. ACS Appl. Mater. Interfaces 2020, 12 (12), 14408-14415.

46. Veeramuthu, L.; Chen, B.-Y.; Tsai, C.-Y.; Liang, F.-C.; Venkatesan, M.; Jiang, D.-H.; Chen, C.-W.; Cai, X.; Kuo, C.-C., Novel stretchable thermochromic transparent heaters designed for smart window defroster applications by spray coating silver nanowire. RSC Adv. 2019, 9 (61), 35786-35796.

47. Coskun, S.; Ates, E. S.; Unalan, H. E., Optimization of silver nanowire networks for polymer light emitting diode electrodes. Nanotechnology 2013, 24 (12), 125202.

48. Chen, J.; Liu, C. T., Technology advances in flexible displays and substrates. IEEE Access. 2013, 1, 150-158.

49. Ummartyotin, S.; Juntaro, J.; Sain, M.; Manuspiya, H., Development of transparent bacterial cellulose nanocomposite film as substrate for flexible organic light emitting diode (OLED) display. Ind. Crop. Prod. 2012, 35 (1), 92-97.

50. Yu, Z.; Zhang, Q.; Li, L.; Chen, Q.; Niu, X.; Liu, J.; Pei, Q., Highly flexible silver nanowire electrodes for shape-memory polymer light-emitting diodes. Adv. Mater. 2011, 23 (5), 664-668.

51. Li, L.; Yu, Z.; Hu, W.; Chang, C. h.; Chen, Q.; Pei, Q., Efficient flexible phosphorescent polymer light-emitting diodes based on silver nanowire-polymer composite electrode. Adv. Mater. 2011, 23 (46), 5563-5567.

52. Xie, Z.; Hung, L.-S.; Zhu, F., A flexible top-emitting organic light-emitting diode on steel foil. 2003, 381 (5-6), 691-696.

53. Polikov, V. S.; Tresco, P. A.; Reichert, W. M., Response of brain tissue to chronically implanted neural electrodes. J. Neurosci. Meth. 2005, 148 (1), 1-18.

54. Navarro, X.; Krueger, T. B.; Lago, N.; Micera, S.; Stieglitz, T.; Dario, P., A critical review of interfaces with the peripheral nervous system for the control of neuroprostheses and hybrid bionic systems. J. Peripher. Nerv. Syst. 2005, 10 (3), 229-258.

55. Trohman, R. G.; Kim, M. H.; Pinski, S. L., Cardiac pacing: the state of the art. Lancet 2004, 364 (9446), 1701-1719.

56. Nordhausen, C. T.; Maynard, E. M.; Normann, R. A., Single unit recording capabilities of a 100 microelectrode array. Brain Res. 1996, 726 (1-2), 129-140.

57. Hoogerwerf, A. C.; Wise, K. D., A three-dimensional microelectrode array for chronic neural recording. IEEE Trans. Biomed. Eng. 1994, 41 (12), 1136-1146.

58. Gobalasingham, N. S.; Thompson, B. C., Direct arylation polymerization: A guide to optimal conditions for effective conjugated polymers. Prog. Polym. Sci. 2018, 83, 135-201.

59. Zhu, C.; Liu, L.; Yang, Q.; Lv, F.; Wang, S., Water-soluble conjugated polymers for imaging, diagnosis, and therapy. Chem. Rev. 2012, 112 (8), 4687-4735.

60. Bhattacharyya, D.; Howden, R. M.; Borrelli, D. C.; Gleason, K. K., Vapor phase oxidative synthesis of conjugated polymers and applications. J. Polym. Sci., Part B: Polym. Phys. 2012, 50 (19), 1329-1351.

61. McNeill, C. R.; Greenham, N. C., Conjugated-polymer blends for optoelectronics. Adv. Mater. 2009, 21 (38-39), 3840-3850.

62. Fukuda, M.; Sawada, K.; Yoshino, K., Fusible conducting poly (9-alkylfluorene) and poly (9, 9-dialkylfluorene) and their characteristics. Japn. J. Appl. Phys. 1989, 28 (8A), L1433.

63. Iwasaki, Y.; Osasa, T.; Asahi, M.; Matsumura, M.; Sakaguchi, Y.; Suzuki, T., Fractions of singlet and triplet excitons generated in organic light-emitting devices based on a polyphenylenevinylene derivative. Phys. Rev. B 2006, 74 (19), 195209.

64. Chen, Z.-K.; Lee, N. H. S.; Huang, W.; Xu, Y.-S.; Cao, Y., New phenyl-substituted PPV derivatives for polymer light-emitting diodes− synthesis, characterization and structure− property relationship study. Macromolecules 2003, 36 (4), 1009-1020.

65. Liu, B.; Yu, W.-L.; Lai, Y.-H.; Huang, W., Blue-light-emitting cationic water-soluble polyfluorene derivatives with tunable quaternization degree. Macromolecules 2002, 35 (13), 4975-4982.

66. Ahn, T.; Lee, H.; Han, S.-H., Effect of annealing of polythiophene derivative for polymer light-emitting diodes. Appl. Phys. Lett. 2002, 80 (3), 392-394.

67. Yu, W. L.; Pei, J.; Huang, W.; Heeger, A. J., Spiro-Functionalized Polyfluorene Derivatives as Blue Light-Emitting Materials. Adv. Mater. 2000, 12 (11), 828-831.

68. Scott, J.; Carter, S.; Karg, S.; Angelopoulos, M., Polymeric anodes for organic light-emitting diodes. Synth. Met. 1997, 85 (1-3), 1197-1200.

69. Zhang, B.; Qin, C.; Ding, J.; Chen, L.; Xie, Z.; Cheng, Y.; Wang, L., High-Performance All-Polymer White-Light-Emitting Diodes Using Polyfluorene Containing Phosphonate Groups as an Efficient Electron-Injection Layer. Adv. Funct. Mater. 2010, 20 (17), 2951-2957.

70. Zhao, Q.; Liu, S. J.; Huang, W., Polyfluorene-based blue-emitting materials. Macromol. Chem. Phys. 2009, 210 (19), 1580-1590.

71. van Woudenbergh, T.; Wildeman, J.; Blom, P. W.; Bastiaansen, J. J.; Langeveld-Vos, B., Electron-Enhanced Hole Injection in Blue Polyfluorene-Based Polymer Light-Emitting Diodes. Adv. Funct. Mater. 2004, 14 (7), 677-683.

72. Aldred, M. P.; Contoret, A. E.; Farrar, S. R.; Kelly, S. M.; Mathieson, D.; O'Neill, M.; Tsoi, W. C.; Vlachos, P., A full-color electroluminescent device and patterned photoalignment using light-emitting liquid crystals. Adv. Mater. 2005, 17 (11), 1368-1372.

73. Ego, C.; Marsitzky, D.; Becker, S.; Zhang, J.; Grimsdale, A. C.; Müllen, K.; MacKenzie, J. D.; Silva, C.; Friend, R. H., Attaching perylene dyes to polyfluorene: three simple, efficient methods for facile color tuning of light-emitting polymers. J. Am. Chem. Soc. 2003, 125 (2), 437-443.

74. Cho, N. S.; Hwang, D.-H.; Lee, J.-I.; Jung, B.-J.; Shim, H.-K., Synthesis and color tuning of new fluorene-based copolymers. Macromolecules 2002, 35 (4), 1224-1228.

75. Bhowmik, P. K.; Kamatam, S.; Han, H.; Nedeltchev, A. K., Synthesis and characterization of poly (pyridinium salt) s with oxyalkylene units exhibiting amphotropic liquid–crystalline and photoluminescence properties. Polym. 2008, 49 (7), 1748-1760.

76. Neher, D., Polyfluorene homopolymers: conjugated liquid-crystalline polymers for bright blue emission and polarized electroluminescence. Macromol. Rapid Commun. 2001, 22 (17), 1365-1385.

77. Oda, M.; Nothofer, H. G.; Lieser, G.; Scherf, U.; Meskers, S.; Neher, D., Circularly polarized electroluminescence from liquid-crystalline chiral polyfluorenes. Adv. Mater. 2000, 12 (5), 362-365.

78. Grell, M.; Bradley, D. D.; Inbasekaran, M.; Woo, E. P., A glass-forming conjugated main-chain liquid crystal polymer for polarized electroluminescence applications. Adv. Mater. 1997, 9 (10), 798-802.

79. Chen, J.-W.; Huang, C.-C.; Chao, C.-Y., Supramolecular liquid-crystal gels formed by polyfluorene-based π-conjugated polymer for switchable anisotropic scattering device. ACS Appl. Mater. Interfaces 2014, 6 (9), 6757-6764.

80. Lin, H.-W.; Lin, C.-L.; Chang, H.-H.; Lin, Y.-T.; Wu, C.-C.; Chen, Y.-M.; Chen, R.-T.; Chien, Y.-Y.; Wong, K.-T., Anisotropic optical properties and molecular orientation in vacuum-deposited ter (9, 9-diarylfluorene) s thin films using spectroscopic ellipsometry. J. Appl. Phys. 2004, 95 (3), 881-886.

81. Yang, X.; Neher, D.; Lucht, S.; Nothofer, H.; Güntner, R.; Scherf, U.; Hagen, R.; Kostromine, S., Efficient polarized light-emitting diodes utilizing ultrathin photoaddressable alignment layers. Appl. Phys. Lett. 2002, 81 (13), 2319-2321.

82. Wegner, G., Ultrathin films of polymers: architecture, characterization and properties. Thin Solid Films 1992, 216 (1), 105-116.

83. Alvarez, S.; Marcasuzaa, P.; Billon, L., Bio-Inspired Silica Films Combining Block Copolymers Self-Assembly and Soft Chemistry: Paving the Way toward Artificial Exosqueleton of Seawater Diatoms. Macromol. Rapid Commun. 2020, 2000582.

84. Galeotti, F.; Pisco, M.; Cusano, A., Self-assembly on optical fibers: a powerful nanofabrication tool for next generation "lab-on-fiber" optrodes. Nanoscale 2018, 10 (48), 22673-22700.

85. Zhang, J.; Chen, X.-F.; Wei, H.-B.; Wan, X.-H., Tunable assembly of amphiphilic rod–coil block copolymers in solution. Chem. Soc. Rev. 2013, 42 (23), 9127-9154.

86. Xie, L.-H.; Yang, S.-H.; Lin, J.-Y.; Yi, M.-D.; Huang, W., Fluorene-based macromolecular nanostructures and nanomaterials for organic (opto) electronics. Philos. T. R. Soc. A 2013, 371 (2000), 20120337.

87. Cushen, J. D.; Otsuka, I.; Bates, C. M.; Halila, S.; Fort, S.; Rochas, C.; Easley, J. A.; Rausch, E. L.; Thio, A.; Borsali, R., Oligosaccharide/silicon-containing block copolymers with 5 nm features for lithographic applications. ACS Nano 2012, 6 (4), 3424-3433.

88. Verduzco, R.; Botiz, I.; Pickel, D. L.; Kilbey, S. M.; Hong, K.; Dimasi, E.; Darling, S. B., Polythiophene-block-polyfluorene and Polythiophene-block-poly (fluorene-co-benzothiadiazole): Insights into the Self-Assembly of All-Conjugated Block Copolymers. Macromolecules 2011, 44 (3), 530-539.

89. Lee, Y.-H.; Yen, W.-C.; Su, W.-F.; Dai, C.-A., Self-assembly and phase transformations of π-conjugated block copolymers that bend and twist: from rigid-rod nanowires to highly curvaceous gyroids. Soft Matter 2011, 7 (21), 10429-10442.

90. Slota, J. E.; He, X.; Huck, W. T., Controlling nanoscale morphology in polymer photovoltaic devices. Nano Today 2010, 5 (3), 231-242.

91. Zhang, Z.-J.; Qiang, L.-L.; Liu, B.; Xiao, X.-Q.; Wei, W.; Peng, B.; Huang, W., Synthesis and characterization of a novel water-soluble block copolymer with a rod–coil structure. Mater. Lett. 2006, 60 (5), 679-684.

92. Wang, J.-J.; Zhou, Y.-N.; Wang, P.; Luo, Z.-H., The synthesis and enhancement of the surface properties of polyfluorene-based photoelectric materials by introducing fluoromonomers. RSC Adv. 2013, 3 (15), 5045-5055.

93. Liu, N.; Qi, C.-G.; Wang, Y.; Liu, D.-F.; Yin, J.; Zhu, Y.-Y.; Wu, Z.-Q., Solvent-Induced White-Light Emission of Amphiphilic Rod–Rod Poly (3-triethylene glycol thiophene)-block-poly (phenyl isocyanide) Copolymer. Macromolecules 2013, 46 (19), 7753-7758.

94. Gutacker, A.; Lin, C.-Y.; Ying, L.; Nguyen, T.-Q.; Scherf, U.; Bazan, G. C., Cationic Polyfluorene-b-Neutral Polyfluorene "Rod–Rod" Diblock Copolymers. Macromolecules 2012, 45 (11), 4441-4446.

95. Knaapila, M.; Evans, R.; Gutacker, A.; Garamus, V.; Torkkeli, M.; Adamczyk, S.; Forster, M.; Scherf, U.; Burrows, H., Solvent Dependent Assembly of a Polyfluorene− Polythiophene "Rod− Rod" Block Copolyelectrolyte: Influence on Photophysical Properties. Langmuir 2010, 26 (7), 5056-5066.

96. Scherf, U.; Adamczyk, S.; Gutacker, A.; Koenen, N., All-Conjugated, Rod-Rod Block Copolymers-Generation and Self-Assembly Properties. Macromol. Rapid Commun. 2009, 30 (13), 1059-1065.

97. Scherf, U.; Gutacker, A.; Koenen, N., All-conjugated block copolymers. Acc. Chem. Res. 2008, 41 (9), 1086-1097.

98. Rubatat, L.; Kong, X.; Jenekhe, S. A.; Ruokolainen, J.; Hojeij, M.; Mezzenga, R., Self-assembly of polypeptide/π-conjugated polymer/polypeptide triblock copolymers in rod− rod− rod and coil− rod− coil conformations. Macromolecules 2008, 41 (5), 1846-1852.

99. Park, J. Y.; Koenen, N.; Forster, M.; Ponnapati, R.; Scherf, U.; Advincula, R., Interplay of Vesicle and Lamellae Formation in an Amphiphilic Polyfluorene-b-polythiophene All-Conjugated Diblock Copolymer at the Air− Water Interface. Macromolecules 2008, 41 (16), 6169-6175.

100. Olsen, B. D.; Segalman, R. A., Self-assembly of rod–coil block copolymers. Mater. Sci. 2008, 62 (2), 37-66.

101. Kros, A.; Jesse, W.; Metselaar, G. A.; Cornelissen, J. J., Synthesis and Self-Assembly of Rod–Rod Hybrid Poly (γ-benzyl L-glutamate)-block-Polyisocyanide Copolymers. Angew. Chem. 2005, 117 (28), 4423-4426.

102. Kong, X.; Jenekhe, S. A., Block copolymers containing conjugated polymer and polypeptide sequences: synthesis and self-assembly of electroactive and photoactive nanostructures. Macromolecules 2004, 37 (22), 8180-8183.

103. Jiang, D.-H.; Kobayashi, S.; Jao, C.-C.; Mato, Y.; Isono, T.; Fang, Y.-H.; Lin, C.-C.; Satoh, T.; Tung, S.-H.; Kuo, C.-C., Light Down-Converter Based on Luminescent Nanofibers from the Blending of Conjugated Rod-Coil Block Copolymers and Perovskite through Electrospinning. Polymers 2020, 12 (1), 84.

104. Au-Duong, A.-N.; Wu, C.-C.; Li, Y.-T.; Huang, Y.-S.; Cai, H.-Y.; Jo Hai, I.; Cheng, Y.-H.; Hu, C.-C.; Lai, J.-Y.; Kuo, C.-C., Synthetic Concept of Intrinsically Elastic Luminescent Polyfluorene-Based Copolymers via RAFT Polymerization. Macromolecules 2020.

105. Zhou, M.; Li, J.; Zhang, H.; Hong, K., Stimuli-responsive fiber-like micelles from the self-assembly of well-defined rod-coil block copolymer. Eur. Polym. J. 2018, 103, 304-311.

106. Hsieh, H.-C.; Hung, C.-C.; Watanabe, K.; Chen, J.-Y.; Chiu, Y.-C.; Isono, T.; Chiang, Y.-C.; Reghu, R. R.; Satoh, T.; Chen, W.-C., Unraveling the stress effects on the optical properties of stretchable rod-coil polyfluorene-poly (n-butyl acrylate) block copolymer thin films. Polym. Chem. 2018, 9 (27), 3820-3831.

107. Wu, W.-C.; Chen, C.-Y.; Lee, W.-Y.; Chen, W.-C., Stimuli-responsive conjugated rod-coil block copolymers: Synthesis, morphology, and applications. Polymers 2015, 65, A1-A16.

108. Saito, K.; Isono, T.; Sun, H.-S.; Kakuchi, T.; Chen, W.-C.; Satoh, T., Rod–coil type miktoarm star copolymers consisting of polyfluorene and polylactide: precise synthesis and structure–morphology relationship. Polym. Chem. 2015, 6 (39), 6959-6972.

109. Chiu, Y.-C.; Shih, C.-C.; Chen, W.-C., Nonvolatile memories using the electrets of conjugated rod-coil block copolymer and its nanocomposite with single wall carbon nanotubes. J. Mater. Chem. C 2015, 3 (3), 551-558.

110. Wang, Q., Theory and simulation of the self-assembly of rod–coil block copolymer melts: recent progress. Soft Matter 2011, 7 (8), 3711-3716.

111. Liu, C.-L.; Lin, C.-H.; Kuo, C.-C.; Lin, S.-T.; Chen, W.-C., Conjugated rod–coil block copolymers: Synthesis, morphology, photophysical properties, and stimuli-responsive applications. Prog. Polym. Sci. 2011, 36 (5), 603-637.

112. Richard, F.; Brochon, C.; Leclerc, N.; Eckhardt, D.; Heiser, T.; Hadziioannou, G., Design of a Linear Poly (3-hexylthiophene)/Fullerene-Based Donor-Acceptor Rod-Coil Block Copolymer. Macromol. Rapid Commun. 2008, 29 (11), 885-891.

113. Ma, Z.; Qiang, L.; Zheng, Z.; Wang, Y.; Zhang, Z.; Huang, W., Morphology and photophysical properties of a thermally responsive fluorescent material based on a rod-coil tri-block copolymer. J. Appl. Polym. Science 2008, 110 (1), 18-22.

114. Kuo, C. C.; Tung, Y. C.; Lin, C. H.; Chen, W. C., Novel Luminescent Electrospun Fibers Prepared From Conjugated Rod–Coil Block Copolymer of Poly [2, 7-(9, 9-dihexylfluorene)]-block-Poly (methyl methacrylate). Macromol. Rapid Commun. 2008, 29 (21), 1711-1715.

115. Wu, W.-C.; Tian, Y.; Chen, C.-Y.; Lee, C.-S.; Sheng, Y.-J.; Chen, W.-C.; Alex, K.-Y. J., Theoretical and experimental studies on the surface structures of conjugated rod− coil block copolymer brushes. Langmuir 2007, 23 (5), 2805-2814.

116. Tung, Y. C.; Wu, W. C.; Chen, W. C., Morphological Transformation and Photophysical Properties of Rod-Coil Poly [2, 7-(9, 9-dihexylfluorene)]-block-poly (acrylic acid) in Solution. Macromol. Rapid Commun. 2006, 27 (21), 1838-1844.

117. Lu, S.; Liu, T.; Ke, L.; Ma, D.-G.; Chua, S.-J.; Huang, W., Polyfluorene-based light-emitting rod− coil block copolymers. Macromolecules 2005, 38 (20), 8494-8502.

118. Chochos, C. L.; Kallitsis, J. K.; Gregoriou, V. G., Rod− Coil Block Copolymers Incorporating Terfluorene Segments for Stable Blue Light Emission. J. Phys. Chem. B 2005, 109 (18), 8755-8760.

119. Tu, G.; Li, H.; Forster, M.; Heiderhoff, R.; Balk, L. J.; Scherf, U., Conjugated triblock copolymers containing both electron-donor and electron-acceptor blocks. Macromolecules 2006, 39 (13), 4327-4331.

120. Asawapirom, U.; Güntner, R.; Forster, M.; Scherf, U., Semiconducting block copolymers—synthesis and nanostructure formation. Thin Solid Films 2005, 477 (1-2), 48-52.

121. Scherf, U.; List, E. J., Semiconducting polyfluorenes—towards reliable structure–property relationships. Adv. Mater. 2002, 14 (7), 477-487.

122. Schmitt, C.; Nothofer, H. G.; Falcou, A.; Scherf, U., Conjugated polyfluorene/polyaniline block copolymers. Macromol. Rapid Commun. 2001, 22 (8), 624-628.

123. Tu, G.; Li, H.; Forster, M.; Heiderhoff, R.; Balk, L. J.; Sigel, R.; Scherf, U., Amphiphilic conjugated block copolymers: synthesis and solvent-selective photoluminescence quenching. Small 2007, 3 (6), 1001-1006.

124. Van Horn, R. M.; Steffen, M. R.; O'Connor, D., Recent progress in block copolymer crystallization. Polym. Crystallization 2018, 1 (4), e10039.

125. Ban, M.; Zou, Y.; Rivett, J. P.; Yang, Y.; Thomas, T. H.; Tan, Y.; Song, T.; Gao, X.; Credgington, D.; Deschler, F., Solution-processed perovskite light emitting diodes with efficiency exceeding 15% through additive-controlled nanostructure tailoring. Nat. Commun. 2018, 9 (1), 1-10.

126. Tao, Y.; Ma, B.; Segalman, R. A., Self-assembly of rod− coil block copolymers and their application in electroluminescent devices. Macromolecules 2008, 41 (19), 7152-7159.

127. Wang, J.-T.; Saito, K.; Wu, H.-C.; Sun, H.-S.; Hung, C.-C.; Chen, Y.; Isono, T.; Kakuchi, T.; Satoh, T.; Chen, W.-C., High-performance stretchable resistive memories using donor–acceptor block copolymers with fluorene rods and pendent isoindigo coils. NPG Asia Mater. 2016, 8 (8), e298-e298.

128. Lin, S.-T.; Tung, Y.-C.; Chen, W.-C., Synthesis, structures and multifunctional sensory properties of poly [2, 7-(9, 9-dihexylfluorene)]-block-poly [2-(dimethylamino) ethyl methacrylate] rod-coil diblock copolymers. J. Mater. Chem. C 2008, 18 (33), 3985-3992.

129. Tung, Y.-C.; Chen, W.-C., Poly [2, 7-(9, 9-dihexylfluorene)]-block-poly [3-(trimethoxysilyl) propyl methacrylate](PF-b-PTMSPMA) rod-coil block copolymers: Synthesis, morphology and photophysical properties in mixed solvents. React. Funct. Polym. 2009, 69 (7), 507-518.

130. Chochos, C. L.; Tzanetos, N. P.; Economopoulos, S. P.; Gregoriou, V. G.; Kallitsis, J. K., New rod–coil block copolymers consisting of terfluorene segments and electron transporting units as the flexible blocks. Eur. Polym. J. 2007, 43 (12), 5065-5075.

131. Chochos, C. L.; Tsolakis, P. K.; Gregoriou, V. G.; Kallitsis, J. K., Influence of the Coil Block on the Properties of Rod− Coil Diblock Copolymers with Oligofluorene as the Rigid Segment. Macromolecules 2004, 37 (7), 2502-2510.

132. Tsolakis, P. K.; Kallitsis, J. K., Synthesis and Characterization of Luminescent Rod–Coil Block Copolymers by Atom Transfer Radical Polymerization: Utilization of Novel End-Functionalized Terfluorenes as Macroinitiators. Chem. Eur. J. 2003, 9 (4), 936-943.

133. Marsitzky, D.; Klapper, M.; Müllen, K., End-Functionalization of Poly (2, 7-fluorene): A Key Step toward Novel Luminescent Rod− Coil Block Copolymers. Macromolecules 1999, 32 (25), 8685-8688.

134. Jin, Z.; Fan, H., Self-assembly of nanostructured block copolymer nanoparticles. Soft Matter 2014, 10 (46), 9212-9219.

135. Qiang, L.; Ma, Z.; Zheng, Z.; Yin, R.; Huang, W., Novel Photo-Crosslinkable Light-Emitting Rod/Coil Copolymers: Underlying Facile Material for Fabricating Pixelated Displays. Macromol. Rapid Commun. 2006, 27 (20), 1779-1786.

136. Jao, C. C.; Chang, J. R.; Ya, C. Y.; Chen, W. C.; Cho, C. J.; Lin, J. H.; Chiu, Y. C.; Zhou, Y.; Kuo, C. C., Novel stretchable light-emitting diodes based on conjugated-rod block elastic-coil copolymers. Polym. Int. 2020.

137. Filiatrault, H. L.; Porteous, G. C.; Carmichael, R. S.; Davidson, G. J.; Carmichael, T. B., Stretchable light-emitting electrochemical cells using an elastomeric emissive material. Adv. Mater. 2012, 24 (20), 2673-2678.

138. Yu, Z.; Niu, X.; Liu, Z.; Pei, Q., Intrinsically stretchable polymer light-emitting devices using carbon nanotube-polymer composite electrodes. Adv. Mater. 2011, 23 (34), 3989-3994.

139. Someya, T., Tiny lamps to illuminate the body. Nat. Mater. 2010, 9 (11), 879-880.

140. Viventi, J.; Kim, D.-H.; Moss, J. D.; Kim, Y.-S.; Blanco, J. A.; Annetta, N.; Hicks, A.; Xiao, J.; Huang, Y.; Callans, D. J., A conformal, bio-interfaced class of silicon electronics for mapping cardiac electrophysiology. Sci. Transl. Med. 2010, 2 (24), 24ra22-24ra22.

141. Sun, P.; Qiu, M.; Li, M.; Mai, W.; Cui, G.; Tong, Y., Stretchable Ni@ NiCoP textile for wearable energy storage clothes. Nano Energy 2019, 55, 506-515.

142. Gao, M.; Li, L.; Song, Y., Inkjet printing wearable electronic devices. J. Mater. Chem. C 2017, 5 (12), 2971-2993.

Chapter 2

Facile Preparation of Cu/Ag Core/Shell Nanofiber as High Flexible Transparent Conductive Electrodes for Polyfluorene Light-Emitting Diode Devices

2.1 Introduction

Polymer light-emitting diodes (PLEDs) have been envisioned to be miniaturized into accessories, including wearable and stretchable electronics that permit both stretchability and portability, as described in **Section 1.2.3**. However, the wildly commercialized transparent electrode, indium tin oxide (ITO), is brittle and even crack happened under small tensile stain. Therefore, PLEDs fabricated on ITO coated flexible substrates have limited flexibility. To conquer the flexibility of PLED, a variety of transparent conductive electrodes (TCEs) with mechanical flexibility or rubbery stretchability have been investigated as compliant electrodes to replace the rigid ITO, including conducting polymer,[1] carbon nanotubes (CNTs),[2] graphenes,[3] and metal nanowire,[4-7] *etc.*

Silver nanowires (AgNWs) spray-coating onto various flexible substrates have been reported as the most promising method to develop with high conductivity and transmittance (*T*). However, the high price of silver (Ag) (US $505/kg) limits the potential for mass production of AgNWs. Another alternative metal is copper (Cu), which is not only 80 times cheaper (US $6.36/kg) than Ag but also possesses low sheet resistance (R_s ~16.8 Ω sq^{-1}) as silver (R_s ~15.9 Ω sq^{-1}).[8] These properties of the copper nanowire (CuNW) have shown promise to rival silver in excellent electrical conductivity, optical transparency, and mechanical flexibility.[9-11] Nevertheless, there is one critical problem with Cu, easily oxidized by moisture and oxygen, which greatly reduces their conductivity. Many studies have focused on using

double metals or materials to enhance the performance of conductive films. For example, Jiang and Fong *et al*. have reported amidoxime surface-functionalized polyacrylonitrile (ASFPAN) nanofiber (NF) webs surface-decorated with silver nanoparticles (AgNPs), and the density and size of AgNPs have a major effect on the activity and sensitivity of surface-enhanced Raman scattering.[12] Lee *et al*. have successfully synthesized a core/shell nanostructure of CuNWs/graphene and demonstrated remarkable thermal oxidation and chemical stability because of the tight encapsulation of CuNW with gas-impermeable graphene shell.[13] These studies have indicated that composite materials can considerably improve performance, but in some cases, the process is extremely complicated or the instrumentation remains to be expensive.

On the other hand, electrospinning (ES) technique is used to prepare NF webs from polymers that provide a facile method to interweave a continuous NF web with many advantages; such as low-cost, uniform, and nanoscale diameters (10-1000 nm), and high surface area.[14-16] These advantages endow various applications of NFs, for example, the sensing of pH level or metal ions,[17] electronic textiles,[18-19] and wearable devices.[19-21] Researchers have reported electrospun NFs prepared from polymers blended with AgNWs or silver particles (AgNPs), which have become considerable attention in developing TCEs. For example, Cui *et al*. have successfully utilized Cu-NFs to fabricate high-performing TCEs through ES. The Cu NF webs have ultrahigh aspect ratios and a fused crossing point with

ultralow junction resistances, which result in lower sheep resistance (R_s) at high transmittance (T) (50 Ω sq^{-1} at 90%).[22] Yoon *et al*. have successfully fabricated Ag-decorated and palladium-coated Cu-electroplated fibers with high electrical conductivity via ES.[23] Both are the only reports that have described the application of Cu-NFs or Cu/metal-NFs in TCEs via the ES technique. These studies inspired the author to fabricate electrospun-based TCEs by performing the core/shell architecture via using a combination of ES and chemical.

According to the above-mentioned, Cu may be the best candidate to prepare metal electrospun NFs considering the price is cheaper than Ag while has a low R_s. In this chapter, the author proposes a novel strategy in which TCEs are prepared from Cu/Ag core/shell NFs via using a combination of ES and chemical reduction, which is not only facile but also a low-cost method for forming Ag layers to avoid Cu-NFs from oxidation, as shown in **Figure 2.1**. TCEs based on Cu/Ag core/shell NFs are characterized by high conductivity, transparency, and stability through an ES and reduction-oxidation heating process. To fulfill flexible PLED, the LED with blue emitter poly(9,9-di-*n*-octyl-2,7-fluorene) (PFO) are demonstrated by using Cu/Ag core/shell NF electrodes.

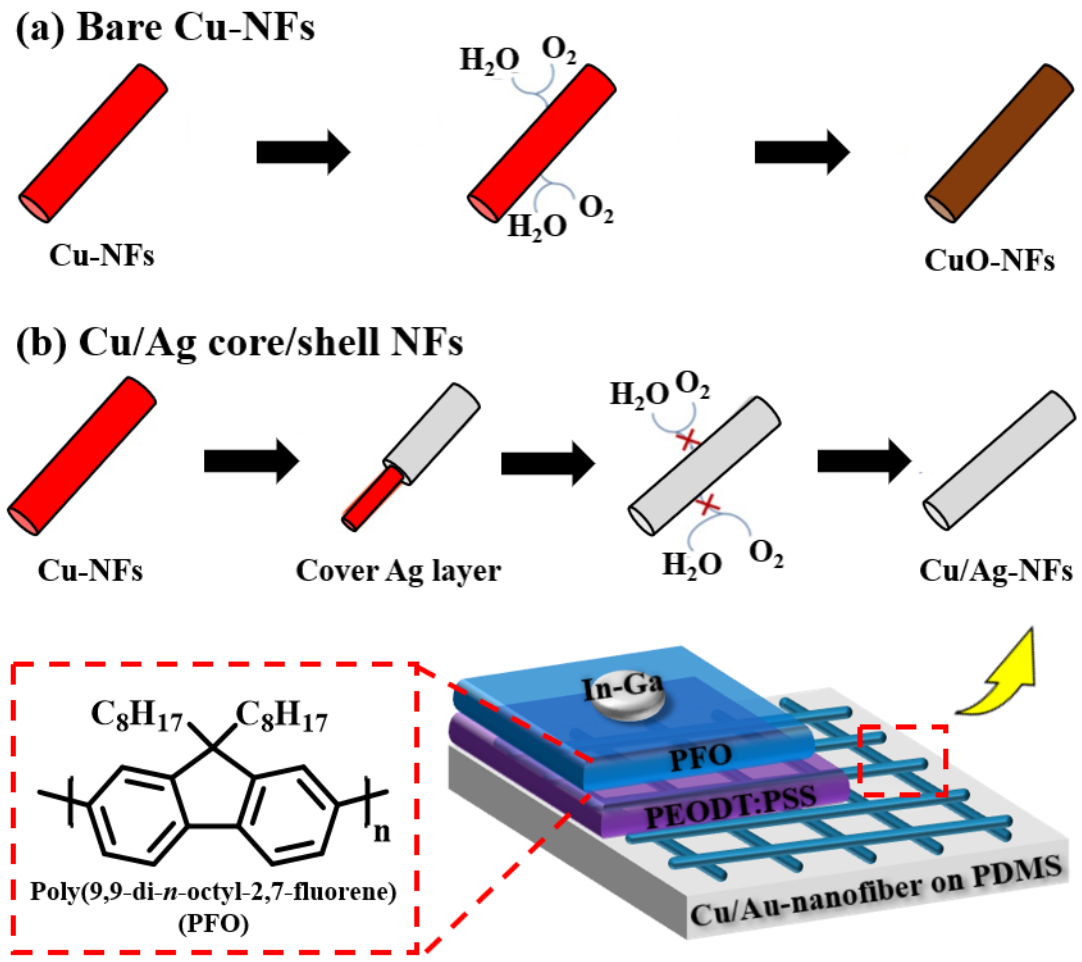

Figure 2.1. Scheme of comparing the oxidation resistance of bare Cu-NFs and Cu/Ag core/shell NFs. (a) Bare Cu-NFs and (b) Cu/Ag core/ shell NFs for high flexible PLED with blue emitter poly(9,9-di-*n*-octyl-2,7-fluorene) (PFO).

2.2 Experimental Section

2.2.1 Material

Polyvinylpyrrolidone (PVP) (*M*w = 1,300,000, 99% hydrolyzed), copper(II) acetate ($CuAc_2$), methanol (MeOH, ≥99%), ammonium hydroxide solution (NH_4OH, 28.0%–30.0% NH_3 basis), silver nitrate ($AgNO_3$, 99% hydrolyzed), poly(9,9-di-*n*-octyl-2,7-fluorene) (PFO, M_n ~ 10,000, $Đ$ ~ 2), poly(3,4-ethylene dioxythiophene) polystyrene sulfonate (PEDOT:PSS, Clevios, PH1000), and indium–gallium eutectic (EGAln, ≥99.99%) are purchased from Sigma-Aldrich, Saint Louis, USA. Polydimethylsiloxane precursors (PDMS, Sylgard 184) is purchased from Dow Corning Corporation, Midland, USA.

2.2.2 Characterization

Field emission scanning electron microscopy (FE-SEM) and energy-dispersive x-ray spectroscopy (EDX) analyses are carried out JEOL JSM-7600F (JEOL, Tokyo, Japan) equipped with energy-dispersive. High-resolution transmission electron microscopy (HR-TEM) analyses are measured by using JEOL JEM-2100F (JEOL, Tokyo, Japan). The characterization of the X-ray powder diffraction (XRD) patterns is recorded using Cu Kα radiation (λ = 1.5418 Å) on a D2 Bruker diffractometer operating at 40 kV and 20 mA. The T and R_s are analyzed based on UV-visible spectra (Jasco V-730, Sendai, Japan) and Keithley 4200 semiconductor

parametric analyzer. Current density-voltage (*J*-*V*) and luminance-voltage (*L*-*V*) characteristics are conducted in ambient air using a photo research PR-670 spectroradiometer.

2.2.3 Preparation of $CuAc_2$/PVP-NFs

First, the PVP is dissolved in deionized water in 10 wt% and then mixed with $CuAc_2$ in various concentrations (*i.e.*, 10, 15, and 20 wt%). Second, a metallic needle is connected to a high-voltage power supply, and aluminum (Al) foil is placed 20 cm below the tip of the needle to collect NFs during the ES **(Figure 2.2)**. The setup voltage and feed rate of the mixture are 12.9 kV, and 1 mL h^{-1}, respectively. The random, aligned, and crossed electrospun $CuAg_2$/PVP NFs are collected from Al foil. All experiments are performed at room temperature, relative humidity of approximately 20%, and 40 mins of collection.

2.2.4 Preparation of Cu-NFs by the reduction-oxidation heating method

The reduction-oxidation heating method is utilized to converted $CuAc_2$/PVP-NFs into Cu-NFs. In the oxidation step, the $CuAc_2$/PVP-NFs are placed in the quartz boat and heated to 250°C under a rate of 2 °C min^{-1} and then heat for 1 h at the maximum temperature in a constant flow of gas composed (nitrogen/oxygen = 4/1). Afterward, the $CuAc_2$/PVP-NFs are reheated to 500°C at a rate of 5 °C min^{-1} for 2 h in ambient air. After oxidation, the $CuAc_2$ is converted

into copper oxide (CuO), and the PVP is pyrolyzed in carbon dioxide. In the reduction step, CuO-NFs are placed in the quartz boat and heated to 300°C under 5 °C min^{-1} in a constant flow of argon/hydrogen gas, and then maintained at 300°C for 1 h in the tube furnace. The CuO-NFs are deoxygenated to Cu-NFs on the glass substrate.

2.2.5 Preparation of Cu/Ag core/shell NFs from Ag electroless deposition

To prepare an Ag precursor, first, stoichiometrically excess $AgNO_3$ is dissolved in deionized water to yield 30 g L^{-1} of $AgNO_3$ solution. Subsequently, NH_4OH is added into $AgNO_3$ solution drop by drop with vigorous stirring until all yellow precipitate disappeared and the solution became clear; then, Cu-NFs are immersed into the $Ag(NH_3)_2^+$ solution. Second, the Ag amine reagent is dropped onto the Cu-NFs and then immersed in di water to wash the Ag amine reagent. After immersion, Cu/Ag core/shell NFs are extracted from deionized water and dried by using an air gun.

$$AgNO_3+2NH_4OH \rightarrow [Ag(NH_3)_2]NO_3+H_2O \quad (1)$$

$$Cu + 2[Ag(NH_3)_2]NO_3 \rightarrow [Cu(NH_3)_4](NO_3)_2 + 2Ag \downarrow \quad (2)$$

2.2.6 Fabrication of polyfluorene light-emitting diode devices

PDMS thin film is prepared by spin-coating at 3000 rpm for 30 s on glass substrate and curing at 100°C for 5 mins. PDMS is peeled off from glass substrate and treated by oxygen-

plasma for 3 mins. Subsequently, Cu/Ag core/shell NFs are transferred to PDMS substrate as an anode, namely as PDMS@Cu/Ag core/shell NFs. An aqueous PEDOT:PSS is spin-coated on PDMS substrate at 1500 rpm for 30 s and annealing at 80°C for 10 mins to yield 45-50 nm thin films. An emissive PFO (dissolved in chlorobenzene 10 mg mL^{-1}) is spin-coated at 1000 rpm for 60 s and annealing at 80°C for 10 mins. Finally, the indium-gallium (Eln-Ga) is drop-coated on the top of the device as a cathode.

2.3 Results and Discussion

2.3.1 NF film morphologies and fabrications

Figure 2.2 shows the schematic of preparing Cu/Ag core/shell NFs as TCEs with varying architectures (*i.e.*, random, aligned, and crossed) through ES. The morphology of $CuAc_2$/PVP-NFs, Cu-NFs, and Cu/Ag-NFs are further investigated by FE-SEM and EDS mapping, as shown in **Figure 2.3**. Here, the author selects the $CuAc_2$/PVP concentration of 20 wt% to experiment due to the best quality of forming fibers and is shown in **Figure 2.3a-c**. To turn Cu into CuO, $CuAc_2$/PVP-NFs are oxidized by heating in air at 500°C. After reduction, CuO-NFs are further converted into Cu-NFs as displayed in **Figure 2.3d**. The roughness of Cu-NFs is increased because of the damage after heat treatment in the furnace at 500°C. To form the Ag protective layer, the Cu-NFs are immersed into an Ag-reactive solution. The FE-SEM image of Cu/Ag core/shell NFs is shown in **Figure 2.3e**. The composite Cu/Ag core/shell NFs become continuous again (Schematic illustration in **Figure 2.3f,g**). The EDX element analysis in **Figure 2.3f,g** reveals the new peaks of Cu and Ag that indicates they successfully turn $CuAc_2$/PVP-NFs into Cu/Ag core/shell NFs. As shown in **Figure 2.4**, $CuAc_2$/PVP NFs, Cu-NFs, and Cu/Ag- NFs are fabricated at an average diameter around 167 ± 56.46, 91 ± 20.16, and 202 ± 52.05 nm, respectively. The reason for a decreased diameter of Cu-NFs is because of thermal treatment, the PVP is evaporated into CO_2. The diameter of Cu/Ag core/shell NFs has increased approximately two-fold increase in the diameter that can be attributed to the

success of forming an Ag protective layer. It is worthwhile to note that the diameter of Cu/Ag-NFs can be optimized by tuning the time factors for encapsulating the Ag shell on Cu-NFs. If lesser time is used than the optimized time for electroless plating, the shell formation is not uniform, and this might retard the oxidation resistance of the core/shell structure and lower the conductivity.

The author further carried out the HR-TEM to investigate internal structures in the Cu/Ag core/shell NFs. As evidenced in **Figure 2.5a,b**, the Cu-NF lattices are observed internal to the core/shell nanostructure of Cu/Ag-NFs. The Cu lattice distance is 0.208 nm, corresponding to the lattice distance value of the (111) plane of Cu. The lattice distance of Ag protective layers in the shell is estimated to be 0.236 nm from (111) plane of Ag, as shown in **Figure 2.5b,c**. **Figure 2.5d,e** presents the high-resolution TEM images of the Cu/Ag core/shell nanostructure. Similarly, the XRD patterns of Cu and Ag are observed from Cu-NFs and Cu/Ag core/shell NFs, respectively, as illustrated in **Figure 2.6**. As evidenced in **Figure 2.6a**, it affirms the CuO-NFs is successfully turned into Cu-NFs. After the electroless plating treatment, Cu-NFs are plated onto the Ag layer and exhibit distinct diffraction peaks of Ag in the XRD pattern shown in **Figure 2.6b**. Because Ag is completely covered onto Cu-NFs, the XRD pattern is dominated by the diffraction of Ag. Both TEM and XRD results evidenced that the Cu/Ag core/shell nanostructure can be successfully prepared by using the electroless plating process, which is

easier for producing the protective layer than the low temperature plasma enhanced chemical vapor deposition (LT-PECVD) process[13] or the atomic layer deposition process.[24]

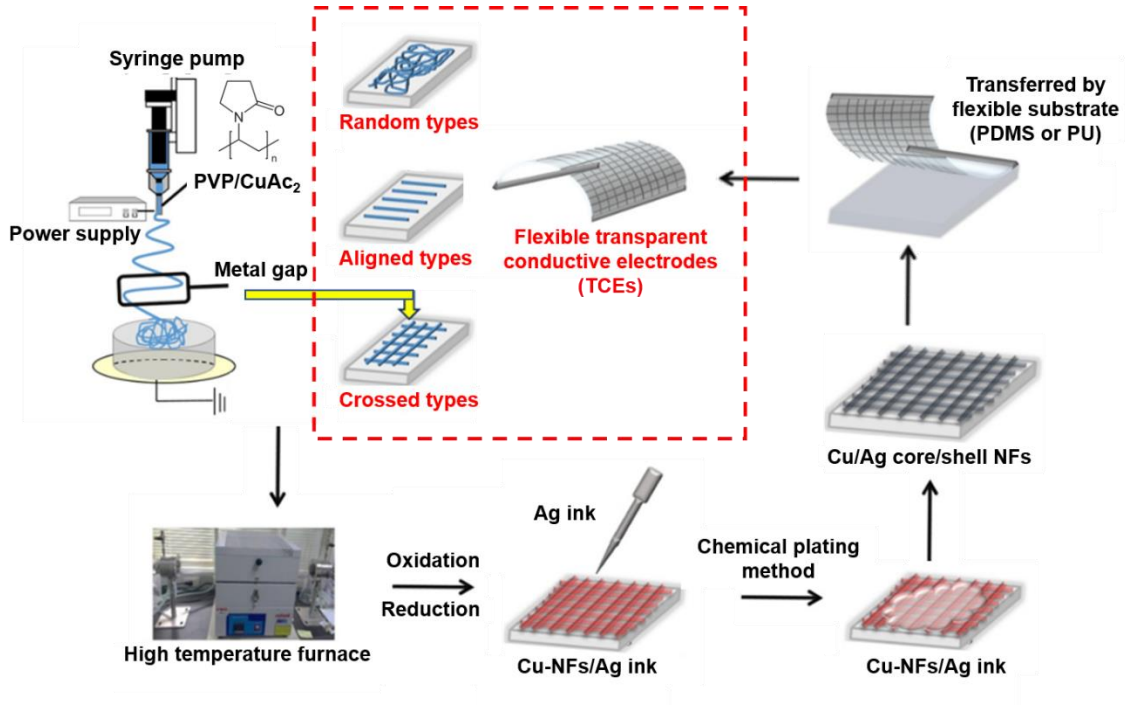

Figure 2.2. Experimental step of fabricating Cu/Ag core/shell NFs.

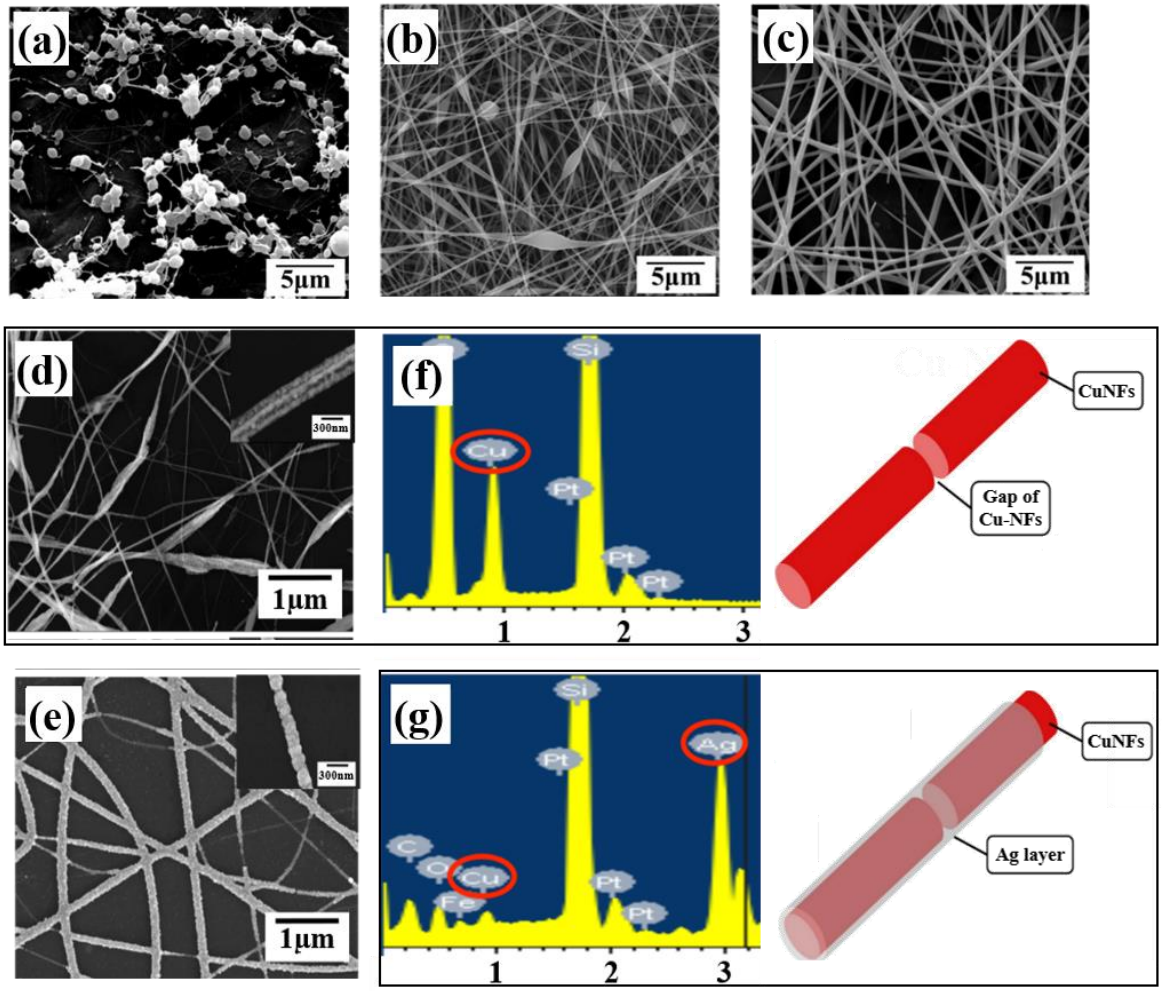

Figure 2.3. FE-SEM image of F $CuAc_2$/PVP-NFs with various concentrations: (a) 10 wt%, (b) 15 wt%, (c) 20 wt%, (d) Cu-NFs, and (e) Cu/Ag-NFs. The EDX spectrum of (f) Cu-NFs and (g) Cu/Ag-NFs.

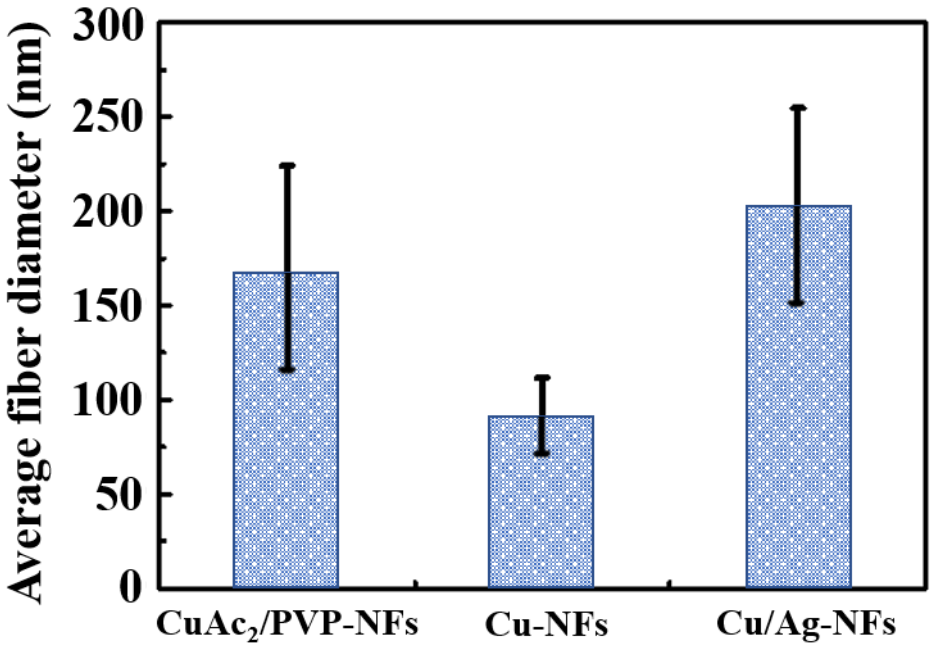

Figure 2.4. The average fiber diameter of $CuAc_2$/PVP-NFs, Cu-NFs, and Cu/Ag-NFs.

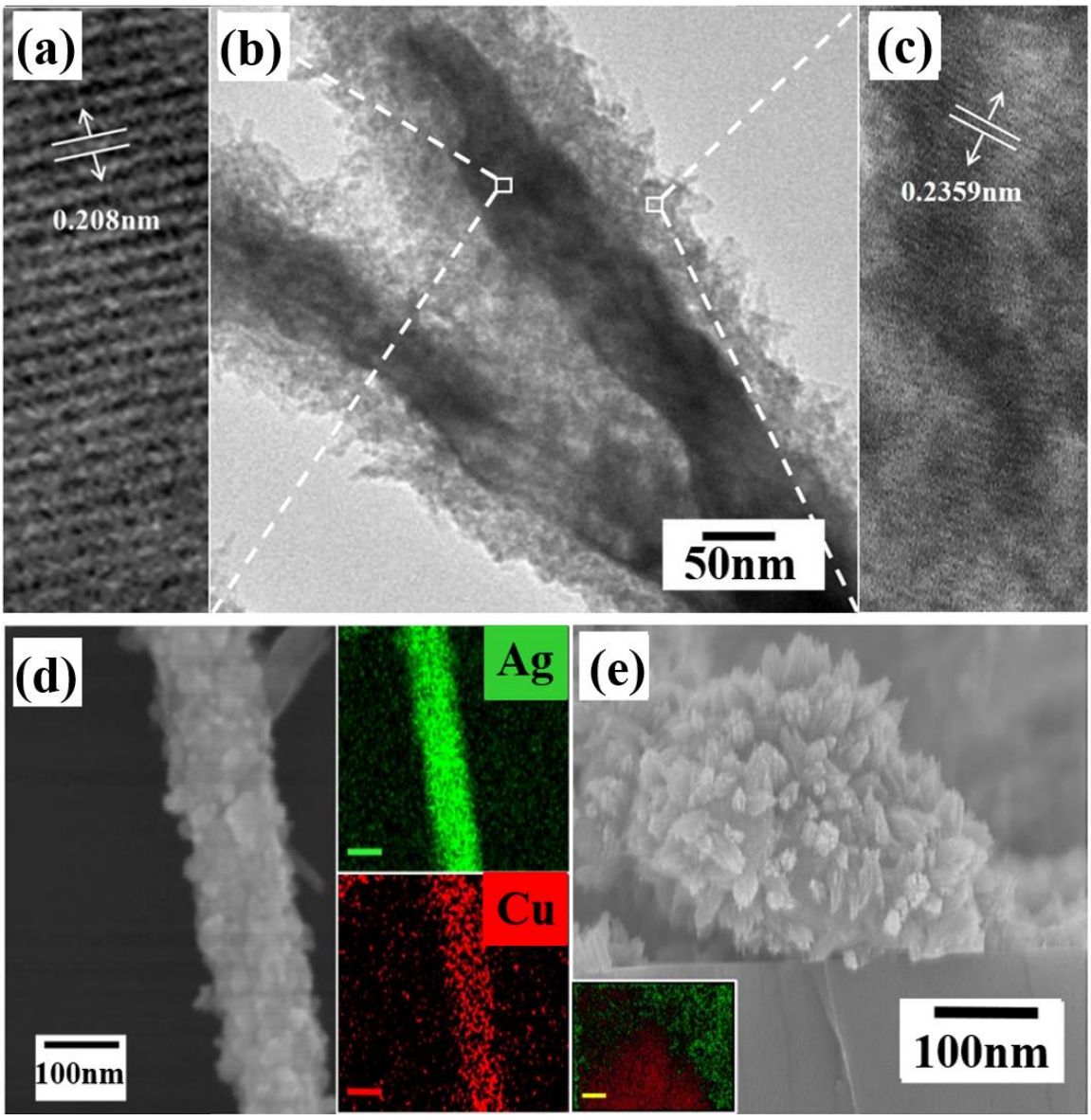

Figure 2.5. HR-TEM image of a fast Fourier transforms an inverse image of (a) the middle, (b) full, and (c) the edge of the Cu/Ag core/shell nanostructure. HR-TEM image of a fast Fourier transforms an inverse image of (d) the middle and (e) the edge of the Cu/Ag-core/shell nanostructure.

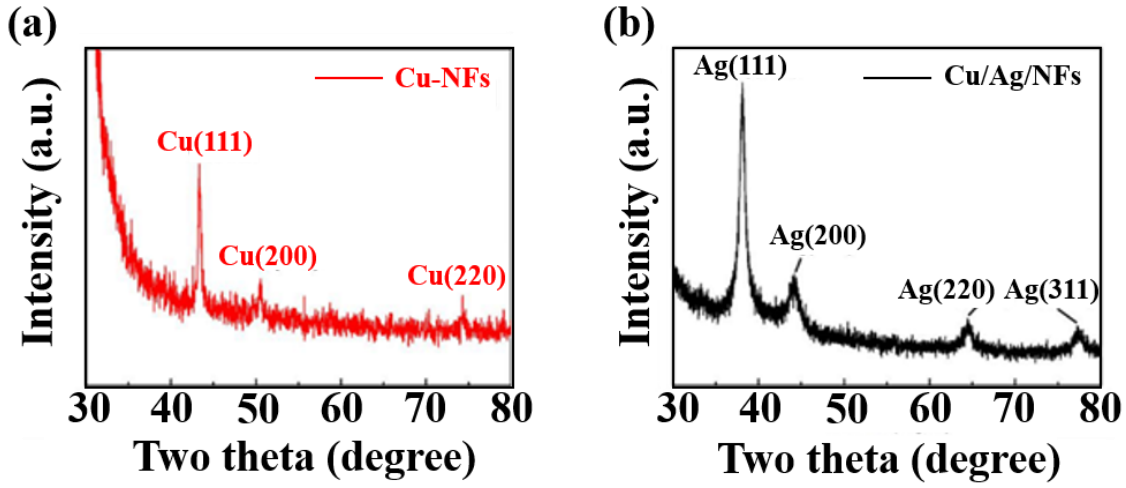

Figure 2.6. XRD patterns of (a) Cu-NFs and (b) Cu/Ag core/shell NFs.

2.3.2 Sheet resistance (R_s) and transmittance (T) of NFs

It has been widely acknowledged that the sheet resistance ratio (R_s/R_0) plays a critical role in TCE where is defined as follows: R_s = sheet resistance in displayed gases at various concentrations and R_0 = sensor resistance in fresh air. The author next places Cu-NFs and Cu/Ag core/shell NFs at a room temperature (~28°C) and average humidity of approximately 60% and observes the changing of the R_s/R_0 ratio. As depicted in **Figure 2.7a**, the R_s/R_0 ratio of Cu-NFs visibly increased approximately 1.7-fold unlike the R_s/R_0 ratio of Cu/Ag core/shell NFs only slightly increased. To increase oxidation rate to test the stability of NF TCEs, the studied samples are further measured in a harsher condition where the humidity and the temperature are controlled at 80% ± 10% and 85°C. As presented in **Figure 2.7b**, the Cu-NFs lose conductivity within 15 mins because water vapor is absorbed by the Cu-NFs which

accelerates the oxidation. In striking contrast to Cu-NFs, the Cu/Ag core/shell NFs still exhibit ultrahigh conductivity owing to the protection by the Ag shell.

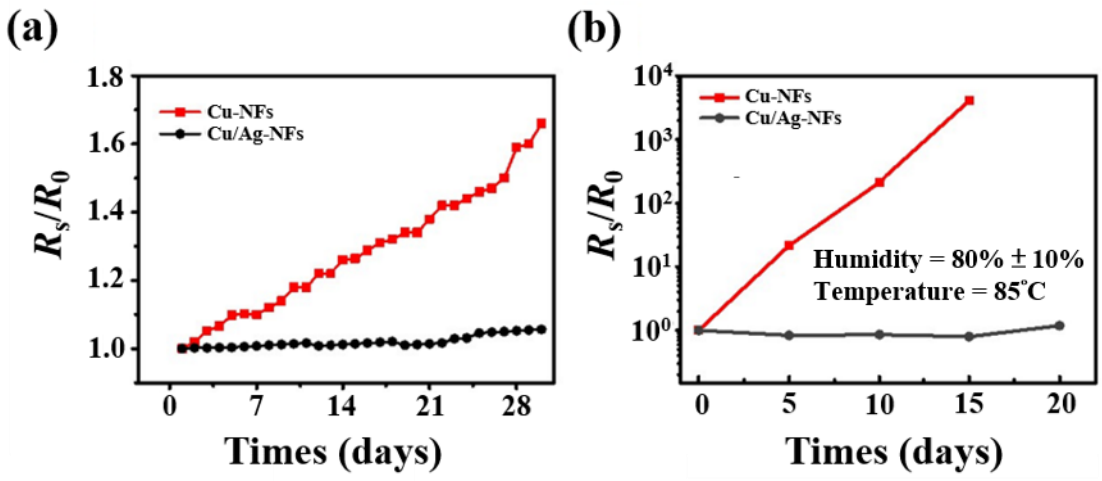

Figure 2.7. Oxidation test of Cu-NFs and Cu/Ag core/shell NFs at (a) room temperature and (b) humidity of 80% ± 10% and 85°C.

Afterward, the FE-SEM and EDS mapping images are utilized to analyze different architectures of the NFs, as displayed in **Figure 2.8**. The random, aligned, and crossed of $CuAc_2$/PVP-NFs are collected and shown in **Figure 2.8a-c**. Based on **Figure 2.8a**, the best concentration of the $CuAc_2$/PVP-NFs can get; then the aligned $CuAc_2$/PVP-NFs can be collected by changing the aluminum plate from disc to the parallels plate, as shown in **Figure 2.8b**. Therefore, the NFs can be collected on the aluminum disc, which has a rectangle gap with an area of 3cm*1.5cm. It can show the NFs, which has crossed over the rectangle gap, are lined up on the aluminum disc and covers on the hard substrate. Finally, the crossed NFs can

be collected by the repeated step with 90 degrees rotated, as shown in **Figure 2.8c**. The images of the Cu/Ag core/shell NFs are exhibited in **Figure 2.8d-f**. The results indicate similar to $CuAc_2$/PVP-NFs but with higher roughness. As depicted in **Figure 2.8g-i**, the Ag nanoparticles grow from the surface of the Cu core, which is different from using the electrospinning process to suppress the CuO nanoparticles packed into the path of ES NFs. The $CuAc_2$ had oxidized into CuO nanoparticles, but not the same that we use the electrospinning process to confine the CuO nanoparticles packed in the path of ES NF and not scattered everywhere. As shown in the EDX mapping presented in **Figure 2.8d-i**, a red/green dot can be seen which proves that Cu/Ag signals on NFs. The EDX mapping in figure 2.8g is used to prove that the inner element is Cu that is covered by the Ag protective layer.

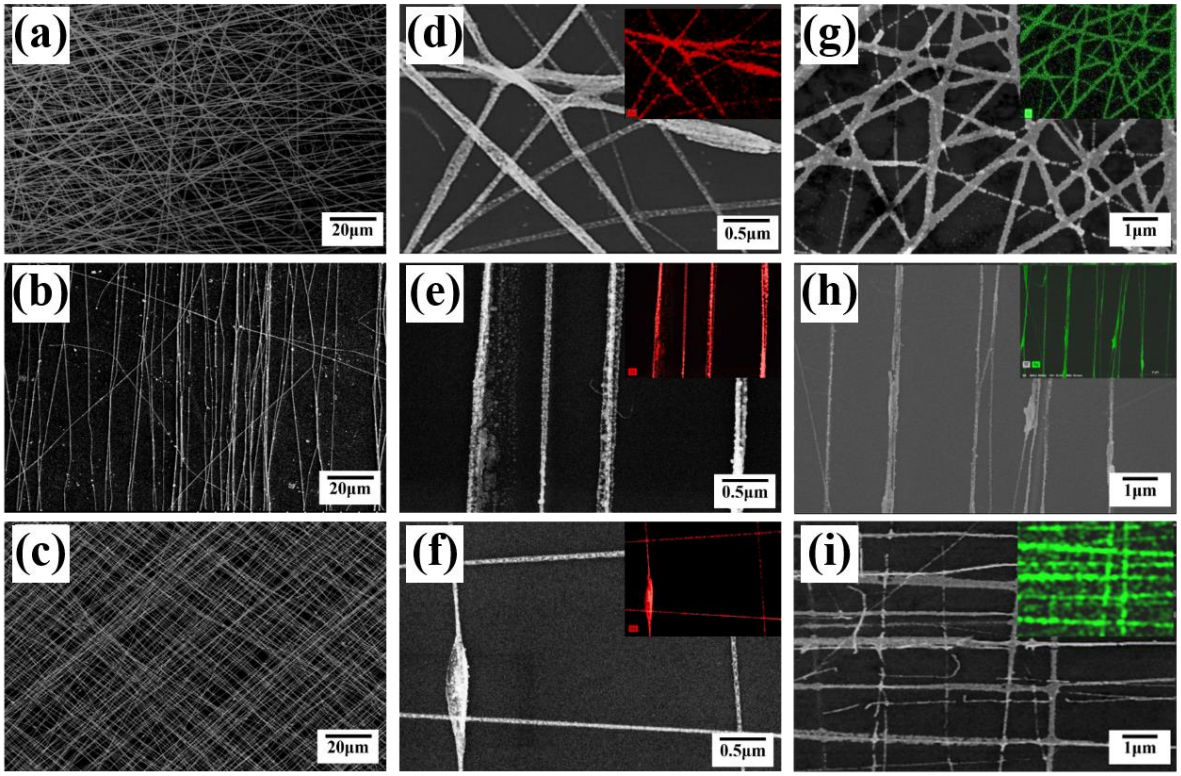

Figure 2.8. $CuAc_2$/PVP-NFs with various architectures: (a) random, (b) aligned, and (c) crossed. Cu/Ag core/shell NFs with various architectures and the EDX analysis: (d) random, (e) aligned, and (f) crossed; magnified FE-SEM images of various architectures and the EDX analysis: (g) random, (h) aligned, and (i) crossed.

Considering is also a significantly key parameter that determines the application of this. In this regard, the *T* of the Cu-NFs and Cu/Ag: core/shell NFs in different architectures are measured. In this study, the *T* is mainly dependent on the node of NFs. When the light passes through the films, the node of NFs blocks the light and causes the *T* to decrease, and therefore, the more the node has in NF films, the less the *T* is. **Figure 2.9a** shows the *T* in order of aligned-NFs > crossed-NFs > random-NFs, following the number of nodes in the NF films. As above-mentioned, forming Ag protective shell on Cu-NFs increases the diameters and roughness of the NFs, therefore, the *T* decreases by approximately 10%. A random-NF is superior to all other TCEs in terms of R_s but has a lower *T* due to the larger number of the nodes, as shown in **Figure 2.9b**. The nodes can provide multiple pathways for charge transport. As illustrated in **Figure 2.9c**, the node numbers of aligned-NFs, cross-NFs, and random-NFs are zero, two, and three, respectively, representing the node theory of *T*.

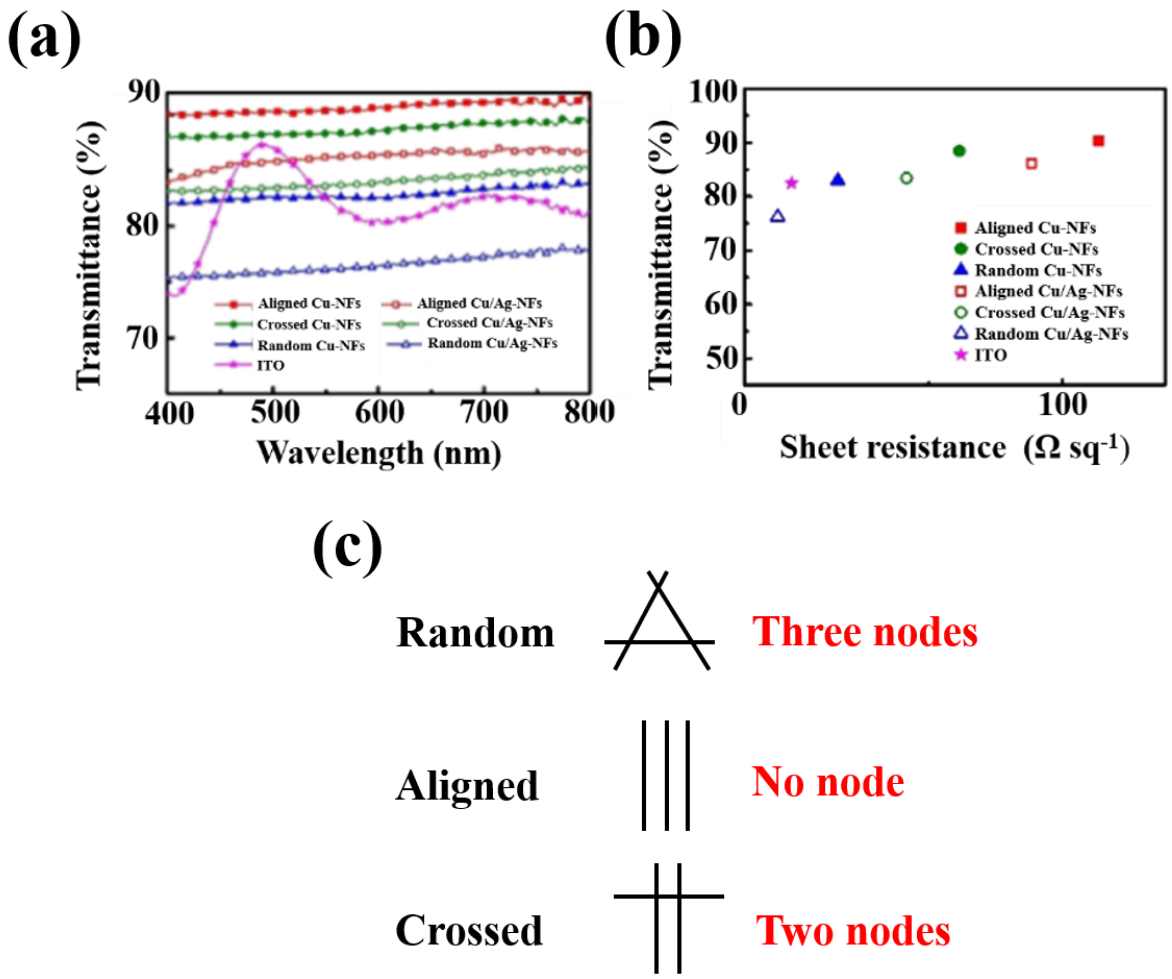

Figure 2.9. (a) Transparency test of Cu-NFs and the Cu/Ag NFs with three architectures (aligned, crossed, random). (b) transmittance (*T*) plotted against sheet resistance (R_s) by morphological type (aligned, crossed, and random) of Cu-NFs and Cu/Ag NFs. (c) Nodes theory of transmittance (*T*).

Another advantage of fabricating TCEs through ES is the R_s and *T* can be controlled by the fiber collection time. Typically, the collection time is directly proportionate to the R_s and inversely proportional to the *T*. Here, the author records five different collection times: 15, 30, 45, 60, and 75 mins. By comparison, the collection time of 45 mins is the best candidate to be

TCEs due to sufficient lower R_s and high T around 80%, as depicted in **Figure 2.10**. Subsequently, the electrospun NFs are collected approximately 45 min and optimized fiber density to tuning the best R_s and the T. As shown in **Figure 2.11**, the R_s and the T of optimized Cu/Ag core/shell NFs can be achieved approximately 7.85 Ω sq^{-1} and 78% at 550 nm.

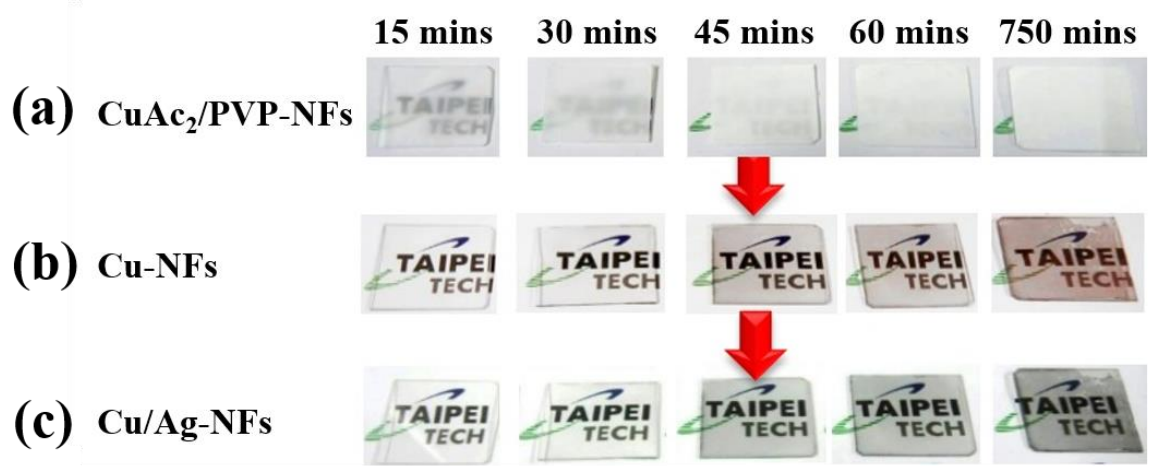

Figure 2.10. Digital photos show the color change of samples (a) $CuAc_2$/PVP-NFs (the precursor samples) (b) Cu-NFs fabricated by the thermal treatment in the H_2 atmosphere with 300°C (red color) and (c) Cu/Ag core/shell NFs fabricated by the electroless plating process with immersed Ag ink for 15 s.

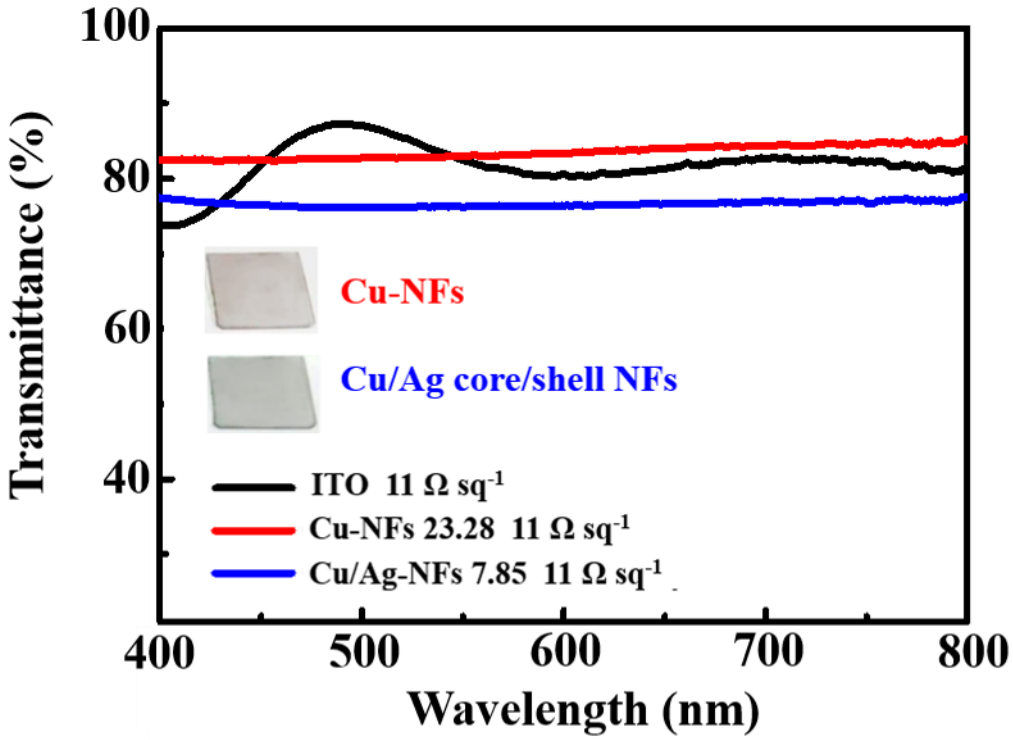

Figure 2.11. Best tuning of Cu-NFs and Cu/Ag core/shell NFs.

2.2.3 Performance of PF-based light-emitting diode devices

In this chapter, the author combines conjugated polymer poly(9,9-di-*n*-octyl-2,7-fluorene) (PFO) and high conductive Cu/Ag-NF TCEs to form fully functional PF-based light-emitting diodes (LEDs). The Cu/Ag-NFs can be easily transferred to other flexible materials (*i.e.*, polyurethane (PU) or PDMS) and chemical stability of the Cu/Ag core/shell structure is studied with an identical optimized device process under ambient air. Due to their nanoscale diameter and metallic bonding nature of Cu/Ag core/shell NFs, such TCEs should exhibit excellent flexibility, stability, and deformation. The PDMS@Cu/Ag-NFs and Eln-Ga are used as anode

and cathode, respectively. PEDOT:PSS is chosen for the hole-transport layer to improve the balance of hole and electron and commercial PFO is utilized to be as the emissive material. As shown in **Figure 2.12a**, these devices fabricated by novel NFs TCEs are not only stable but also flexible. Also, the R_s value of Cu/Ag-NF electrodes remained almost the same even after transferring to PDMS and bending around 100 times, as shown in **Figure 2.12b**. The turn-on voltage of devices is at 6V, and maximum luminance (L) is obtained of 138.6 cd m^{-2} at 12 V. The current efficiency also exhibits a rising trend with applied voltage, and saturates at 0.05 cd A^{-1} after about 12 V, as shown in **Figure 2.12c-e**. Surprisingly, the PLEDs could still emit light under 20% strain, even used intrinsically rigid conjugated PFO as an emissive layer. It can be explained that sufficient long alkyl side chains from PFO be considered the prime reason. Nevertheless, the excellent flexibility and conductivity of novel Cu/Ag-NF may open new avenues for future wearable devices.

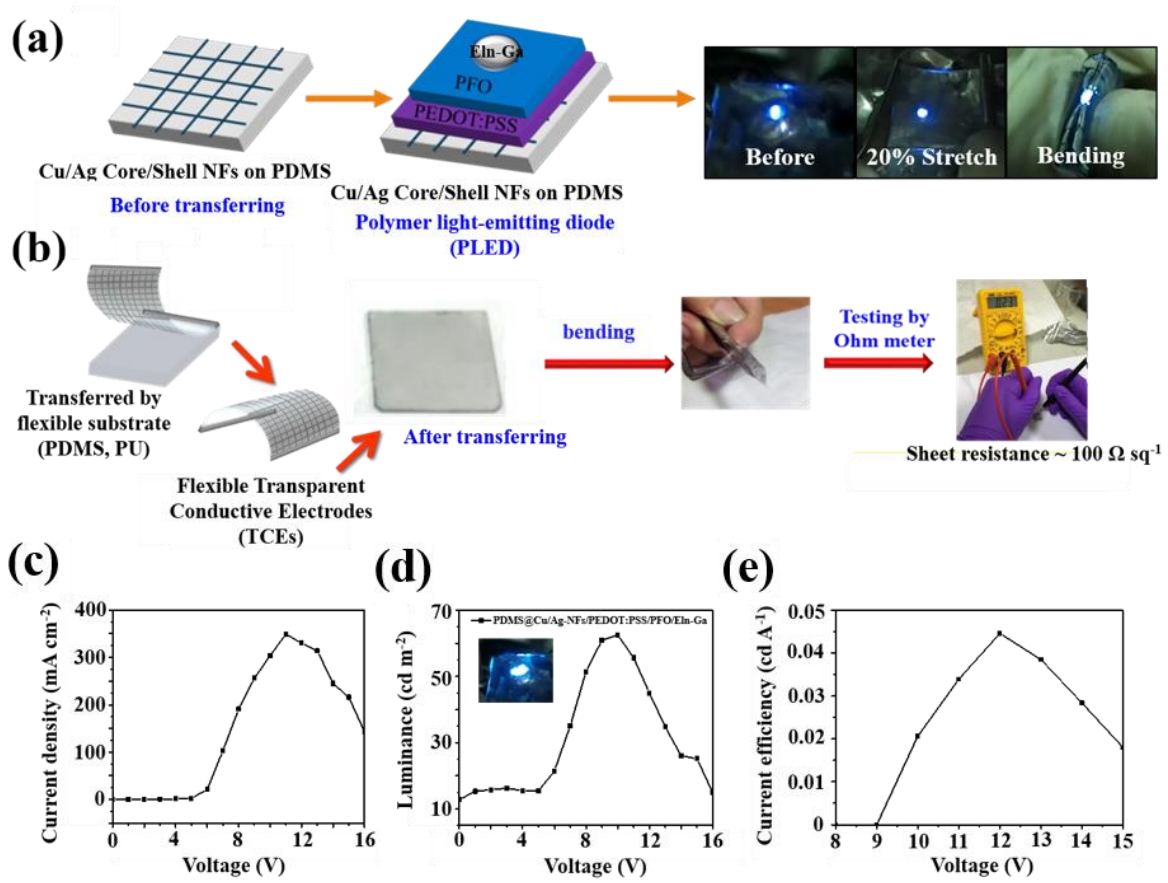

Figure 2.12. Fabrication of (a) flexible LED and (b) TCEs via transferring method to PDMS. The characteristics of PFO LEDs (c) Current density-voltage (*J*-*V*), (d) luminance-voltage (*L*-*V*), and (e) current efficiency-voltage.

2.4 Conclusions

In this chapter, the author has successfully fabricated various architectures (random, aligned, and crossed types) of Cu/Ag core/shell NFs via the chemical reduction and ES. In addition, the Cu/Ag-NF TCEs exhibit not only low R_s = 7.85 Ω sq^{-1} but also high stability because of the protection from the Ag shell. Given the extraordinary performance and cost-effectiveness of electrospun Cu/Ag -NFs as TCEs, this protective and novel method provides a critical advantage to replace ITO in the industry and commercial uses. Furthermore, a flexible and stable PFO LED has been demonstrated by using the Cu/Ag-NF TCEs. The high conductivity and excellent transparency of the fibrous films are demonstrated that they can be applied as electrodes to achieve wearable optoelectronics in the future. However, to realized a fully flexible LED the ductile emissive materil is necessary. The current state of development for flexible optoelectronics requires further investigation into high PLQY and ductile emissive polymer to make up the overall flexibility and performance of device. Exploring the synthesis of conjugated polymers with high flexibility and PLQY **(Section 1.2.3)** is of great importance for their applications in flexible LEDs. It is expected that novel multifunctional polymers can be produced and applied to the stretchable optoelectronics, such as foldable and expandable display, wearable electronic clothing, and collapsible lamp, as mentioned in **Section 1.4**.

2.5 References

1. Ma, C.; Song, Y.; Shi, J.; Zhang, D.; Zhai, X.; Zhong, M.; Guo, Q.; Liu, L., Preparation and One-step Activation of Microporous Carbon Nanofibers for Use as Supercapacitor Electrodes. Carbon 2013, 51, 290-300.

2. He, H.; Li, X.; Wang, J.; Qiu, T.; Fang, Y.; Song, Q.; Luo, B.; Zhang, X.; Zhi, L., Reduced Graphene Oxide Nanoribbon Networks: a Novel Approach Towards Scalable Fabrication of Transparent Conductive Films. Small 2013, 9 (6), 820-824.

3. Kim, K. S.; Zhao, Y.; Jang, H.; Lee, S. Y.; Kim, J. M.; Kim, K. S.; Ahn, J.-H.; Kim, P.; Choi, J.-Y.; Hong, B. H., Large-Scale Pattern Growth of Graphene Films for Stretchable Transparent Electrodes. nature 2009, 457 (7230), 706-710.

4. De, S.; Higgins, T. M.; Lyons, P. E.; Doherty, E. M.; Nirmalraj, P. N.; Blau, W. J.; Boland, J. J.; Coleman, J. N., Silver Nanowire Networks as Flexible, Transparent, Conducting Films: Extremely High DC to Optical Conductivity Ratios. ACS nano 2009, 3 (7), 1767-1774.

5. Hu, L.; Kim, H. S.; Lee, J.-Y.; Peumans, P.; Cui, Y., Scalable Coating and Properties of Transparent, Flexible, Silver Nanowire Electrodes. ACS nano 2010, 4 (5), 2955-2963.

6. Lee, J.-Y.; Connor, S. T.; Cui, Y.; Peumans, P., Solution-Processed Metal Nanowire Mesh Transparent Electrodes. Nano letters 2008, 8 (2), 689-692.

7. Madaria, A. R.; Kumar, A.; Ishikawa, F. N.; Zhou, C., Uniform, Highly Conductive, and Patterned Transparent Films of a Percolating Silver Nanowire Network on Rigid and Flexible Substrates Using a Dry Transfer Technique. Nano Research 2010, 3 (8), 564-573.

8. Rathmell, A. R.; Wiley, B. J., The Synthesis and Coating of Long, Thin Copper Nanowires to Make Flexible, Transparent Conducting Films on Plastic Substrates. Advanced Materials 2011, 23 (41), 4798-4803.

9. Sachse, C.; Weiß, N.; Gaponik, N.; Müller-Meskamp, L.; Eychmüller, A.; Leo, K., ITO-Free, Small-Molecule Organic Solar Cells on Spray-Coated Copper-Nanowire-Based Transparent Electrodes. Advanced Energy Materials 2014, 4 (2), 1300737.

10. Ye, S.; Rathmell, A. R.; Stewart, I. E.; Ha, Y.-C.; Wilson, A. R.; Chen, Z.; Wiley, B. J., A Rapid Synthesis of High Aspect Ratio Copper Nanowires for High-Performance Transparent Conducting Films. Chemical Communications 2014, 50 (20), 2562-2564.

11. Zhang, D.; Wang, R.; Wen, M.; Weng, D.; Cui, X.; Sun, J.; Li, H.; Lu, Y., Synthesis of Ultralong Copper Nanowires for High-Performance Transparent Electrodes. Journal of the American Chemical Society 2012, 134 (35), 14283-14286.

12. Zhang, L.; Gong, X.; Bao, Y.; Zhao, Y.; Xi, M.; Jiang, C.; Fong, H., Electrospun Nanofibrous Membranes Surface-Decorated with Silver Nanoparticles as Flexible and Active/Sensitive Substrates for Surface-Enhanced Raman Scattering. Langmuir 2012, 28 (40), 14433-14440.

13. Ahn, Y.; Jeong, Y.; Lee, D.; Lee, Y., Copper Nanowire–Graphene Core–Shell Nanostructure for Highly Stable Transparent Conducting Electrodes. ACS nano 2015, 9 (3), 3125-3133.

14. Chen, Y. Y.; Kuo, C. C.; Chen, B. Y.; Chiu, P. C.; Tsai, P. C., Multifunctional polyacrylonitrile-Z n O/A g electrospun nanofiber membranes with various Z n O morphologies for photocatalytic, UV-shielding, and antibacterial applications. Journal of Polymer Science Part B: Polymer Physics 2015, 53 (4), 262-269.

15. Kuo, C. C.; Tung, Y. C.; Lin, C. H.; Chen, W. C., Novel Luminescent Electrospun Fibers Prepared From Conjugated Rod–Coil Block Copolymer of Poly [2, 7-(9, 9-dihexylfluorene)]-block-Poly (methyl methacrylate). Macromolecular Rapid Communications 2008, 29 (21), 1711-1715.

16. Kuo, C.-C.; Lin, C.-H.; Chen, W.-C., Morphology and Photophysical Properties of Light-Emitting Electrospun Nanofibers Prepared from Poly (fluorene) Serivative/PMMA Blends. Macromolecules 2007, 40 (19), 6959-6966.

17. Kuo, C. C.; Tung, Y. C.; Chen, W. C., Morphology and pH Sensing Characteristics of New Luminescent Electrospun Fibers Prepared from Poly (phenylquinoline)-block-Polystyrene/Polystyrene Blends. Macromolecular rapid communications 2010, 31 (1), 65-70.

18. Fu, W.; Dai, Y.; Meng, X.; Xu, W.; Zhou, J.; Liu, Z.; Lu, W.; Wang, S.; Huang, C.; Sun, Y. J. N., Electronic textiles based on aligned electrospun belt-like cellulose acetate nanofibers and graphene sheets: portable, scalable and eco-friendly strain sensor. 2018, 30 (4), 045602.

19. Lin, C. C.; Jiang, D.-H.; Kuo, C.-C.; Cho, C.-J.; Tsai, Y.-H.; Satoh, T.; Su, C., Water-Resistant Efficient Stretchable Perovskite-Embedded Fiber Membranes for Light-Emitting Diodes. ACS applied materials & interfaces 2018, 10 (3), 2210-2215.

20. Li, L.; Yang, G.; Li, J.; Ding, S.; Zhou, S., Cell Behaviors on Magnetic Electrospun Poly-D, L-lactide Nanofibers. Materials Science and Engineering: C 2014, 34, 252-261.

21. Pelipenko, J.; Kocbek, P.; Kristl, J., Critical Attributes of Nanofibers: Preparation, Drug Loading, and Tissue Regeneration. International journal of pharmaceutics 2015, 484 (1-2), 57-74.

22. Wu, H.; Hu, L.; Rowell, M. W.; Kong, D.; Cha, J. J.; McDonough, J. R.; Zhu, J.; Yang, Y.; McGehee, M. D.; Cui, Y., Electrospun Metal Nanofiber Webs as High-Performance Transparent Electrode. Nano letters 2010, 10 (10), 4242-4248.

23. An, S.; Kim, Y. I.; Jo, H. S.; Kim, M.-W.; Lee, M. W.; Yarin, A. L.; Yoon, S. S., Silver-Decorated and Palladium-Coated Copper-Electroplated Fibers Derived From Electrospun Polymer Nanofibers. Chemical Engineering Journal 2017, 327, 336-342.

24. Hsu, P.-C.; Wu, H.; Carney, T. J.; McDowell, M. T.; Yang, Y.; Garnett, E. C.; Li, M.; Hu, L.; Cui, Y., Passivation Coating on Electrospun Copper Nanofibers for Stable Transparent Electrodes. ACS nano 2012, 6 (6), 5150-5156.

Chapter 3

Light Down-Converter Based on the Blending of Polyfluorene Block Copolymers with Perovskite through Electrospinning

3.1 Introduction

Conjugated polymers have been attractive research areas in the last decades due to their potential properties, such as low-cost solution processability,[1-2] tunable bandgap,[3-5] easy structural and functional versatility through molecular design, and various self-assemble properties **(Section 1.2)**.[6-7] A satisfactory design and fabrication of these intrinsic active materials must sustain a large mechanical and deformation and maintain high semiconducting properties due to the rising technology within stretchable wearable devices for bioinspired robotics and healthcare.[8-11] Incorporating conjugated polymers with elastomeric materials is providing great opportunities to meet this new generation's requirements.[12-15] There are several methods to meet these new requirements, including polymer blending,[16-19] embedding,[20-21] and modification through synthesis.[22-23] These methods have widely been utilized to enhance the stretchability and flexibility of the conjugated polymers, as described in **Section 1.3**. Polyfluorene-based (PF-based) rod-coil BCPs have been extensively used for producing organic optoelectronic devices.[24-25] It is well-known that stretchability and the optical properties of materials could control by adjusting the rod/coil segment ratio. However, the optical and device performance of such designed materials decreased upon the coil ratio increased due to decreased conjugated phase domains.[26-27] The stretchable light-emitting materials show high device performance and work under high mechanical strain, which is critical to meet future demands.

In this chapter, the author reports how to make white emissive nanofiber (NF) membranes through electrospinning by combining the stretchable and blue light-emitter rod-coil BCPs (PFN-*b*-PBA) blending with perovskite ($CsPbBr_3$). The rod-coil BCPs (PFN-*b*-PBA) are synthesized through a click reaction with ethynyl-functionalized PFN and azido-terminated PBA homopolymers following the reported paper **(Scheme 3.1)**.[28] To easily apply the BCPs to the electrospinning, the author firstly increased the viscosity of the BCPs. To increase the viscosity, the author synthesizes the BCPs with high molecular weight by Suzuki–Miyaura catalyst transfer polymerization (SCTP) of PFN and atom transfer radical polymerization (ATRP) of PBA, respectively. The NF membranes prepared by electrospinning PFN-*b*-PBA blending with perovskite ($CsPbBr_3$) exhibit not only high flexible but also luminance. Furthermore, the white-light-emitting fibers are prepared by electrospinning in which the colors can be tuned by varying the perovskite/PFN ratio. This work represents an imperative stride in the field of conjugated BCPs with perovskite electronics through new opportunities for devices that demonstrate high performance white-light-emitting.

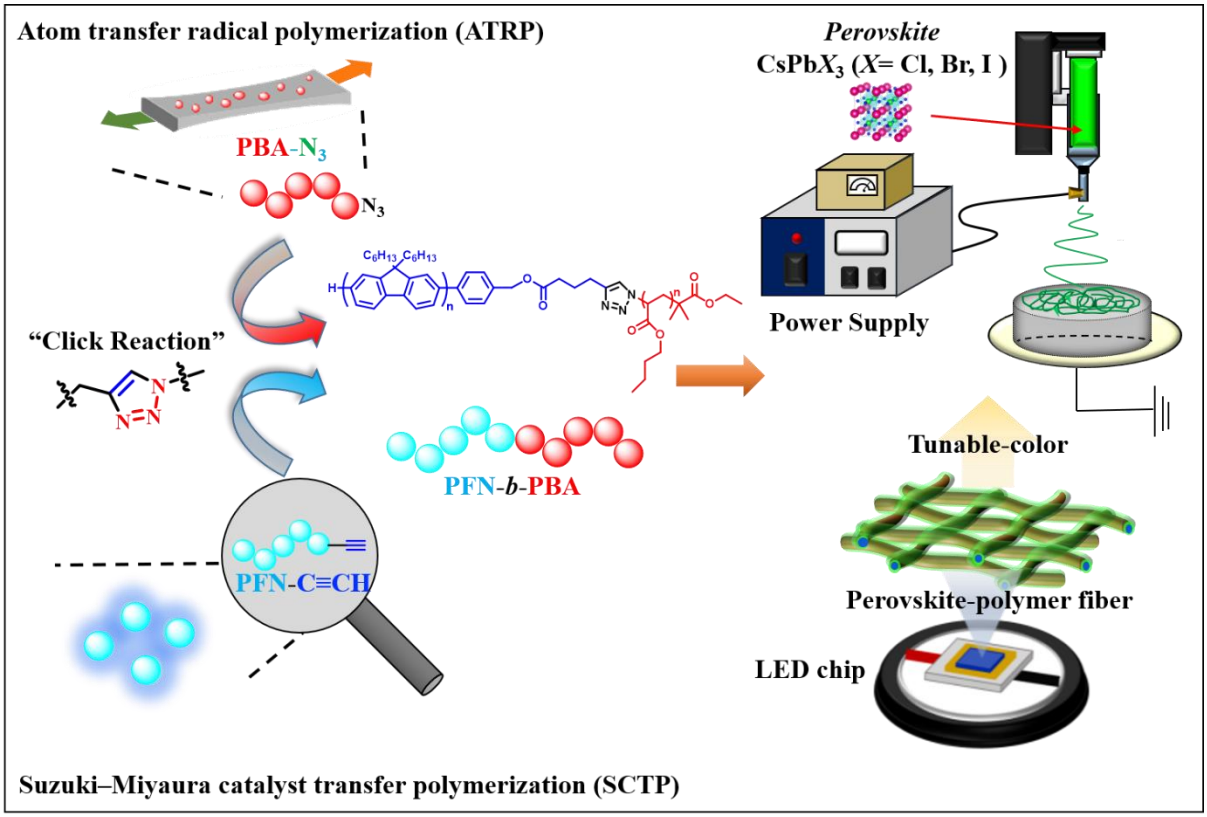

Scheme 3.1. A novel strategy for preparing light down-converter blending polyfluorene (PF) block copolymers (BCPs) with perovskite through electrospinning.

3.2 Experimental Section

3.2.1 Material

2-(7-Bromo-9, 9-dihexyl-9H-fluorene-2-yl) 4, 4, 5, 5-tetramethyl-1, 2, 3-dioxaborolane is prepared in accordance to the reported literature studies.[29-31] Tris-(dibenzylideneacetone)palladium ($Pd_2(dba)_3$, >97%), ethyl 2-bromo-2-methylpropanoate (≥98%), copper(I) bromide (CuBr, >98%), sodium azide (NaN_3, >99%), tetrahydrofuran (THF, anhydrous, ≥99%), methanol (MeOH, ≥99%), dichloromethane (CH_2Cl_2, anhydrous, ≥99%), toluene (anhydrous, ≥99%), chloroform ($CHCl_3$, anhydrous, ≥99%), *N*, *N*-dimethylformamide (DMF, ≥99%), oleyamine (primary amine, >98%), oleic acid (90%), cesium carbonate (99.995%), 1-octadecene (90%), and lead (ll) bromide are purchased from Sigma-Aldrich, Saint Louis, USA. Tri (*t*-butyl)phosphine (*t*-Bu_3P, >96%) and tripotassium phosphate (K_3PO_4, >95%) are purchased from Wako Pure Chemical, Osaka, Japan. 4-Iodobenzyl alcohol (>99.0%), 5-hexynoic acid (>95%), 18-crown-6 (>98%), *n*-butyl acrylate (BA, >99%), 1-ethyl-3-(3-dimethylaminopropyl) carbodiimide (EDC, >98%), 4-dimethylaminopyridine (DMAP, >99%), and *N*, *N*, *N′*, *N″*, *N″*-pentamethyldiethylenetriamine (PMDETA, >99%) are purchased from Tokyo Chemical, Tokyo, Japan.

3.2.2 Characterization

^1H nuclear magnetic resonance (NMR) spectra are measured with a JEOL JNM-ECS400

(JEOL Ltd., Tokyo, Japan) at room temperature at 400 MHz in chloroform-d_1, and chemically shifts are referenced to the internal stand. Molecular weights and dispersities of the polymers are measured by size exclusion chromatography (SEC) employing a THF where the eluent is at a flow rate of 1.0 mL min^{-1} at 40 °C. It is measured by employing a JASCO (JASCO Co., Tokyo, Japan) high-performance liquid chromatography system (PU-980 Intelligent HPLC pump, CO-2065 Plus Intelligent Column Oven, RI-2031 Plus Intelligent RI Detector, and DG-2080-53 Degasser) equipped with a Shodex KF-G guard column (4.6 mm×10 mm; particle size, 8 μm) and two Shodex KF-804L columns (linear; particle size, 7 μm; 8.0 mm × 300 mm; exclusion limit, 4 × 104) (Showa Denko K. K., Tokyo, Japan). The Ultraviolet-visible (UV-visible) spectra are measured by Jasco V-370 spectrophotometer (JASCO Co., Tokyo, Japan). The photoluminescence (PL) spectra are measured by a Fluorolog-3 spectrofluorometer (Horiba Jobin Yvon, Paris, France), and the polymer films are excited at wavelengths of 365 nm. The differential scanning calorimetry (DSC) is used and measured to investigate thermal properties under a nitrogen atmosphere by Hitachi DSC 7000X (Hitachi High-Tech Science Co., Ltd., Tokyo, Japan) with a heating/cooling rate of 10 °C min^{-1} from −100 °C to 250 °C under a nitrogen flow. Thermogravimetric analysis (TGA) is performed through a Bruker AXS TG-DTA2010SAT (Bruker AXS, Billerica, USA) with a heating rate of 10 °C min^{-1} from 100 °C to 800 °C under a nitrogen flow. The Fourier transform infrared spectroscopy (FTIR) analysis is carried out by using a PerkinElmer Frontier MIR spectrometer equipped with a

single reflection, diamond, universal, attenuated total reflection (ATR) accessory. The characterization of the X-ray powder diffraction (XRD) patterns is recorded using Cu Kα radiation (λ = 1.5418 Å) on a D2 Bruker diffractometer operating at 40 kV and 20 mA. The scanning electron microscopic (SEM) (Hitachi TM-3000, Tokyo, Japan) images are obtained through a cold-field emission scanning electron microscope (HR-SEM) (Hitachi S-4800, Tokyo, Japan) equipped with energy-dispersive. Ultraviolet-visible (UV-visible) spectra are measured by a spectrophotometer (Jasco V-730, Sendai, Japan). The photoluminescence (PL) spectra are measured by a fluorolog-3 spectrofluorometer (Horiba Jobin Yvon, Paris, French), and the NF mats are excited at wavelengths of 380 nm. The fluorescent images of $CsPbBr_3$@polymer fiber film are measured by a confocal spectral microscope imaging system (Leica TCS SP5, Wetzlar, Germany). The water-resistant properties of the $CsPbBr_3$@polymer fiber film are observed through a contact angle measurement with Phoenix 300 Touch (GAT Scientific, Suwon, Korea). The international commission on illumination (CIE) coordinated and correlated with the color temperature (CCT) of the white light-emitting diode (WLED) spectra are measured by Spectroradiometer (PR670, Taipei, Taiwan) under ambient air conditions at 25 °C. The calibration method is the standard sunset light, which was correlated to color temperature of 2856 K, this was performed to confirm the instrument's correctness. The time-resolved photoluminescence (TR-PL) spectra are coupled to a spectrometer (Horiba iHR320, Kyoto, Japan) with a Hamamatsu C10910 streak camera and an M10913 slow single

sweep unit. Temperature-dependent photoluminescence is measured with a pulsed diode-laser (PicoQuant LDH-D-C-375, Berlin, Germany) at a repetition rate of 1 MHz.

3.2.3. Synthesis of the ethynyl end-functionalized polyfluorene

In an argon-filled glove box, 4-iodobenzyl alcohol (288 μL, 0.14 mmol, 0.5 mole L^{-1} stock solution in THF), $Pd_2(dba)_3 \cdot CHCl_3$ (44.66 mg, 0.04 mmol), *t*-Bu_3P (633 μL, 0.32 mmol, as 0.5 mol L^{-1} stock solution in THF), and dry-THF (12 mL) are added to a vial and stirred for 30 minutes. A mixture of PFN monomer (7.15 ml, 3.45 mmol, 0.42M mol L^{-1} stock solution in THF), 18-crown-6 (9.44 mg, 35.75 mmol), and K_3PO_4 (22.77 mg, 107.25 mmol) are dissolved in a solvent of dry-THF (420 mL) and deionized water (54 mL), which is purged with argon and then cooled to -20 ℃. After 30 minutes of stirring, the Pd-initiator solution is introduced to the monomer solution by a cannula to start polymerization for 10 minutes. To terminate the polymerization, 12 mole L^{-1} HCl (10ml) is added to the reaction mixture for 30 minutes. After removing the solvent by evaporation, the residue is extracted by CH_2Cl_2 and brine. The organic layer is dried over $MgSO_4$ and purified by alumina. The residue is diluted by adding THF and is dropped into the cold toluene solution. The precipitate is collected by filtration and is dried under reduced pressure to get PFN_{24}-BnOH (953mg; yield: 85.10 %), a yellow powder. $M_{n,NMR}$ = 8,200 g mol^{-1} in chloroform-d_1; $M_{n,SEC}$ = 9,400; $Đ$ = 1.38. ^{1}H-NMR (400 MHz, $CDCl_3$): δ (ppm) 7.75-7.90 (m, Ar-H), 7.56-7.70 (m, Ar-H), 7.48 (d, Ar-H), 4.80 (d, -CH_2OH): 2.18 (br,

-$CH_2(CH_2)_4CH_3$), 0.62-1.32 (m, -$CH_2(CH_2)_4CH_3$).

The PFN_{24}-BnOH powder is dried overnight. In a three-neck flask, PFN_{24}-BnOH (900 mg, 0.11 mmol), EDC (105.20 mg, 0.55mmol), and DMAP (67.04 mg, 0.55 mmol) are dissolved in dry CH_2Cl_2 (100 mL). The reaction is deoxygenated by argon bubbling for 1 h, and then 5-hexynoic acid (59.86μL, 0.55mmol) is added to the solution. The reaction mixture is stirred for 24 h at room temperature, and the solvent is evaporated to dryness. The residue is diluted by adding THF and is dropped to the cold MeOH as a poor solvent to get PFN_{24}-C≡CH (857mg; yield: 95.2%), a yellow powder. $M_{n,\,NMR}$ = 8,300 g mol^{-1} in chloroform-d_1; $M_{n,SEC}$ = 9,500 $Đ$ = 1.43. ^{1}H-NMR (400 MHz, $CDCl_3$): δ (ppm) 7.74-7.88 (m, Ar-H), 7.58-7.76 (m, Ar-H), 7.48 (d, Ar-H), 5.24 (s, -CH_2-OC(＝O)CH_2-), 2.55 (t, -OC(＝O)CH_2-), 2.32 (m, CH_2C≡CH), 2.16 (br, -$CH_2(CH_2)_4CH_3$), 2.00 (t, -C≡CH), 1.92 (m,–CH_2CH_2C≡CH), 0.62-1.36 (m, -$CH_2(CH_2)_4CH_3$).

3.2.4. Synthesis of the azido-terminated poly (n-butyl acrylate)

The ω-Bromo end-functionalized poly (*n*-butyl acrylate) (PBA-Br) is prepared according to the reported paper.[28] The *n*-butyl acrylate (BA) (monomer) (18 mL, 0.126 mol, 126 eq) is purified by passing through a neutral Al_2O_3 column to remove out the inhibitor and is mixed with ethyl 2-bromoiso butyrate (initiator) (0.146 mL, 0.001 mol, 1 eq), CuBr (catalyst) (57.135 mg, 0.003mol, 3 eq), and anhydrous toluene (2 mL) in Schlenk flask under an argon atmosphere.

After 1 h, the PMDETA (0.209 mL, 0.001mol, 1 eq) is added to flask. The atom transfers radical polymerization (ATRP) is performed in the oil bath at 70 ℃ for 2 h followed by the terminal reaction through an air bubbling. The mixture is purified by Al_2O_3 column chromatography and is eluted with THF to remove out the catalyst. After that, the concentrated polymer solution is further purified by immersing in acetone with a Spectra/Pro dialysis membrane (molecular weight cutoff 1.0 kDa) for 48 h at room temperature. Finally, the polymer solution is evaporated to dryness, and a highly viscous and yellow PBA_{93}-Br liquid (8.91 g; yield: 55%) is obtained/prepared. Monomer conversion: 74%; $M_{n,\ NMR}$ = 11,800 g mol^{-1} in chloroform-d_1; $M_{n,SEC}$ = 12,600; $Đ$ = 1.10. ^{1}H NMR (400 MHz, $CDCl_3$): δ (ppm) 1.82-1.95 and 2.15-2.41 (br, polymer backbone); 3.83-4.10, 1.45-1.65, and 0.85-0.97 (br, butyl side chain).

The general procedure for azidation follows the previous paper:[28] The obtained PBA-Br (8.63g, 0.72 moles) and NaN_3 (233.76 mg, 3.60 moles) are dissolved in DMF (15 mL) and is stirred for 48 h at 40 ℃. The excess NaN_3 in the solution/mixture is removed by passing through a silica gel column by DMF to make a high viscous and a yellow PBA-N_3 liquid. PBA_{90}-Br conversion: 99%, PBA_{90}-N_3: $M_{n,\ NMR}$ = 11,700 g mol^{-1} in chloroform-d_1; $M_{n,SEC}$ = 12,500; $Đ$ = 1.10. ^{1}H NMR (400 MHz, $CDCl_3$): δ (ppm) 1.82-1.95 and 2.15-2.41 (br, polymer backbone); 3.89-4.08, 1.45-1.65, and 0.85-0.97 (br, butyl side chain).

3.2.5. Synthesis of the PFN-b-PBA block copolymer

The synthesis of BCP (PFN-*b*-PBA) (3) is performed through a click reaction of ethynyl-terminated PFN (1) with azido-terminated PBA (2). The PFN_{24}-C≡CH (200 mg, 25 μmol) is vacuumed dry overnight before the click reaction is taken place, and afterward, it is introduced in a flask with CuI (23.8 mg, 125 μmol). The PBA_{90}-N_3 (360 mg, 30 μmol), PMDETA (52.19 μL, 250 μmol), and anhydrous THF (7 mL) are placed in a 10 mL Schlenk flask. The reaction mixture of Schlenk flask is deoxygenated by argon bubbling for 1 h and then added to the flask under an argon atmosphere after a vacuum freeze-drying. The reaction flask is stirred for 42 h in an oil bath at 45 °C. The polymer solution is diluted by adding THF and is purified by passing through a basic Al_2O_3 column to remove the catalyst. The residue is further concentrated by rotary evaporation and is precipitated in the cold mixed solvent (MeOH/deionized water = 4/1 (*v*/*v*)) to remove the excessive PBA homopolymer. After precipitation, the final product of PFN_{24}-*b*-PBA_{90} (480 mg; yield: 85.7%) is obtained as a yellow sticky solid. $M_{n,\,NMR}$ = 19,100 g mol^{-1} in chloroform-d_1; $M_{n,SEC}$ = 21,400 $Đ$ = 1.43. ^{1}H NMR (400 MHz, $CDCl_3$): δ (ppm) 7.56-7.94 (m, Ar-H of PFN backbone), 5.24 (s, -CH_2-OC(= O)CH_2-), 2.16 (br, -$CH_2(CH_2)_4CH_3$ of PFN side chain), 0.62-0.87, 1.02-1.28 (m, -$CH_2(CH_2)_4CH_3$ of PFN side chain), 1.82-1.95, 2.15-2.41 (br, PBA backbone), 3.88-4.12, and 0.85-0.97 (br, butyl side chain of PBA).

3.2.6. Synthesis of the $CsPbX_3$ (X = Cl, Br, I)

The $CsPbX_3$ (X = Cl, Br, I) is prepared by a previously reported paper.[31] PbX_2 (0.188 mmol) and ODE (5 mL) are loaded into a 25 mL three-neck flask and are degassed in a vacuum at 120°C for 1 h. Subsequently, dried oleylamine (0.5 mL) and OA (0.5 mL) are injected into the solution at 120 °C in an N_2 atmosphere. The temperature is heated to 170 °C and csoleate solution (0.4 mL) is quickly injected into the mixture. The nanoparticles (NPs) are extracted from the crude solution by centrifuging at 3500 rpm for 10 min after the mixture is cooled. The precipitated particles are discarded, and the supernatant is redispersed in toluene to form the final solution.

3.2.7. Preparation of the electrospinning of $CsPbBr_3$ QDs/polymer NFs

The electrospinning NFs are prepared using a single-capillary spinneret. First, the $CsPbBr_3$ (100, 200, and 400 μl) is dissolved in CH_2Cl_2 (2 ml). Second, the PFN_{24}-*b*-PBA_{90} ($M_{n,\,SEC}$ = 21,400, 500 mg mL^{-1}) is added to the mixture and is stirred overnight. The polymer solution is fed into a metallic needle using syringe pumps with a feed rate of 0.8-1.0 mL h^{-1} and the voltage at 10.2 kV during the electrospinning. A piece of aluminum foil or quartz is placed 15 cm below the tip of the needle for 30-60 mins to collecting the NFs.

3.3 Results and Discussion

3.3.1 Synthesis and structure characterization of PFN-b-PBA BCPs

To prepare rod-coil BCPs by using copper-catalyzed click reaction, the homopolymer with appropriate functional groups for both polymerizations are synthesized according to the reported literature.[28] Polyfluorene with a benzyl alcohol (PFN_{24}-BnOH) is synthesized by the SCTP and then modified to the alkynyl-functionalized PFN (PFN_{24}-C≡CH) via the esterification from 5-hexynoic acid. The ^{1}H NMR signals of the PFN_{24}-BnOH and PFN_{24}-C≡CH clearly show the shift in the benzyl proton (e, 4.80 ppm to 5.24 ppm) and show the appearance of the new peak after modification due to hexynoate moiety (f: 2.55, h: 2.32, i: 2.00, and g: 1.92 ppm). This is indicating that the PFN_{24}-C≡CH is efficiently and successfully synthesized **(Figure 3.1a,b)**. On the other hand, the azido-terminated PBA is obtained through ATRP by using 2-bromo-2methylpropanoate as an initiator, and subsequently, the functionalized group is converted to azido group by utilizing sodium azide. The ^{1}H NMR signals of azido-terminated PBA (PBA_{90}-N_3) backbone (a: 1.82-1.95 and b: 2.15-2.41 ppm) and butyl side chain (c: 3.89-4.08, d and e: 1.45-1.65, and f: 0.85-0.97 ppm) are depicted in **Figure 3.1c,d**. The structure of PBA is further confirmed by the FTIR spectrum **(Figure 3.2)**. The FTIR spectrum of PBA display the characteristic of the stretching band at 2100 cm^{-1}, which corresponds to the azido group. Finally, rod-coil BCP, poly[2, 7-(9, 9-dihexyl-fluorene)]-*block*-poly(*n*-butyl acrylate) (PFN_{24}-*b*-PBA_{90}) is synthesized by coupling ethynyl-functionalized

PFN with azido-terminated PBA. The synthetic pathway is illustrated in **Scheme 3.2**, and the molecular characteristics of the polymers are listed in **Table 3.1**. Similarly, the ^{1}H NMR signals of PFN$_{24}$-*b*-PBA$_{90}$ exhibit the same characteristic protons of long alkyl chain from both PFN and PBA segment, and the peak at 2100 cm^{-1} from FTIR spectrum completely disappear due to the disappeared of the azido group **(Figure 3.3)**. Moreover, the SEC trace of the studied polymer display a unimodal peak with the M_w/M_n value of 1.43, which shows a shifted toward a higher molecular weight region as compared to the homopolymer (PFN and PBA) due to the successfully coupling reaction **(Figure 3.4)**.

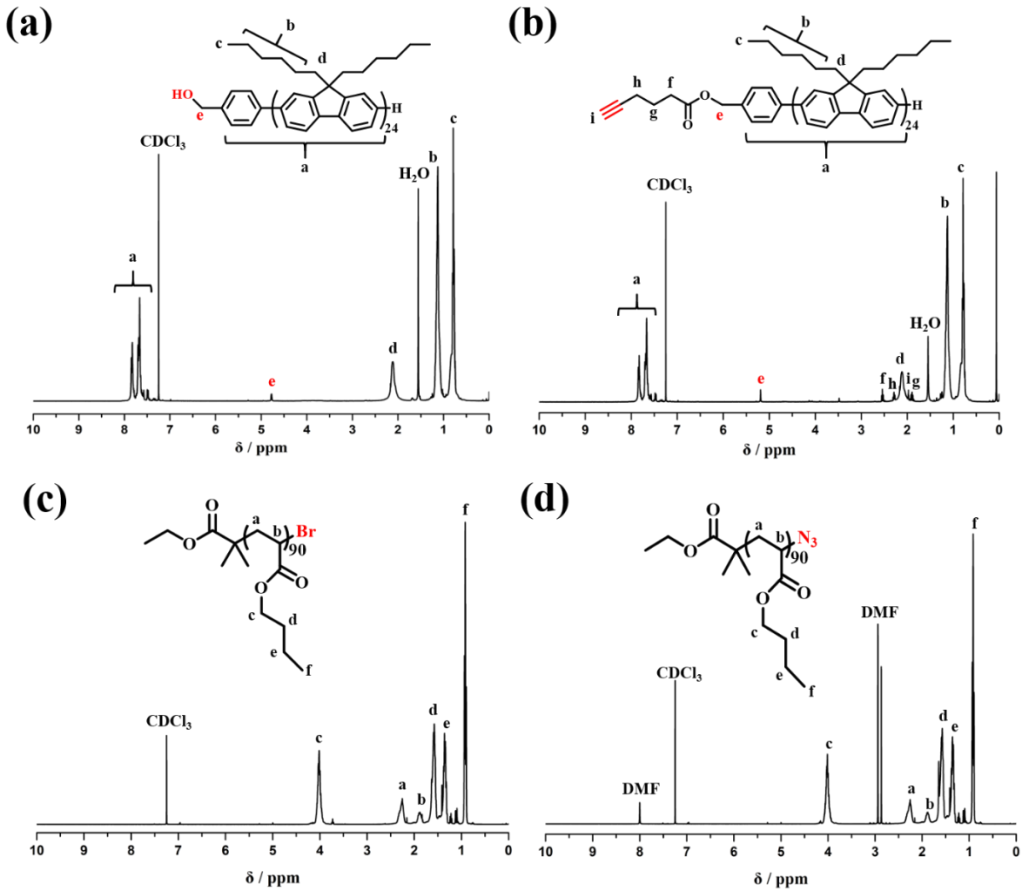

Figure 3.1. ^{1}H-NMR spectra of the (a) PFN$_{24}$-BnOH, (b) PFN$_{24}$-C≡CH, (c) PBA$_{90}$-Br$_3$ (d) PBA$_{90}$-N$_3$ in chloroform-d_1 ($CDCl_3$).

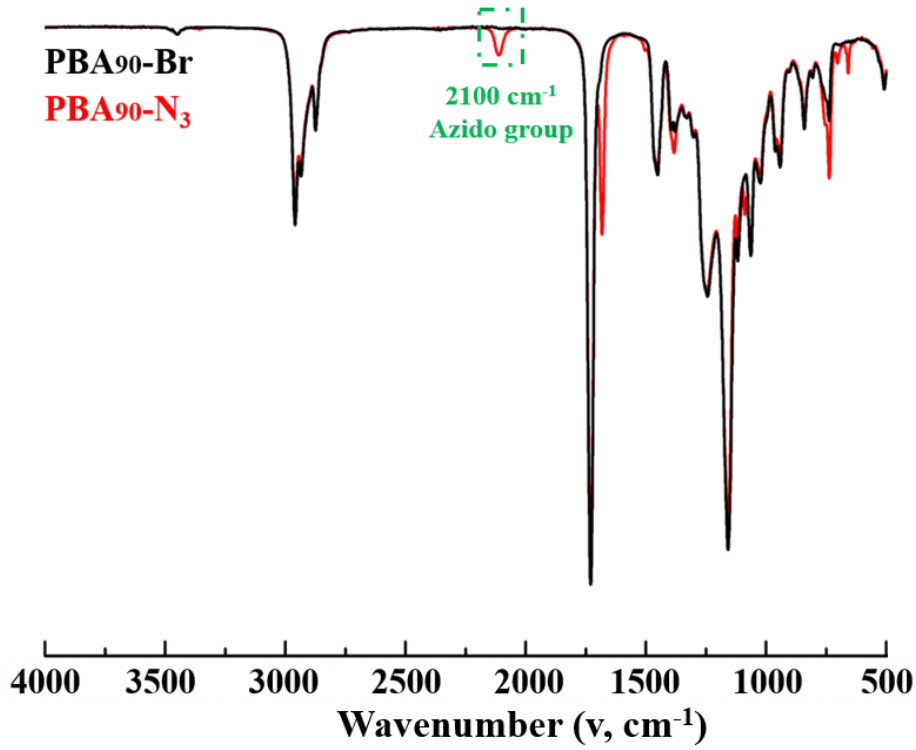

Figure 3.2. FTIR spectra of the PBA_{90}-Br and PBA_{90}-N_3.

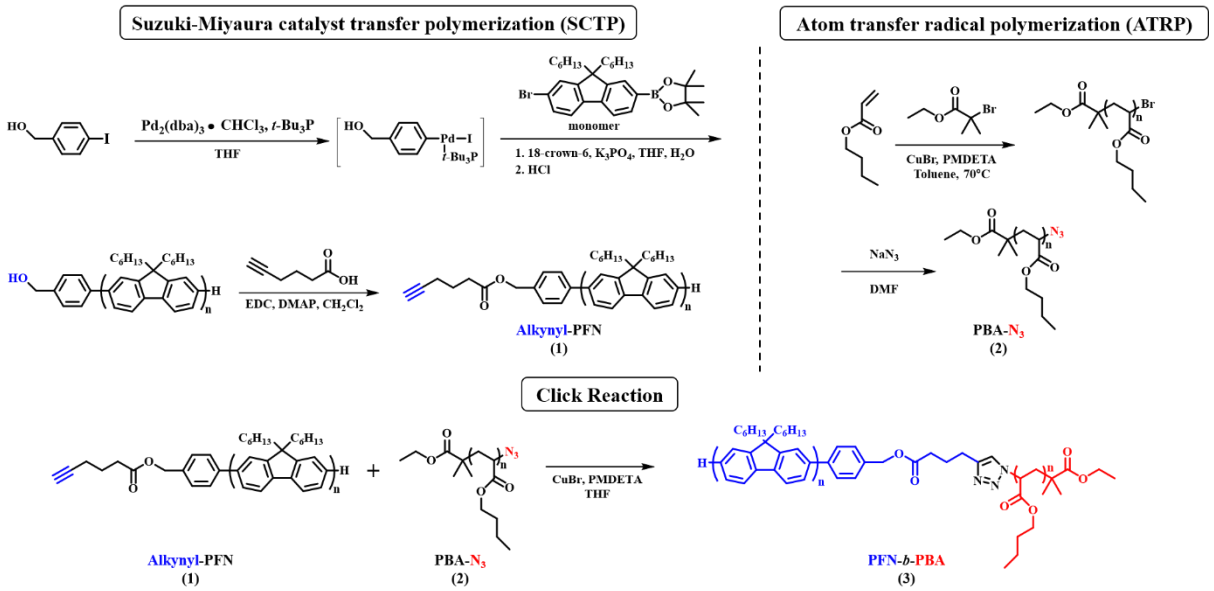

Scheme 3.2. The synthesis of PFN-*b*-PBA rod-coil block copolymer (BCP).

Table 3.1. Molecular characteristics of the PFN_{24}, PBA_{90}-N_3, and PFN_{24}-*b*-PBA_{90} copolymers.

Sample	PBA [a] (wt%)	$M_{n,NMR}$ [a] (g mol^{-1})	$M_{n,SEC}$ [b] (g mol^{-1})	$Đ$ [b]
PFN_{24}-C≡CH	0	8,200	9,400	1.38
PBA_{90}-N_3	100	11,700	12,500	1.10
PFN_{24}-*b*-PBA_{90}	72	19,100	21,400	1.43

[a]Calculated from ^{1}H NMR spectra of the polymers in chloroform-d_1 ($CDCl_3$). [b]Determined by SEC in tetrahydrofuran (THF) using a polystyrene (PS) standard.

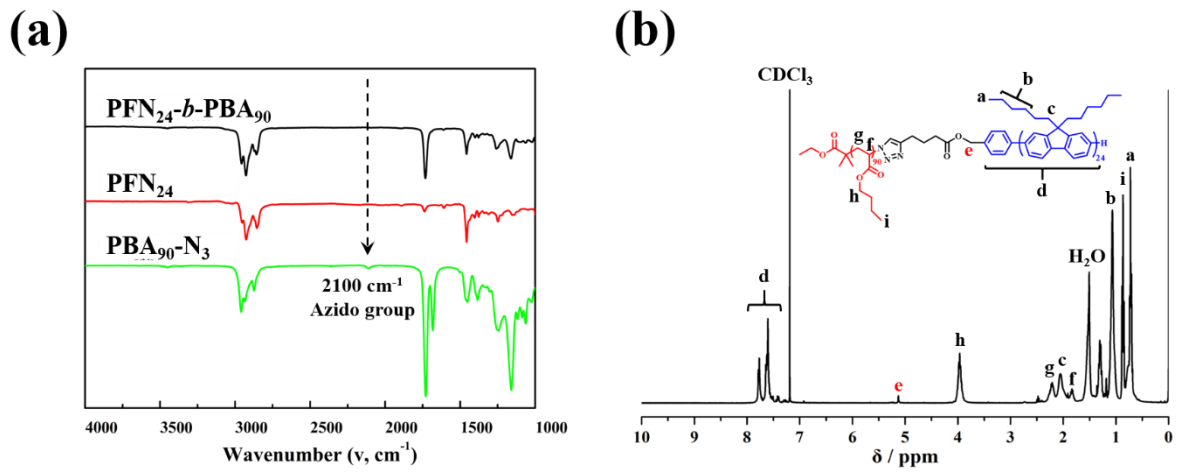

Figure 3.3. (a) FTIR spectra of the PFN_{24}, PBA_{90}-N_3, and PFN_{24}-*b*-PBA_{90} polymers. (b) ^{1}H-NMR spectrum of the PFN_{24}-*b*-PBA_{90} in chloroform-d_1 ($CDCl_3$) and

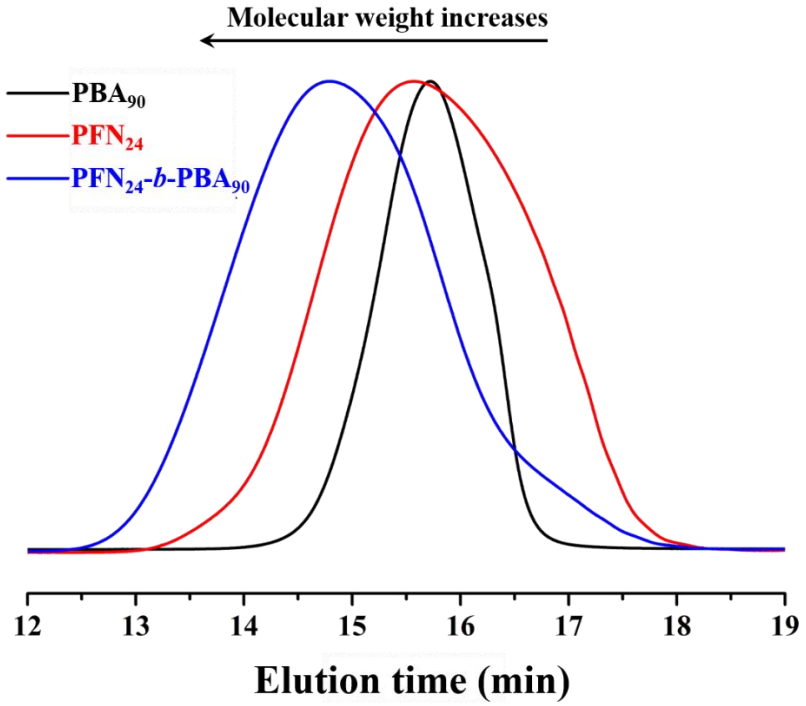

Figure 3.4. SEC profiles of the PFN_{24}, PBA_{90}, and PFN_{24}-*b*-PBA_{90} copolymers in tetrahydrofuran (THF) eluent.

3.3.2 The physical and optical properties of the PFN-b-PBA thin films

Afterward, the author is investigating the thermal behavior of BCPs by using TGA and DSC. This is summarized in **Table 3.2**. The results are indicating that the thermal degradation temperature (T_d, 5% weight loss) of the PFN_{24}-*b*-PBA_{90} (350 ℃) is between the PFN_{24}-C≡CH (401 ℃) and PBA_{90}-N_3 (340 ℃) homopolymers showing favorable thermal stability **(Figure 3.5)**. Also, the PFN_{24}-*b*-PBA_{90} exhibits two glass transition temperatures (T_g) from individual homopolymers, such as 78 ℃ (PFN_{24}) and -54℃ (PBA_{90}). It is widely acknowledged that the two individual phase transitions from PFN and PBA are due to an

incompatibility between the rod PFN and the coil PBA phase and tendency to separate these into different domains causing the existence of the two different T_g.[28]

Table 3.2. Physical properties of the PFN_{24}-C≡CH, PBA_{90}-N_3, PFN_{24}-*b*-PBA_{90}, and $CsPbBr_3$@PFN_{24}-*b*-PBA_{90} (1g BCPs and 400µl perovskite dissolve in 2 mL CH_2Cl_2).

Sample	T_d (°C)	T_g (°C)	As-cast film		Nanofiber membrane
			λ^{abs}_{max} (nm)	λ^{PL}_{max} (nm)	λ^{PL}_{max} (nm)
PFN_{24}-C≡CH	401	78	384	451, 481	--
PBA_{90}	340	-54	--	--	--
PFN_{24}-*b*-PBA_{90}	350	-78, 110	386	445,466	446
$CsPbBr_3$ @ PFN_{24}-*b*-PBA_{90}	--	--	382	445,471,510	446, 518

[a]Degradation temperature at the heating/cooling rate of 10°C min^{-1} in thermogravimetric analysis (TGA) in a nitrogen atmosphere. [b]Midpoint temperature of glass transition at a heating rate of 10°C min^{-1} in differential scanning calorimetry (DSC) in a nitrogen atmosphere. [c]Melting temperature. [d]Crystallization temperature at a cooling rate of 10°C min^{-1} in differential scanning calorimetry (DSC) in a nitrogen atmosphere.

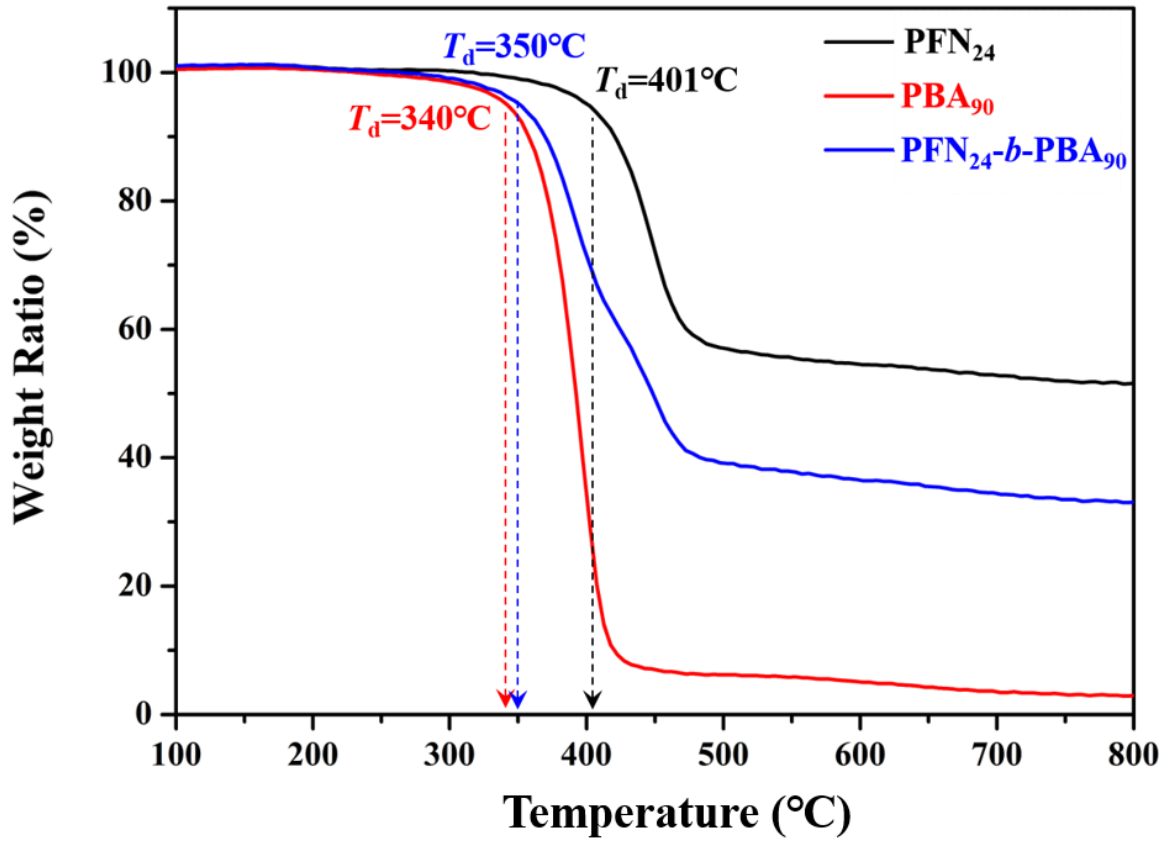

Figure 3.5. TGA curves of the PFN_{24}-C≡CH, PBA_{90}-N_3, and PFN_{24}-*b*-PBA_{90} copolymers.

The SEM images of $CsPbBr_3$ QDs@PFN_{24}-*b*-PBA_{90} composite fibers (1g BCPs and 400µl perovskite dissolve in 2 mL CH_2Cl_2) prepared by electrospinning are presented in **Figure 3.6a.** As seen in the figure, the fabricated fibers are uniformed and showed an average diameter of 800-1000 nm. Their surface morphology is smooth indicating that no perovskite crystals are appearing on the fiber surface. The XRD data of the $CsPbBr_3$@PFN_{24}-*b*-PBA_{90} fiber (1g/400µl) compared to the $CsPbBr_3$@PFN_{24}-*b*-PBA_{90} (1g/400µl) and the $CsPbBr_3$ QDs films are shown in **Figure 3.6b**. Interestingly, both $CsPbBr_3$@PFN_{24}-*b*-PBA_{90} film and $CsPbBr_3$@PFN_{24}-*b*-PBA_{90} fiber do not show any peak of perovskite. The author hypothesizes that this is inside of

the fiber. Therefore, the author is further conducting confocal imaging for $CsPbBr_3$ QDs@PFN_{24}-*b*-PBA_{90}, which are excited by UV-visible light at a wavelength of 380 nm, as shown in **Figure 3.6c**. The QDs and PFN in the sample are emitting their original light colors verified that the perovskite QDs are encapsulated inside the polymer fiber, and the fluorescent properties are restained after electrospinning. **Figure 3.7** shows the UV-vis and PL spectra of the studied polymers, which are prepared by spin-coating and electrospinning. The λ^{abs}_{max} values of PFN_{24} and PFN_{24}-*b*-PBA_{90} are observed at 384 and 386 nm, respectively, which are from the π-π conjugation of the PFN block. To the as-cast film of λ^{PL}_{max} values, the blue color shifted from PFN_{24}-*b*-PBA_{90} can be observed that owing to the phase separation from PFN and PBA block phenomenon. The as-cast film of $CsPbBr_3$ @PFN_{24}-*b*-PBA_{90} can also be observed at the π-π conjugation peak at 382 nm, and the λ^{PL}_{max} values show peaks at 445, 471, and 510 nm, respectively. A peak located at 510 nm is assigned from the $CsPbBr_3$ QDs and the distinct peaks of 445 and 471 nm are assigned to the different crystal phases of PFN blocks **(Table 3.2)**.

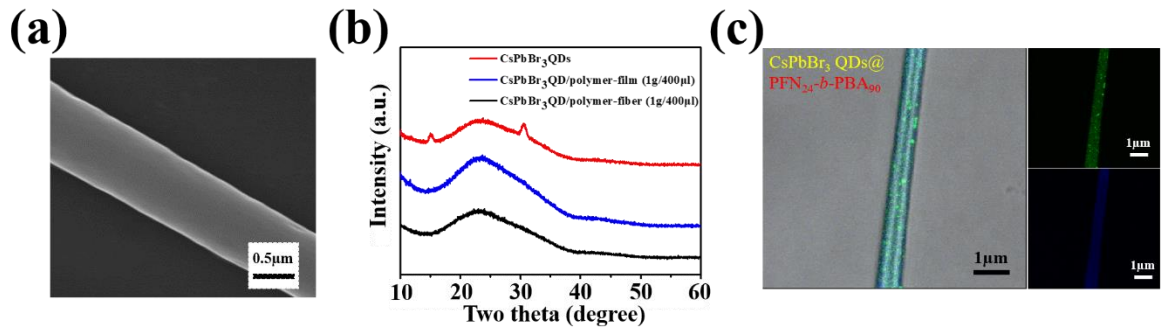

Figure 3.6. (a) SEM images of the $CsPbBr_3$@PFN_{24}-*b*-PBA_{90} fibers (1g/400μl). (b) XRD patterns of the $CsPbBr_3$@PFN_{24}-*b*-PBA_{90} fiber mats, $CsPbBr_3$@PFN_{24}-*b*-PBA_{90}, and $CsPbBr_3$ QDs film. (c) Confocal image of the $CsPbBr_3$ QDs@PFN_{24}-*b*-PBA_{90} fibers.

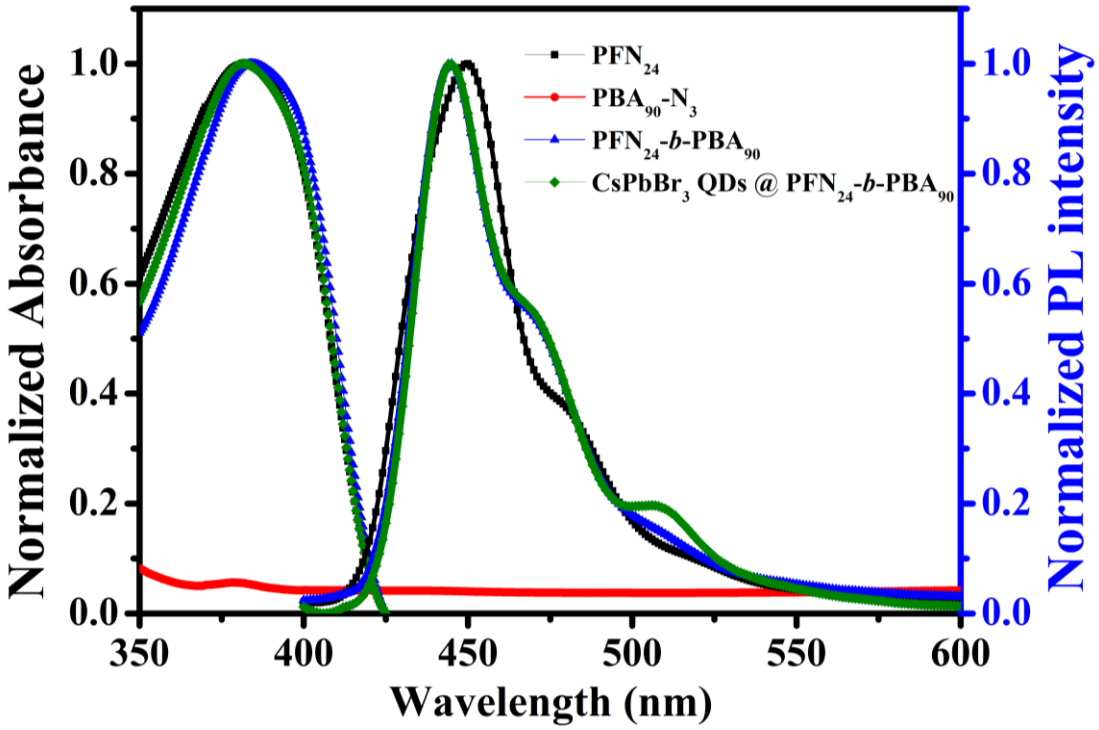

Figure 3.7. UV-vis absorption and PL emission spectrum of the PFN_{24}-C≡CH, PBA_{90}-N_3, PFN_{24}-*b*-PBA_{90}, and $CsPbBr_3$ QDs@PFN_{24}-*b*-PBA_{90} films (1g/400μl).

3.3.3 Morphologies and stretchable performance of the PFN-b-PBA thin films

The PFN_{24} homopolymer, PFN_{24}-*b*-PBA_{90} films, and $CsPbBr_3$ QDs@PFN_{24}-*b*-PBA_{90} fibers are measured directly by OM under different strains for the deformation, as shown in **Figure 3.8**. First, the studied samples are prepared onto the polyurethane (PU) substrate by spin-coating and electrospinning. The PFN_{24} homopolymer's surface starts to crack while the strain is gradually increasing. By incorporating to the PBA soft block, the stretchability of PFN_{24}-*b*-PBA_{90} film is enhanced, it is starting to crack once the strain reached 150%. By contrast, the $CsPbBr_3$ QDs@PFN_{24}-*b*-PBA_{90} fibers are no crack appearing even under the strain 200%. It affirms that the soft block modification and nano-scale change by electrospinning can effectively enhance the stretchability of the material.[32-33]

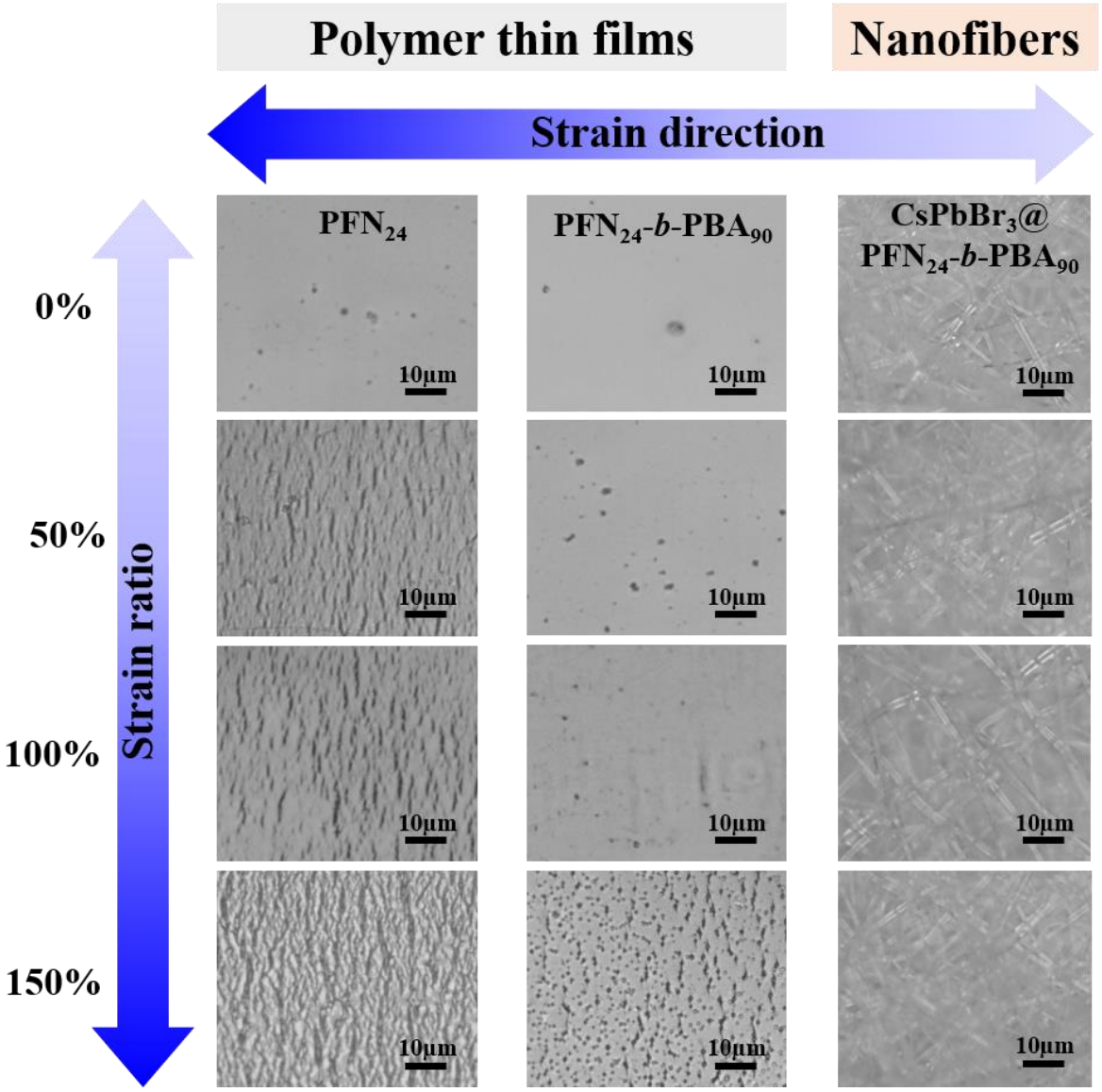

Figure 3.8. The crack-onset test for the PFN_{24}, PFN_{24}-*b*-PBA_{90} films, and $CsPbBr_3$ @PFN_{24}-*b*-PBA_{90} composite fibers (1g/400μl).

3.3.4 The color-tunable properties of light-emitting diodes

The color-tunable light down-converter LEDs are successfully fabricated by using a single-layer of $CsPbBr_3$@PFN_{24}-*b*-PBA_{90} composite fibers on a commercial UV chip (λ_{max} = 380 nm) and the Commission Internationale de l'eclairage (CIE) is illustrated in **Figure 3.9**. Besides,

the color from LED can be controlled by adjusting the varying of the QD/polymer ratio, 1:100, 1:200, and 1:400 (1g/400µl) and different voltages. The LEDs with different correlated color temperatures (CCTs), which corresponding to the LED emission images are presented in the insets of **Figure 3.9**. It clearly shows that the emissive intensity of perovskite is becoming weaker when the ratio is decreasing. The higher intensity at 550 nm on green color emission is observed with an increasing perovskite QD blending ratio. It is because of the obvious energy transfer (physical process) from commercial UV LED chip (donor) and PF block (donor) to perovskite QD (acceptor). In this way, the CCTs and the color can be tuned from green to blue. It is a novel and easy way to control the color by blending perovskite in the fluorescent polymer.

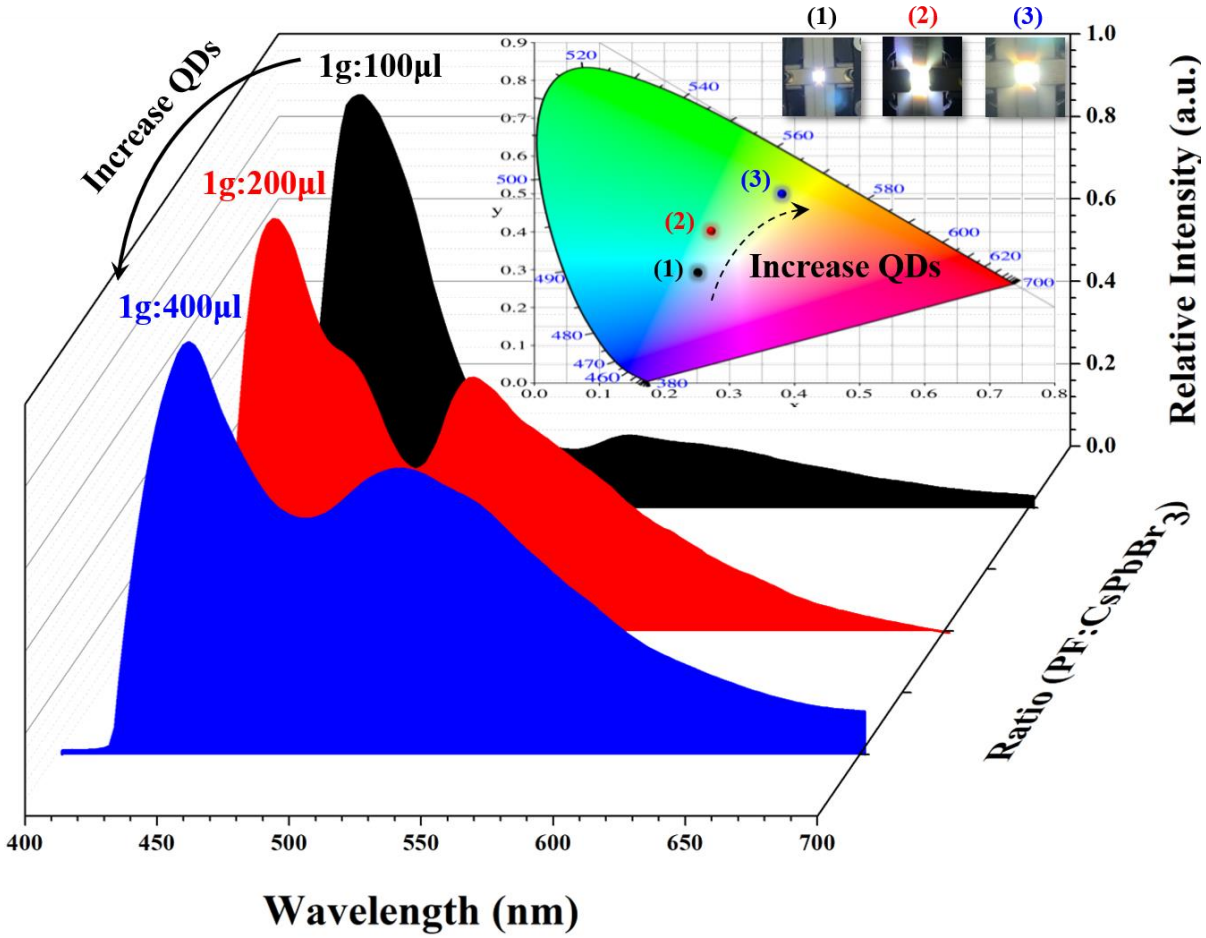

Figure 3.9. Emission spectra of different color LEDs with CIE color coordinates by using $CsPbBr_3$@ PFN_{24}-*b*-PBA_{90} composite fibers under UV chip (380 nm) excitation and an applied voltage 3V. (Inset images show the LEDs applied by 1:100, 1:200, and 1:400 (g/µl) ratio of QD/polymer composite fibers)

3.4 Conclusion

In this chapter, the author successfully demonstrates the novel strategy to fabricate the stretchable and color-tunable LEDs by only a single-layer. By incorporation of a PBA coil block, enabling a BCP to construct high stretchability. This resulting in enlarging the applied scopes, such as e-skin, wearable devices, and stretchable LEDs. Furthermore, this method is different from multilayer stack and perovskite's halogen substitute methods, as the LED's color can be tuned by varying the QD/polymer ratios through the double fluorescence combination by only a single-layer fiber mat. The present study suggests that rod-coil BCPs combining with perovskite QDs have the potential to form high stretchability as well as fluorescence properties for versatile applications that require intrinsically outstanding optical properties.

Another interesting discovery in this chapter, the PF-based rod-coil BCPs exhibit higher PLQY than their respective homopolymers, which corresponding to previously reported papers **(Section 1.3)**.[28, 34-35] It is well-known that the insulating property of coil-segment significantly lowers the interchain charge transport properties, which is unfavorable for achieving an efficient electroluminescent device. High PLQY implies that the rod-coil BCPs have a better potential for LED, but there are no reports on this in the current. To address this problem and accelerate facile fabricate wearable devices, the author will discuss in-depth in the next chapter.

3.5 References

1. Chikamatsu, M.; Nagamatsu, S.; Yoshida, Y.; Saito, K.; Yase, K.; Kikuchi, K., Solution-processed n-type organic thin-film transistors with high field-effect mobility. Appli. Phys. Lett. 2005, 87 (20), 203504.
2. Yu, X.; Rahmanudin, A.; Jeanbourquin, X. A.; Tsokkou, D.; Guijarro, N. s.; Banerji, N.; Sivula, K., Hybrid heterojunctions of solution-processed semiconducting 2D transition metal dichalcogenides. ACS Energy Lett. 2017, 2 (2), 524-531.
3. Van De Wetering, K.; Brochon, C.; Ngov, C.; Hadziioannou, G., Design and Synthesis of a Low Band Gap Conjugated Macroinitiator: Toward Rod− Coil Donor− Acceptor Block Copolymers. Macromolecules 2006, 39 (13), 4289-4297.
4. Yi, Z.; Wang, S.; Liu, Y., Design of high-mobility diketopyrrolopyrrole-based π-conjugated copolymers for organic thin-film transistors. Adv. Mater. 2015, 27 (24), 3589-3606.
5. Zhang, Y.-H.; Zhou, K.-G.; Xie, K.-F.; Zeng, J.; Zhang, H.-L.; Peng, Y., Tuning the electronic structure and transport properties of graphene by noncovalent functionalization: effects of organic donor, acceptor and metal atoms. Nanotechnology 2010, 21 (6), 065201.
6. An, B.-K.; Gierschner, J.; Park, S. Y., π-Conjugated cyanostilbene derivatives: a unique self-assembly motif for molecular nanostructures with enhanced emission and transport. Acc. Chem. Res. 2011, 45 (4), 544-554.
7. Luo, C.; Kyaw, A. K. K.; Perez, L. A.; Patel, S.; Wang, M.; Grimm, B.; Bazan, G. C.; Kramer, E. J.; Heeger, A. J., General strategy for self-assembly of highly oriented nanocrystalline semiconducting polymers with high mobility. Nano Lett. 2014, 14 (5), 2764-2771.
8. Choi, S.; Lee, H.; Ghaffari, R.; Hyeon, T.; Kim, D. H., Recent advances in flexible and stretchable bio-electronic devices integrated with nanomaterials. Adv. Mater. 2016, 28 (22), 4203-4218.
9. Kim, D.-H.; Lu, N.; Ma, R.; Kim, Y.-S.; Kim, R.-H.; Wang, S.; Wu, J.; Won, S. M.; Tao, H.; Islam, A., Epidermal electronics. Science 2011, 333 (6044), 838-843.
10. Rogers, J. A.; Someya, T.; Huang, Y., Materials and mechanics for stretchable electronics. Science 2010, 327 (5973), 1603-1607.
11. Zhang, Y.; He, Z.; Jiang, S.; Gao, B.; Liu, Z.; Han, B.; Wang, H., Marine redox stratification during the early C ambrian (ca. 529-509 Ma) and its control on the development of organic-rich shales in Y angtze P latform. Geochemistry, Geophysics, Geosystems 2017, 18 (6), 2354-2369.
12. Choi, M. K.; Yang, J.; Kang, K.; Kim, D. C.; Choi, C.; Park, C.; Kim, S. J.; Chae, S. I.; Kim, T.-H.; Kim, J. H., Wearable red–green–blue quantum dot light-emitting diode array using high-resolution intaglio transfer printing. Nature Comm. 2015, 6, 7149.

13. Kim, T.-H.; Lee, C.-S.; Kim, S.; Hur, J.; Lee, S.; Shin, K. W.; Yoon, Y.-Z.; Choi, M. K.; Yang, J.; Kim, D.-H., Fully stretchable optoelectronic sensors based on colloidal quantum dots for sensing photoplethysmographic signals. ACS Nano 2017, 11 (6), 5992-6003.
14. Son, D.; Chae, S. I.; Kim, M.; Choi, M. K.; Yang, J.; Park, K.; Kale, V. S.; Koo, J. H.; Choi, C.; Lee, M., Colloidal synthesis of uniform-sized molybdenum disulfide nanosheets for wafer-scale flexible nonvolatile memory. Adv. Mater. 2016, 28 (42), 9326-9332.
15. Song, J. K.; Son, D.; Kim, J.; Yoo, Y. J.; Lee, G. J.; Wang, L.; Choi, M. K.; Yang, J.; Lee, M.; Do, K., Wearable force touch sensor array using a flexible and transparent electrode. Adv. Funct. Mater. 2017, 27 (6), 1605286.
16. Choi, D.; Kim, H.; Persson, N.; Chu, P.-H.; Chang, M.; Kang, J.-H.; Graham, S.; Reichmanis, E., Elastomer–polymer semiconductor blends for high-performance stretchable charge transport networks. Chem. Mater. 2016, 28 (4), 1196-1204.
17. Kuo, C.-C.; Lin, C.-H.; Chen, W.-C., Morphology and photophysical properties of light-emitting electrospun nanofibers prepared from poly (fluorene) derivative/PMMA blends. Macromolecules 2007, 40 (19), 6959-6966.
18. Lee, Y.; Zhou, H.; Lee, T.-W., One-dimensional conjugated polymer nanomaterials for flexible and stretchable electronics. J. Mater. Chem. C 2018, 6 (14), 3538-3550.
19. Scott, J. I.; Xue, X.; Wang, M.; Kline, R. J.; Hoffman, B. C.; Dougherty, D.; Zhou, C.; Bazan, G.; O'Connor, B. T., Significantly increasing the ductility of high performance polymer semiconductors through polymer blending. ACS Appli. Mater. Inter. 2016, 8 (22), 14037-14045.
20. Shin, M.; Oh, J. Y.; Byun, K. E.; Lee, Y. J.; Kim, B.; Baik, H. K.; Park, J. J.; Jeong, U., Polythiophene nanofibril bundles surface-embedded in elastomer: A route to a highly stretchable active channel layer. Adv. Mater. 2015, 27 (7), 1255-1261.
21. Song, E.; Kang, B.; Choi, H. H.; Sin, D. H.; Lee, H.; Lee, W. H.; Cho, K., Stretchable and transparent organic semiconducting thin film with conjugated polymer nanowires embedded in an elastomeric matrix. Adv. Electron. Mater. 2016, 2 (1), 1500250.
22. Peng, R.; Pang, B.; Hu, D.; Chen, M.; Zhang, G.; Wang, X.; Lu, H.; Cho, K.; Qiu, L., An ABA triblock copolymer strategy for intrinsically stretchable semiconductors. J. Mater. Chem. C 2015, 3 (15), 3599-3606.
23. Wu, H.-C.; Hung, C.-C.; Hong, C.-W.; Sun, H.-S.; Wang, J.-T.; Yamashita, G.; Higashihara, T.; Chen, W.-C., Isoindigo-based semiconducting polymers using carbosilane side chains for high performance stretchable field-effect transistors. Macromolecules 2016, 49 (22), 8540-8548.
24. Lu, S.; Liu, T.; Ke, L.; Ma, D.-G.; Chua, S.-J.; Huang, W., Polyfluorene-based light-emitting rod− coil block copolymers. J. Macromol. 2005, 38 (20), 8494-8502.
25. Saito, K.; Isono, T.; Sun, H.-S.; Kakuchi, T.; Chen, W.-C.; Satoh, T., Rod–coil type

miktoarm star copolymers consisting of polyfluorene and polylactide: precise synthesis and structure–morphology relationship. Polym. Chem. 2015, 6 (39), 6959-6972.

26. Wang, J.-T.; Saito, K.; Wu, H.-C.; Sun, H.-S.; Hung, C.-C.; Chen, Y.; Isono, T.; Kakuchi, T.; Satoh, T.; Chen, W.-C., High-performance stretchable resistive memories using donor–acceptor block copolymers with fluorene rods and pendent isoindigo coils. NPG Asia Mater. 2016, 8 (8), e298.
27. Wang, J.-T.; Takshima, S.; Wu, H.-C.; Shih, C.-C.; Isono, T.; Kakuchi, T.; Satoh, T.; Chen, W.-C., Stretchable conjugated rod–coil poly (3-hexylthiophene)-block-poly (butyl acrylate) Thin films for field effect transistor applications. Macromolecules 2017, 50 (4), 1442-1452.
28. Hsieh, H.-C.; Hung, C.-C.; Watanabe, K.; Chen, J.-Y.; Chiu, Y.-C.; Isono, T.; Chiang, Y.-C.; Reghu, R. R.; Satoh, T.; Chen, W.-C., Unraveling the stress effects on the optical properties of stretchable rod-coil polyfluorene-poly (n-butyl acrylate) block copolymer thin films. Polym. Chem. 2018, 9 (27), 3820-3831.
29. Bade, S. G. R.; Shan, X.; Hoang, P. T.; Li, J.; Geske, T.; Cai, L.; Pei, Q.; Wang, C.; Yu, Z., Stretchable Light-Emitting Diodes with Organometal-Halide-Perovskite–Polymer Composite Emitters. Adv. Mater. 2017, 29 (23), 1607053.
30. Chou, S.-Y.; Ma, R.; Li, Y.; Zhao, F.; Tong, K.; Yu, Z.; Pei, Q., Transparent Perovskite Light-Emitting Touch-Responsive Device. ACS Nano 2017, 11 (11), 11368-11375.
31. Lin, C. C.; Jiang, D.-H.; Kuo, C.-C.; Cho, C.-J.; Tsai, Y.-H.; Satoh, T.; Su, C., Water-resistant efficient stretchable perovskite-embedded fiber membranes for light-emitting diodes. ACS Appli. Mater. Inter. 2018, 10 (3), 2210-2215.
32. Wang, X.; Zhang, Y.; Zhang, X.; Huo, Z.; Li, X.; Que, M.; Peng, Z.; Wang, H.; Pan, C., A highly stretchable transparent self-powered triboelectric tactile sensor with metallized nanofibers for wearable electronics. Adv. Mater. 2018, 30 (12), 1706738.
33. Sehaqui, H.; Morimune, S.; Nishino, T.; Berglund, L. A., Stretchable and strong cellulose nanopaper structures based on polymer-coated nanofiber networks: An alternative to nonwoven porous membranes from electrospinning. Biomacromolecules 2012, 13 (11), 3661-3667.
34. Jao, C. C.; Chang, J. R.; Ya, C. Y.; Chen, W. C.; Cho, C. J.; Lin, J. H.; Chiu, Y. C.; Zhou, Y.; Kuo, C. C. J. P. I., Novel stretchable light-emitting diodes based on conjugated-rod block elastic-coil copolymers. 2020.
35. Au-Duong, A.-N.; Wu, C.-C.; Li, Y.-T.; Huang, Y.-S.; Cai, H.-Y.; Jo Hai, I.; Cheng, Y.-H.; Hu, C.-C.; Lai, J.-Y.; Kuo, C.-C. J. M., Synthetic Concept of Intrinsically Elastic Luminescent Polyfluorene-Based Copolymers via RAFT Polymerization. 2020, 53 (10), 4030-4037.

Chapter 4

Smart Synthesis of Polyfluorene-Based Block Copolymers Accelerates Design and Fabrication of Flexible Light-Emitting Diode Devices

4.1 Introduction

As described in **Section 1.3**, polyfluorene-based (PF-based) conjugated block copolymers (BCPs) have an impressive footprint on the continued development related to their various applications in microelectronics,[1-2] optoelectronics,[3-5] biotechnology,[6-7] and environmental technology[8] due to facile low-cost solution processability and various self-assemble nanostructures. With detailed molecular design, type, and size of the nanostructure, self-assembled BCPs are controlled by molecular weight ratio and volume fraction between blocks. The nanostructures of spherical,[9-10] cylindrical,[10-11] bicontinuous,[10,12] and lamellar[10,13] forming conjugated BCPs have attracted considerable attention because they boost the modification of the active-layer morphology for improving electronic device performance. The control over domain size of nanostructure to achieve efficient charge transport is known to enhance device performance due to the effective radiative recombination between the electron and hole.[14-15] Besides, coil blocks add flexibility to the overall BCPs and enable the construction of wearable devices.[16-17] Unfortunately, the insulating property of coil-segment significantly lowers the interchain charge transport properties, which is unfavorable for achieving efficient electroluminescent device. Therefore, it is critical to find a balance between the two conflicting factors in the molecular design of conjugated BCPs.

The typical synthesis of PF derivatives is carried out by Suzuki-Miyaura polycondensation (SMP) in a classical step-growth fashion, but it is unfavorable for the preparation of BCPs. As

an alternative method, synthesis of heterodifunctional PF via controlled chain-growth Suzuki–Miyaura catalyst transfer polymerization (SCTP) is more suitable for block copolymerization, where the PF chain-ends are capped with chemically reactive end groups for further functionalization and copolymerization.[3-4,18] Another promising method is the utilization of ethynyl or azido groups for click reaction to produce BCPs.[7, 19] However, the laborious synthetic procedures and the complexity of purification of these methods are limiting mass production.[3,7,18-21] Despite the limitations, some studies demonstrate the successful application of conjugated BCPs produced by the aforementioned methods. Chen and Satoh *et al*. have synthesized rod-coil BCPs poly[2,7-(9,9dihexylfluorene)]-*block*-poly (*n*-butyl acrylate) (PFN-*b*-PBA) through a click reaction and demonstrated high fluorescence properties and deformability, which could have great potential for high-performance wearable electronic devices.[21] Additionally, Chiu *et al*. have designed intrinsically elastic PF-based copolymers via reversible addition-fragmentation chain transfer (RAFT) polymerization. The copolymers had stable mechanical performance and stable photoluminescence quantum yield (PLQY) at 300% strain over 100 cycles.[22] It is noteworthy that both examples have had rod-coil conjugated BCPs exhibit higher PLQY than their respective homopolymers, as mentioned in **Section 1.3**.[21-22] This implies conjugated BCPs are potential candidates for light-emitting diode (LED) applications, but there are no reports on this in the current.

To address the limitations in synthesis processes and produce conjugated BCPs with high

PLQY, in this chapter, the author presents a smart one-pot synthesis based on the SCTP and ring-opening polymerization (ROP). High PLQY and exciton binding energy (EBE) are induced by coil-segment having low-dielectric constants. The PF blocks self-assemble into a layer structure surrounded by the coil-segment driven by π-π stacks increasing the attractive force between electron and hole, because of weak screen effect. In addition, the flexible touch-responsive LED devices with PFN_{18}-*b*-PDL_{13} as the emissive layer exhibit deformability and greater external quantum efficiency (EQE, 6 times higher) than devices with PF homopolymer **(Scheme 4.1)**. This is the first study to demonstrate greater LED performance for the conjugated BCP system over its respective conjugated homopolymer.

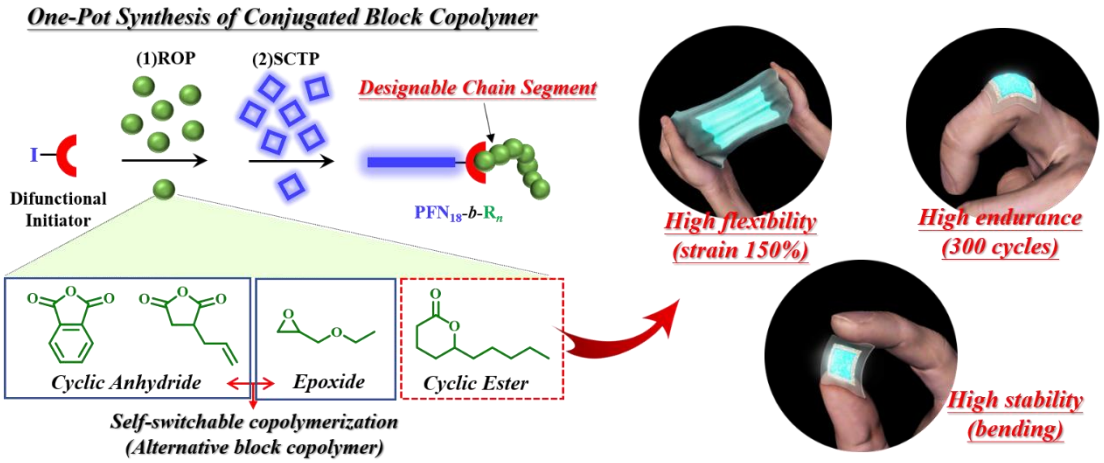

Scheme 4.1. Smart one-opt synthesis for facile fabrication of flexible touch-responsive LEDs.

4.2 Experimental Section

4.2.1 Material

Potassium 2-(7-bromo-9,9-di-*n*-hexyl-9H-fluorene-2-yl) triolborate is prepared according to the previous report.[23] Tris-(dibenzylideneacetone) palladium ($Pd_2(dba)_3$, >97%), tetrahydrofuran (THF, anhydrous, ≥99%), methanol (MeOH, ≥99%), dichloromethane (CH_2Cl_2, anhydrous, ≥99%), toluene (anhydrous, ≥99%), chloroform ($CHCl_3$, anhydrous, ≥99%), *δ*-decanolactone (*δ*-DL), phthalic anhydride (PA), ethyl glycidyl ether (EGE), *tert*-butylimino-tri(pyrrolidino)phosphorene (*t*-BuP_1), allyl succinic anhydride (AA), dec-5-ene (TBD, >98.0%), poly(9,9-di-*n*-octyl-2,7-fluorene) (PFO) (M_n ~ 10,000, $Đ$ ~ 2), and poly(ethylene glycol) (PEO), poly(3,4-ethylenedioxythiophene)-poly(styrenesulfonate) (PEDOT: PSS; high conductivity grade 1.1 wt% in H_2O) are purchased from Sigma-Aldrich, Saint Louis, USA. Tri(*tert*-butyl)phosphine (*t*-Bu_3P, >96%) is purchased from Wako Pure Chemical Industries Ltd, Osaka, Japan. 4-Iodobenzyl alcohol (>99.0%) is purchased from Tokyo Chemical Industry Co., Ltd., Tokyo, Japan. Polyurethane (PU) is purchased from RainEmpire Taipei Co., Ltd., Taipei, Taiwan. Silver nanowires (average diameter = 55-75 nm, average length = 20-40 μm) dispersed in IPA (0.66%) are purchased from Zhejiang Kechuang Advanced Materials Co., Ltd., Zhejiang, China.

4.2.2 Characterization

^{1}H, ^{13}C, homonuclear correlation spectroscopy (COSY), heteronuclear multiple quantum coherence (HMQC), and diffusion ordered spectroscopy (DOSY) nuclear magnetic resonance (NMR) spectra are measured with a JEOL JNM-ECS 400 (JEOL Ltd., Tokyo, Japan) at 25 ℃ temperature at 400 MHz in chloroform-d_1, and chemical shifts are referenced to an internal standard. Size exclusion chromatography (SEC) analysis are using THF as the eluent at a flow rate of 1.0 mL min^{-1} at 40°C and measured by employing a JASCO (JASCO Co., Tokyo, Japan) high-performance liquid chromatography system (PU-980 Intelligent HPLC pump, CO-2065 Plus Intelligent Column Oven, RI-2031 Plus Intelligent RI Detector, and DG-2080-53 Degasser) equipped with a Shodex KF-G guard column (4.6 mm×10 mm; particle size, 8 μm) and two Shodex KF-804L columns (linear; particle size, 7 μm; 8.0 mm × 300 mm; exclusion limit, 4 × 104) (Showa Denko K. K., Tokyo, Japan). The calculated number average molecular weight ($M_{n,\,SEC}$) and the dispersity ($Đ$) of the polymers are calibrated with polystyrene (PSt) standards. Ultraviolet-visible (UV-visible) spectra are measured by Jasco V-370 spectrophotometer (JASCO Co., Tokyo, Japan). The photoluminescence (PL) spectra are measured by a Fluorolog-3 spectrofluorometer (Horiba Jobin Yvon, Paris, France), and the polymer films are excited at wavelengths of 365 nm. The structure of the polymer thin films is imaged by Hitachi AFM5000II (Hitachi Systems Co., Ltd., Tokyo, Japan) operating in tapping mode under an ambient atmosphere. The thin films for the atomic force microscopy (AFM) measurements are

prepared by spin coating (3000 rpm, 60 s) from the polymer solutions in THF (5.0% w/w) onto a silicon substrate. The thin film samples are annealed under vacuum at 120 °C for one day. The AFM images are processed using Gwyddion software. Differential scanning calorimetry (DSC) is measured to investigate thermal properties under a nitrogen atmosphere by Hitachi DSC 7000X (Hitachi High-Tech Science Co., Ltd., Tokyo, Japan) with a heating/cooling rate of 10 °C min^{-1} from −100 °C to 250 °C under a nitrogen flow. Thermogravimetric analysis (TGA) is performed through a Bruker AXS TG-DTA2010SAT (Bruker AXS, Billerica, USA) with a heating rate of 10 °C min^{-1} from 100 °C to 500 °C under a nitrogen flow. Synchrotron grazing-incidence wide-angle X-ray scattering (GIWAXS) measurements are conducted with an X-ray beam of wavelength (λ) 0.12359 nm at the 3C beamline[24-27] of the Pohang Accelerator Laboratory (PAL), Pohang, Korea. A 2D charge-coupled detector (model Eiger X 4M, DECTRIS Ltd., Baden-Daettwil, Switzerland) is used to measure all GIWAXS data. The incidence angle α_i of the X-ray beam for the film sample surface is set in the range 0.093–0.196°, which is between the critical angle of the polymer film and the silicon substrate ($\alpha_{c,f}$ and $\alpha_{c,s}$). Aluminum foils are used as a semi-transparent beam stop. The sample-to-detector distance (SDD) is set to 208.3 mm. Each scattering pattern is collected for 30 s. The scattering angles are corrected according to the positions of the X-ray beams reflected from the silicon substrate as well as using precalibrated silver behenate standards (Tokyo Chemical Inc., Tokyo, Japan). The absolute PLQY measurement is recorded by using Enli Tech LQ-100X (Enli

Technology Co., Ltd., Kaohsiung, Taiwan) for detecting all-polymer thin films under different strains or stretching cycles through the integrating sphere at a fixed excitation wavelength at 365 nm. The optical microscope (OM) observation is measured under a microscope by LSM 21 510 Meta (ZEISS Co., Ltd., Oberkochen, Germany) equipped with a 22 LCI Plan-Neofluar 40x 1.3^{-1} NA immersion. The international commission on illumination (CIE) color coordinates and correlated color temperature (CCT) of the LED spectra are measured by PR670 spectroradiometer (Titan Electro-Optics Co., Ltd., Taipei, Taiwan) under ambient air at 25 °C. The calibration method is standard sunset light, which is correlated to a color temperature of 2856 K, this is done to confirm the instrument's correctness. The time-resolved photoluminescence (TR-PL) spectra are coupled to a Horiba iHR320 spectrometer (HORIBA, Kyoto, Japan) with a Hamamatsu C10910 streak camera and an M10913 slow single sweep unit. Temperature-dependent photoluminescence is measured with a pulsed diode-laser by PicoQuant LDH-D-C-375 (PicoQuant, Berlin, Germany) at a repetition rate of 1 MHz.

4.2.3 Arrhenius formula simulation of the binding energy

Here, the photo-generated excitons are assumed to be depopulated only by thermal dissociation and radiative recombination. In the steady-state PL measurement, the n_{Pg} refers to the number of photo-generated excitons. n_{PL} is the number of the radiative emissions induced by the exciton recombination, which can be determined from the integrated PL intensity.

n_{td} is the number of thermally dissociated excitons. According to the Arrhenius formula, n_{td} is saturated when temperature (*T)* is not too high and the $n_{td} \propto Ae^{-E_b/kT}$ can get, in which E_b is the binding energy and k is the Boltzman constant. Assuming that when $T = \infty$, $n_{PL} = 0$, then $n_{PL} = n_{Pg} - n_{td} = A(1 - e^{-E_b/kT})$. After fitting $n_{td}(T)$, we can determine A and E_b.

$$n_{PL} = n_{pg} - n_{td} = A(1 - e^{-E_b/kT}) \quad (1)$$

4.2.4 The time decay curve fitting by an exponential function

The decays are fitted with the formula (2) where τ_1 is the time constant, which is attributed to the intrinsic recombination and A_1 is the fractions of the contribution. The first 1.0 ns following the laser excitation are used for fitting. The time constant of all the dots measured is around 0.0 ~ 1.0 ns. If the time constant is determined by a nonradiative channel, the distribution of exciton would expect a more rapid decline in time constant.

$$F(t) = A_1 e^{-t/\tau_1} \quad (2)$$

4.2.5 Synthesis of PF-based block copolymers with ring-opening polymerization monomer through a smart one-pot procedure

The typical polymerization procedure is as follows: An appropriate amount of TBD (0.026 mmol, 1 equiv.), 4-iodobenzyl alcohol (0.026 mmol, 1 equiv.), and δ-DL (1.538 mmol, 60 equiv.) are added to an oven-dried Schlenk flask equipped with a magnetic stir (The PA or AA is 0.513

mmol, 20 equiv with EGE (1.026 mmol, 40 equiv) is added). The Schlenk flask is placed in an aluminum heating block with a predetermined temperature of 25 °C to start the ROP (100°C for the PA or AA with EGE). During the ROP step, a crude aliquot is withdrawn from the system by pipette and monitored by ^{1}H NMR spectroscopy, and the SEC determines monomer conversion and molecular weight. After the defined time, $Pd_2(dba)_3{\cdot}CHCl_3$ (0.010 mmol, 0.4 equiv.), *t*-Bu_3P (0.057 mmol, 2.2 equiv. as 0.5 mol L^{-1} stock solution in tetrahydrofuran (THF)), and dry-THF (12 mL) are added to the reaction mixture and is stirred for 30 minutes to form Pd-initiator complex. A solution of HexFL (0.466 mmol, 18 equiv.) in dry-THF (200 mL) is introduced to the Pd-initiator solution, which has been purged with argon and pre-cooled at −10°C by a cannula to start the SCTP for 10 minutes. To terminate the polymerization, 12M hydrochloric acid (HCl) (10ml) is added to the reaction mixture for 30 minutes. SEC is performed to trace the final copolymers. The elution peaks of the copolymers shift to a shorter elution time than those for the corresponding I-PDL$_n$, which indicates a successful chain extension of the PFN block. After removing the solvent by evaporation, the residue is dissolved in CH_2Cl_2 and washed with brine. The organic layer is dried over $MgSO_4$ and purified by alumina column. The residue is diluted by adding THF and poured into cold acetone. The precipitate is collected by filtration and dried under reduced pressure to get PFN_{18}-*b*-PDL_{36} (yield: 63.1 %) as a dark green powder. $M_{n,NMR}$ = 12,800 g mol^{-1}; $Đ$ = 1.31. ^{1}H NMR (400 MHz, $CDCl_3$): δ (ppm) 7.71-7.83 (m, Ar-H of PF backbone), 5.18 (d, -CH_2OH): 2.29 (br, -

$CH_2(CH_2)_4CH_3$ of PF side chain), 0.79-1.27 (m, -$CH_2(CH_2)_4CH_3$ of PF side chain), 4.87 (br, PDL backbone and side-chain connection), 1.27-2.29 (br, PDL backbone), and 0.87-1.55 (br, pentyl side chain of PDL).

4.2.6 Touch-responsive light-emitting diodes fabrication

The PU substrates are prepared by being spin-coated onto the polytetrafluoroethylene (PTFE) substrate and is cured at 40 °C for 1 day. The PU substrates are oxygen plasma treated for 3 min and the PEDOT: PSS/ poly(ethylene glycol) (PEO) (5 wt%) solution is spin-coated onto the treated PU substrate at 1000 rpm for 30 s. Subsequently, the film is annealed at 80 °C for 15 min to remove residual solvents. After being cooled down, the substrate is transferred into a nitrogen-filled glove box and is spin-coated with the PF-based BCP, as an emissive layer. The emissive layer is prepared by spin coating at 3000 rpm for 60 s and annealed at 120 °C in a vacuum for 1 day, and then, the spacer polyethylene terephthalate (PET) is introduced onto the emissive layer. The prepared PU@AgNWs electrode is then faced down and stacked onto the emissive layer that plays the role of a cathode (upper electrode) **(Scheme 4.1)**.

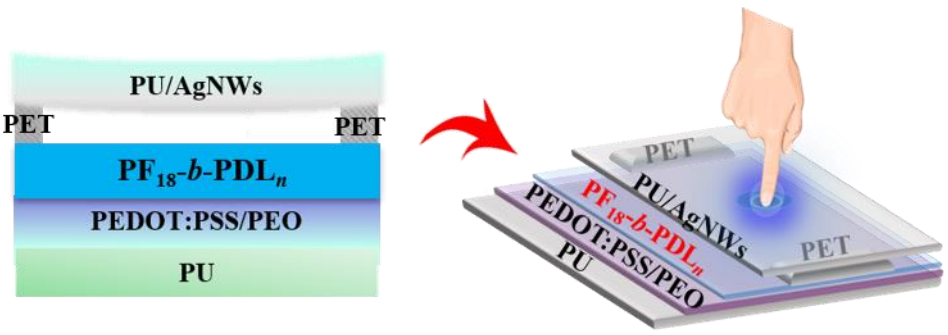

Scheme 4.1. Schematic illustration of touch-responsive LED.

4.3 Results and Discussion

4.3.1 Synthesis and structure characterization of PFN-b-PDL BCPs

The details one-pot synthesis of PFN_{18}-*b*-PDL_n BCPs are given in the **Experimental Section** and illustrated in **Figure 4.1a,** and the detailed molecular characteristics are summarized in **Table 4.1**. The aforementioned synthesis is a two-step process based on the ROP of *δ*-decanolactone (*δ*-DL) and SCTP of potassium 2-(7-bromo-9,9-di-*n*-hexyl-9H-fluorene-2-yl) triolborate (HexFL) in a sequential manner. The tedious purification is not required but the overall synthesis becomes very efficient. To enable the one-pot process, commercially available 4-iodobenzyl alcohol, difunctional initiator possessing hydroxyl, and iodobenzene groups are used. The hydroxyl group functions as the initiating site for ROP, and the iodobenzene group reacts with Pd(0) to form an initiating site for SCTP. First, ROP of *δ*-DL performed in bulk is carried out by using 1,5,7-triazabicyclo[4.4.0]dec-5-ene (TBD) as a catalyst and 4-iodobenzyl alcohol as an initiator. This is performed at 25 °C under a nitrogen atmosphere to produce iodoend-functionalized PDLs [I-PDL_n (n = 13, 24, and 34; **Figure 4.1a,b**)]. The molecular weight control of I-PDL_n is achieved by varying the reaction time and *δ*-DL/initiator ($[\delta\text{-DL}]_0/[I]_0$) ratio. The ROP is monitored by performing ^{1}H NMR analysis of aliquots at regular intervals producing a linear correlation between the evolution of the molecular weight ($M_{n,SEC}$) and monomer conversion, which indicates a living polymerization behavior **(Figure 4.1–4.7** and **Table 4.2)**. Subsequent addition of a mixture of a tris(dibenzylideneactone) dipalladium

(0)-chloroform adduct ($Pd_2(dba)_3 \cdot CHCl_3$) and tri-*tert*-butylphosphine (*t*-Bu_3P) results in the formation of a coordination complex with I-PDL_n initiating a controlled chain-growth SCTP of HexFL.[23] To understand the effect of the molecular weight balance between the conjugated and coil blocks on the LED performance, the PF blocks in all BCPs are synthesized with a fixed theoretical molecular weight ($M_{n,NMR}$) of 6,300 g mol^{-1} (*i.e.*, ca. 18 repeating units). On the other hand, the ring-opening alternating copolymerization (ROAC) of epoxides with cyclic anhydrides has been recognized as a promising approach to diversified polymers and allowing facile functional tunability. In view of achieving facile approach, the utilized commercially available initiator bridges two different catalytic reactions involving ring-opening alternating copolymerization (ROAC) of epoxide (EGE) and cyclic anhydrides (PA or AA) with SCTP of conjugated PF opens up the smart one pot synthetic strategy of PF-based conjugated BCPs **(Figure 4.8-4.11)**. The synthetic strategy works efficiently in constructing diverse PF-based BCPs as it acts straightforward, and functions facile in regulating the molecular blocks with desired physical properties. Through smart synthetic approach, the author synthesizes series of PF-based BCPs namely PFN_{18}-*b*-PDL_{13}, PFN_{18}-*b*-PDL_{24}, PFN_{18}-*b*-PDL_{36}, PFN_{18}-*b*-(PA-*alt*-EGE)$_{20}$, and PFN_{18}-*b*-(AA-*alt*-EGE)$_{20}$, which represents the ease and flexibility in attaining desired degree of polymerization without any purification steps.

Although a series of BCPs are prepared, the author focus primitively on PFN_{18}-*b*-PDL_n as main theme of this chapter is to fabricate bio-derived stretchable wearable LEDs. The ^1H, ^{13}C,

and 2D NMR spectra are used to confirm and analyze the chemical compositions of PFN_{18}-*b*-PDL_n, as shown in **Figures 4.12**. In the ^1H NMR spectrum **(Figure 4.1c)**, the proton signals are originated from the hexyl side chain on the PFN block (peaks a, b, and c) and the main chain of the PDL block (peaks d, e, f, and g) are observed for PFN_{18}-*b*-PDL_{34}. The ^1H, ^{13}C, and 2D NMR peak positions and their peak integration values for all BCPs are in good agreement with the chemical structures and target molecular weights. DOSY NMR analysis is a powerful tool for accurately identifying individual NMR spectra from a mixture of various chemical species, and the analysis is performed to determine the capability of the novel synthesis for producing a single type of BCP. The DOSY NMR spectra reveal only a single diffusion peak, which proves that only one copolymer was produced through smart one-pot synthesis **(Figure 4.13a)**. In contrast, two diffusion peaks are observed for a mixture of PFN and PDL homopolymers **(Figure 4.13b)**. The NMR spectra and SEC traces suggest that well-defined BCPs are produced through the novel smart synthesis process. The novel synthesis is a simple, high yielding (typically 65%–67%),[3-4,18,20,22] and short reaction process (~2 h); thus, this method is beneficial for the mass production of copolymers.

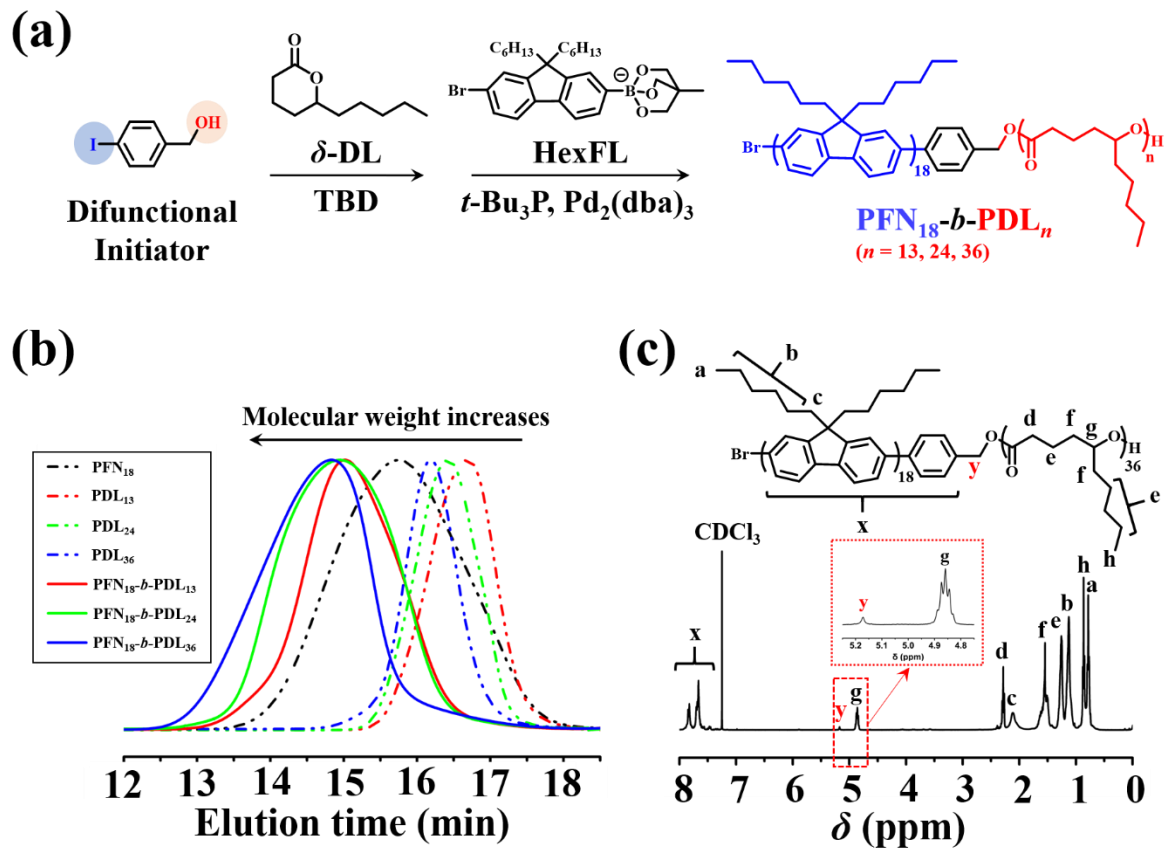

Figure 4.1. (a) Smart synthesis of PFN_{18}-*b*-PDL_n block copolymers by combining ROP and SCTP. (b) SEC trace of studied polymers via the smart synthesis in THF calibrated with polystyrene (PS) standards. (c) The ^1H NMR with peak designation and (d) DOSY NMR spectrum of the PFN_{18}-*b*-PDL_{36} in $CDCl_3$.

Table 4.1. Smart synthesis of PF-based conjugated block copolymer under TBD or *t*-BuP_1 using difunctional initiator.

Run	Sample	$[M]_{ROP}$: $[M]_{HexFL}$: $[Initiator]_0$: $[TBD]_{ROP}$	Time (min)	T (°C) [ROP, SCTP]	Conv. (%) (ROP)	Conv. (%) (HexFL)	$M_{n,NMR}$ [b] (g mol^{-1})	$M_{n,SEC}$ [c] (g mol^{-1})	$Đ$ [c]	Yield (%)
1	PFN_{18}	0:18:1:0	10	-10	-	>99	6,300	11,000	1.328	82.1
2	$PDL_{13,\ TBD}$	60:0:1:1	30	rt	23.20	-	2.300	3,100	1.223	53.8
3	$PDL_{24,\ TBD}$	60:0:1:1	90	rt	39.10	-	3.900	5,000	1.106	75.2
4	$PDL_{36,TBD}$	60:0:1:1	120	rt	59.38	-	6,000	8,800	1.128	80.3
5	PFN_{18}-*b*-$PDL_{13,\ TBD}$ [a]	0:18:1:1	10	-10	-	>99	8,500	14,300	1.393	68.3
6	PFN_{18}-*b*-$PDL_{24,\ TBD}$ [a]	0:18:1:1	10	-10	-	>99	10,500	16,200	1.303	70.2
7	PFN_{18}-*b*-$PDL_{36,\ TBD}$ [a]	0:18:1:1	10	-10	-	>99	12,500	20,000	1.353	63.1
8	PFN_{18}-*b*-$PDL_{13,\ TBD}$	60:18:1:1	40	rt, -10	22.47	>99	7,400	14,600	1.233	67.5
9	PFN_{18}-*b*-$PDL_{24,\ TBD}$	60:18:1:1	100	rt, -10	38.41	>99	10,100	16,300	1.252	66.8
10	PFN_{18}-*b*-$PDL_{36,\ TBD}$	60:18:1:1	130	rt, -10	59.47	>99	12,800	18,500	1.311	65.3
11	PFN_{55}-*b*-$PDL_{55,\ TBD}$	80:55:1:1	210	rt, -10	68.24	>99	26,880	28,700	1.503	63.2
12	PFN_{18}-*b*-(PA-*alt*-EGE)$_{20,\ t\text{-}BuP1}$	20:20:18:1:0.5	100	100, -10	>99	>99	10,860	12,200	1.326	73.5
13	PFN_{18}-*b*-(AA-*alt*-EGE)$_{20,\ t\text{-}BuP1}$	20:20:18:1:0.5	160	100, -10	>99	>99	10,600	14,800	1.351	52.3

[a]The reaction was conducted after purification (dialysis) of the PDL. [b]Calculated by ^1H NMR spectroscopy of the polymers in $CDCl_3$. [c]Determined by SEC analysis in THF calibrated with polystyrene standards. (The ROP is conducted in bulk at 25°C, [TBD or *t*-BuP_1]:[4-iodobenzyl alcohol]:[δ-DL] = 1 : 1 : 60(80); SCTP is conducted in THF at -10°C, $[Pd_2(dba)_3]$:[*t*-Bu_3P]:[4-iodobenzyl alcohol]:[HexFL] = 0.4 : 2.2 : 1 : 18.

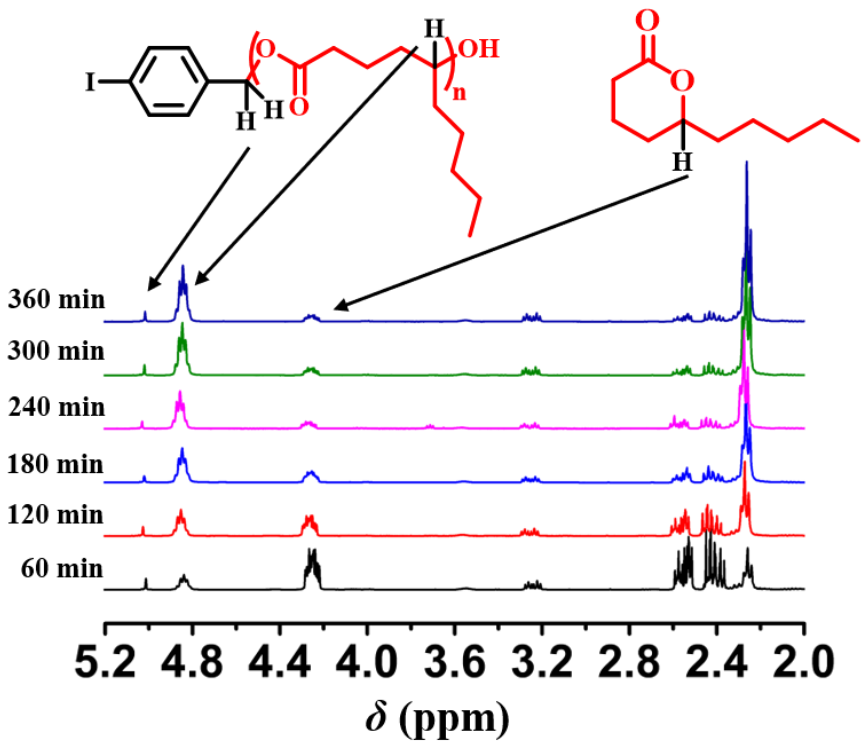

Figure 4.2. The ^{1}H NMR spectrum of crude aliquots withdrawn from the reaction system for monitoring the conversion of δ-DL formation of polymer. (The ROP was conducted in bulk at 25℃, [TBD]/[4-Iodobenzyl alcohol]/[δ-DL]=1:1:60)

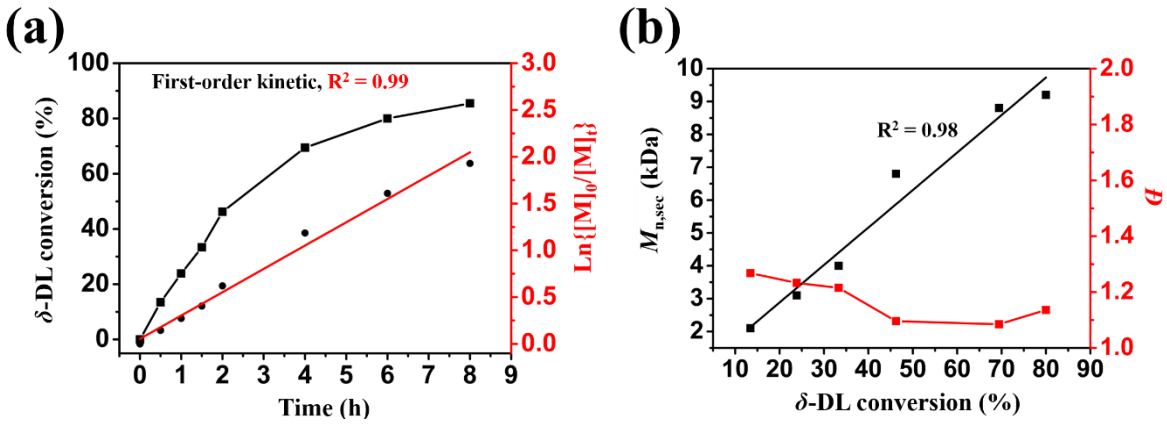

Figure 4.3. (a) Polymerization time versus δ-DL conversion and Ln($[M]_0/[M]_t$). (b) The plots of $M_{n,sec,}$ and $Đ$ versus δ-DL conversion for indicating a controlled polymerization by TBD. (The polymerization was conducted in bulk at 25℃, [TBD]/[4-Iodobenzyl alcohol]/[δ-DL]=1:1:60)

Table 4.2. The ROP of δ-DL catalyzed by TBD[a].

Run	Time (min)	Conv.[b] (%)	TOF (min^{-1})	$[M]_0/[M]_t$	$Ln\{[M]_0/[M]_t\}$	$M_{n,SEC}$[c] ($g\ mol^{-1}$)	$Đ$[c]
1	30	13.44	0.45	1.15	0.14	2,100	1.268
2	60	23.86	0.40	1.31	0.27	3,100	1.233
3	90	33.33	0.37	1.51	0.41	4,000	1.215
4	120	42.23	0.35	1.85	0.62	6,800	1.096
5	240	69.44	0.29	3.29	1.19	8,800	1.085
6	360	80.00	0.22	6.89	1.93	9,200	1.136

[a]The polymerization reactions are conducted in [TBD]:[4-Iodobenzyl alcohol]:[δ-DL] = 1 : 1 : 60 under 25°C. [b]The conversion of δ-DL is determined by ^{1}H NMR spectroscopy. [c]$M_{n,SEC}$ and $Đ$ are determined by SEC analysis in THF calibrated with polystyrene standards.

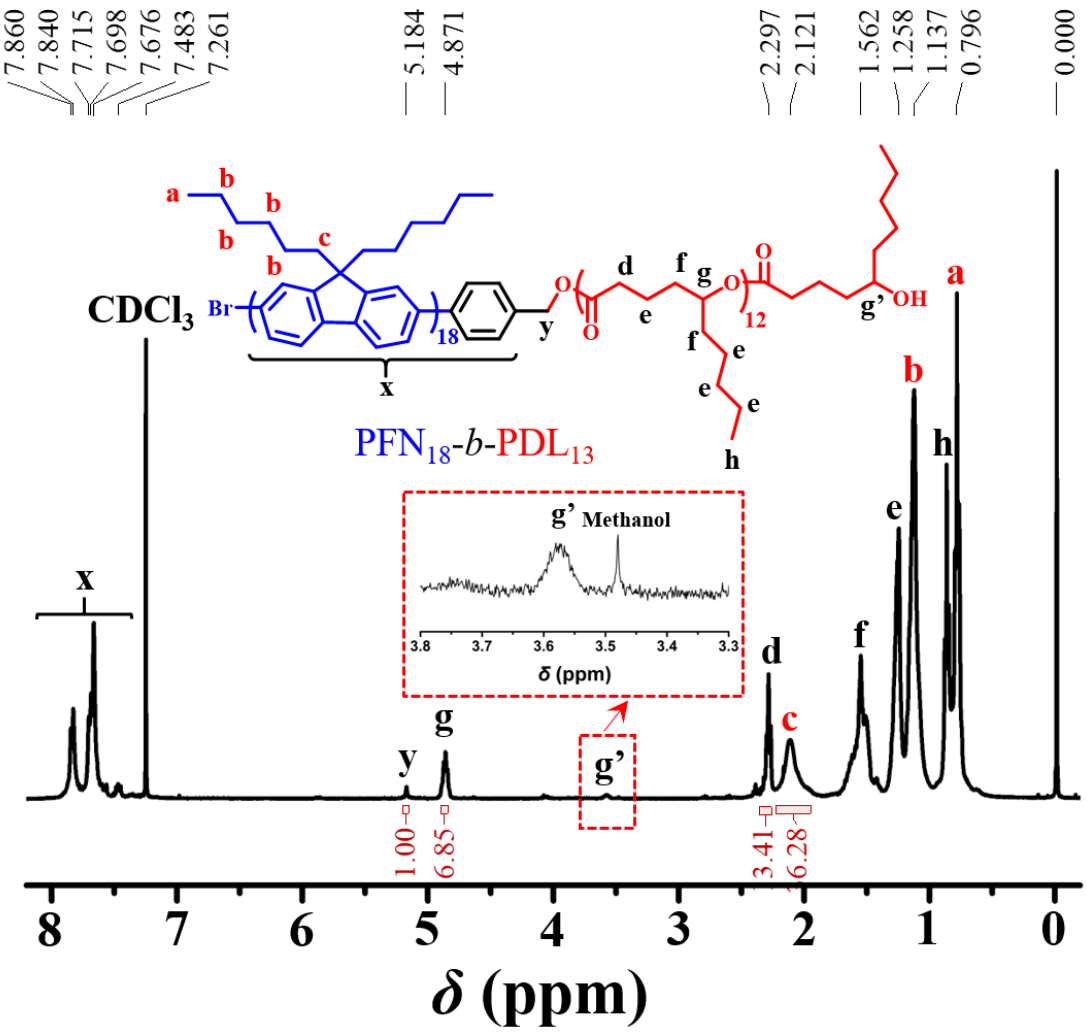

Figure 4.4. The ^{1}H NMR spectrum of the resultant PFN_{18}-*b*-PDL_{13} via smart synthesis isolated from the mixture by precipitation in cold toluene.

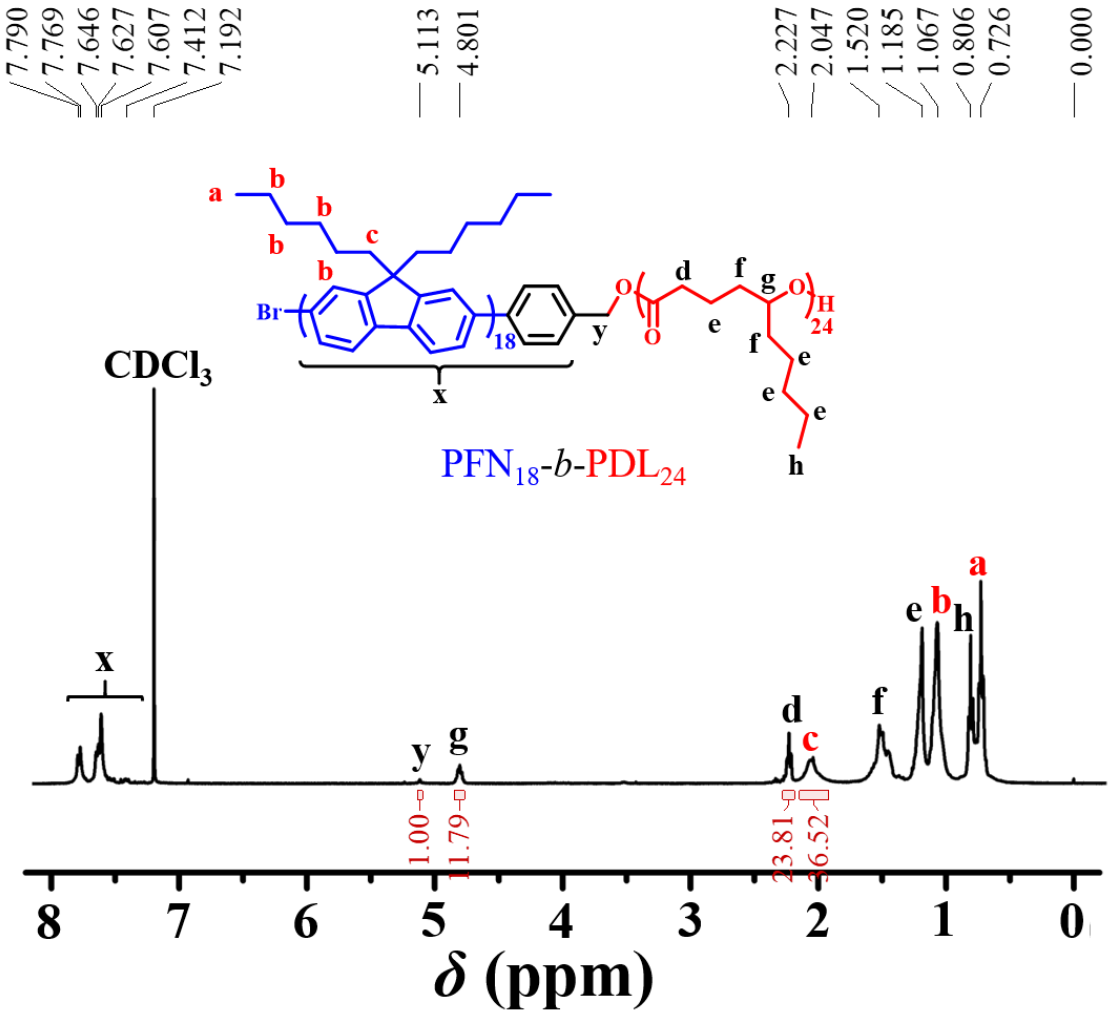

Figure 4.5. The ^{1}H NMR spectrum of the resultant PFN_{18}-*b*-PDL_{24} via smart synthesis isolated from the mixture by precipitation in cold toluene.

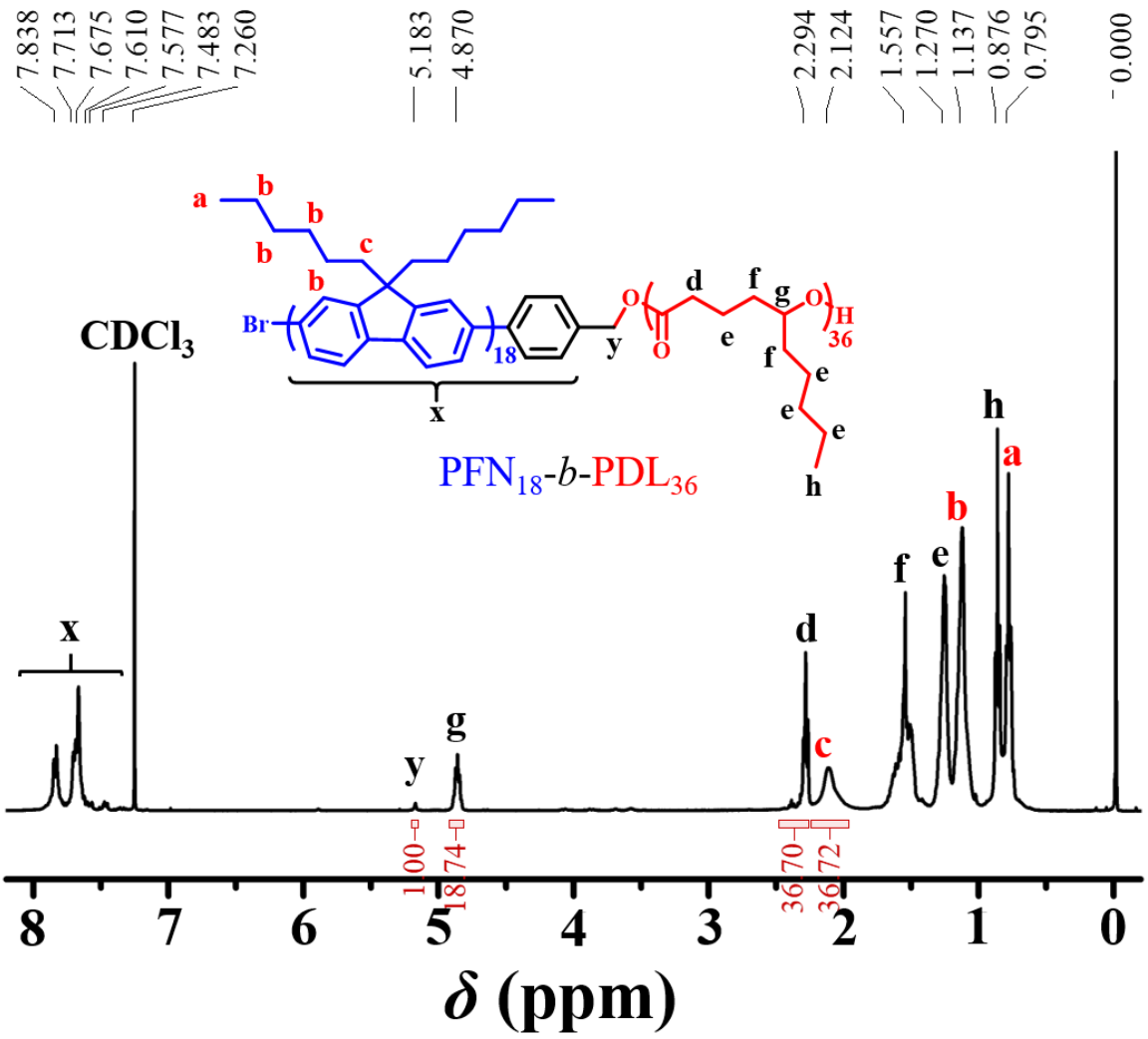

Figure 4.6. The ^{1}H NMR spectrum of the resultant PFN_{18}-*b*-PDL_{36} via smart synthesis isolated from the mixture by precipitation in cold toluene.

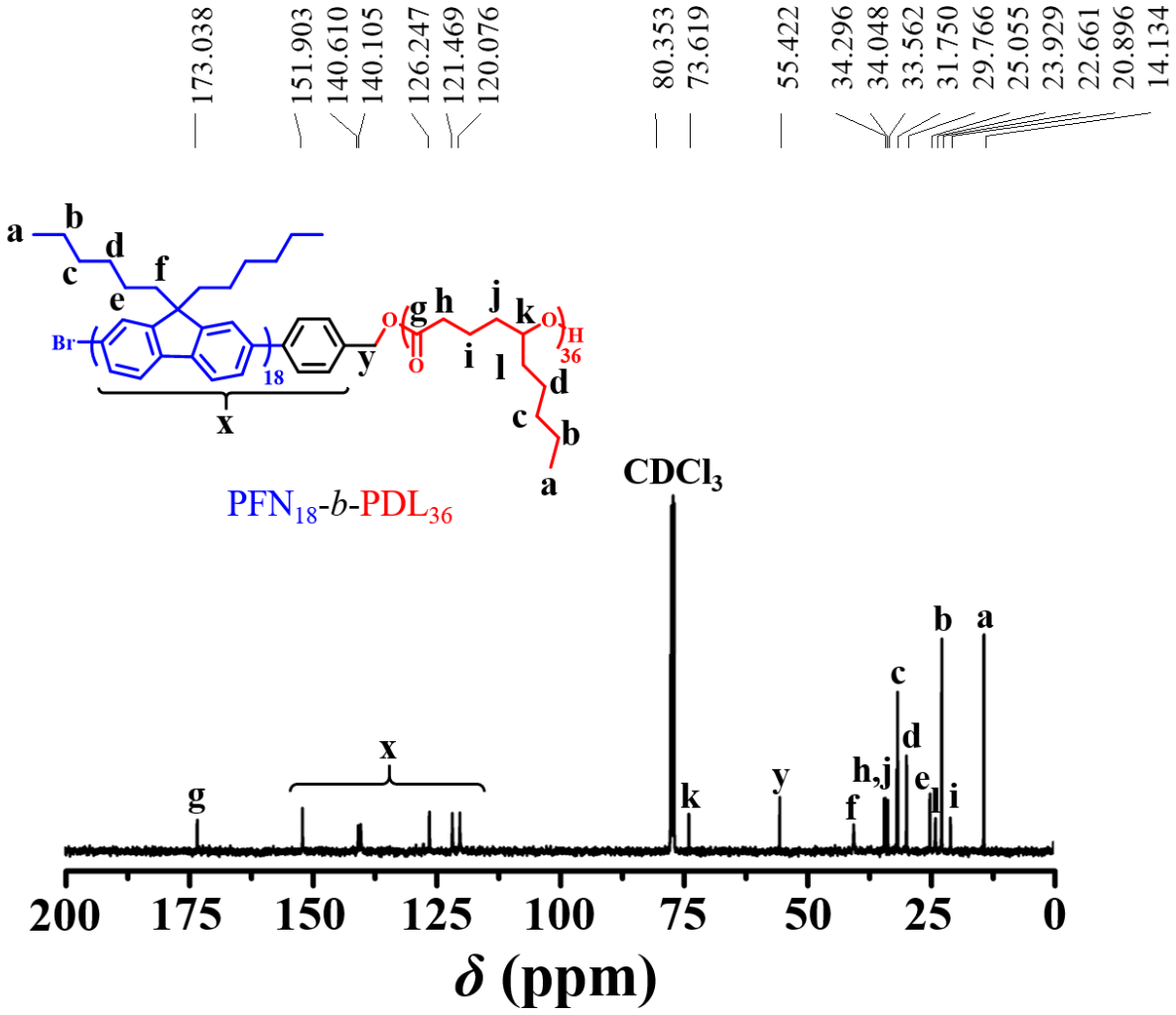

Figure 4.7. The ^{13}C NMR with peak designation of the polymerization of PFN_{18}-*b*-PDL_{36} via smart synthesis.

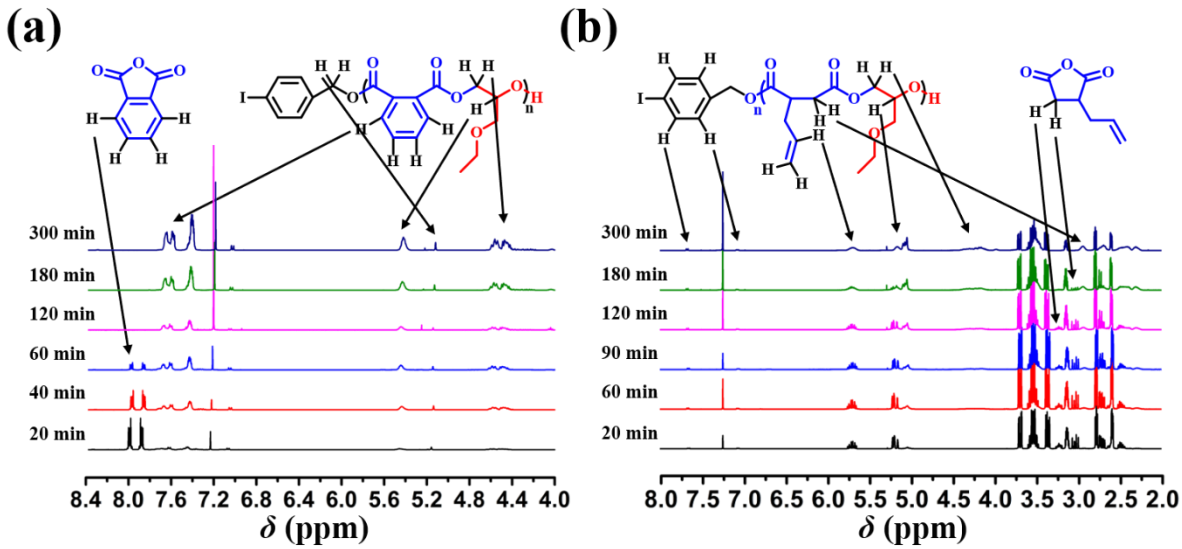

Figure 4.8. The ^{1}H NMR spectrum of crude aliquots withdrawn from the reaction system for monitoring the conversion of EGE and the formation of an alternative copolymer (a) PA-*alt*-EGE and (b) AA-*alt*-EGE.

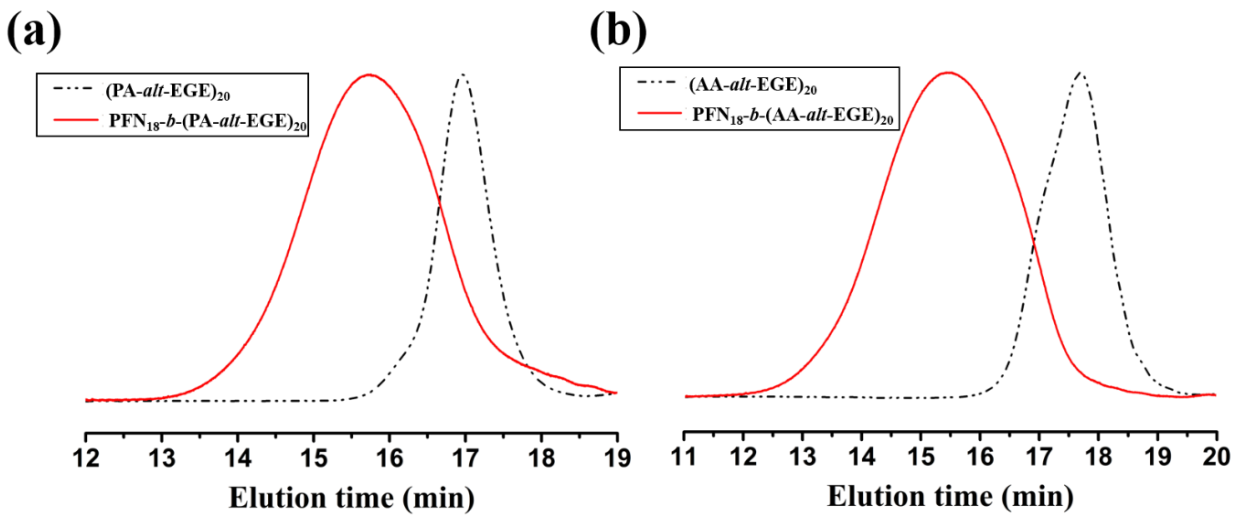

Figure 4.9. Evolution of SEC traces after Suzuki–Miyaura catalyst transfer polymerization (SCTP) (a) PFN_{18}-*b*-(PA-*alt*-EGE)$_{20}$ and (b) PFN_{18}-*b*-(AA-*alt*-EGE)$_{20}$.

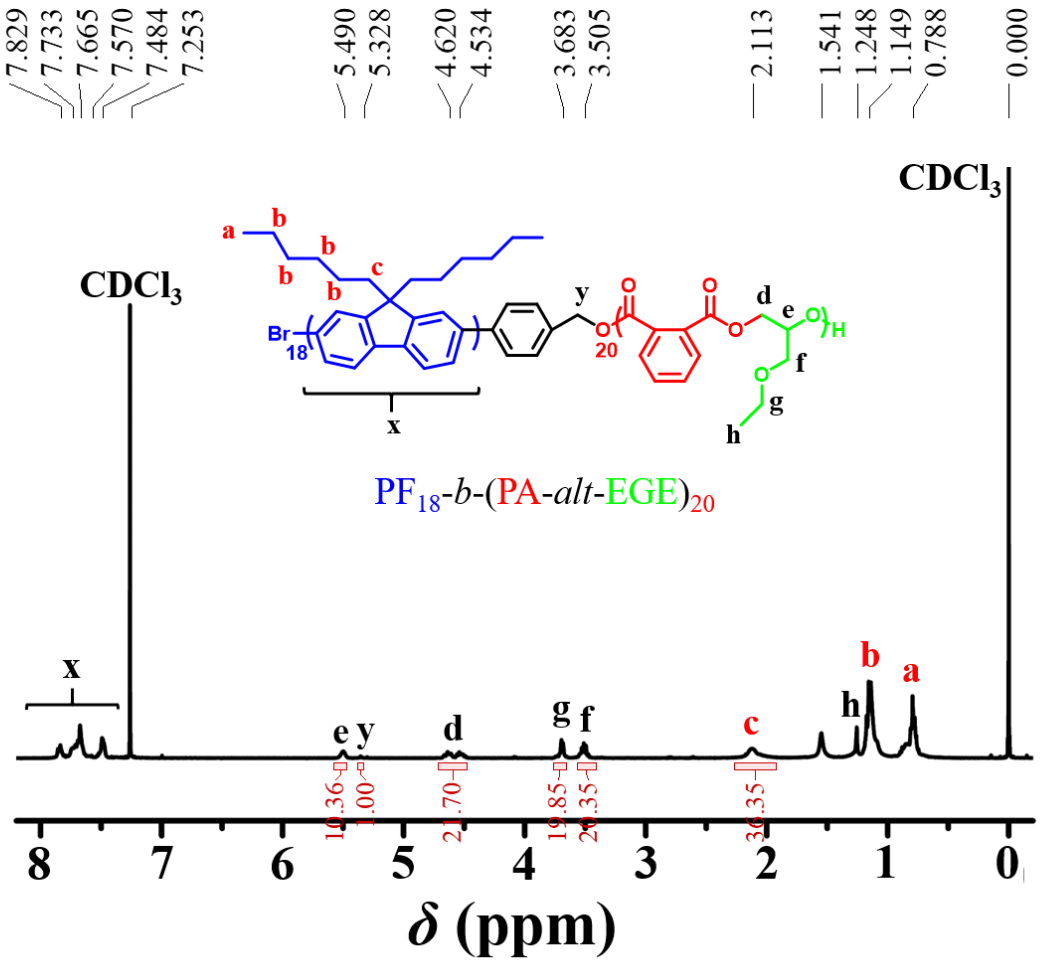

Figure 4.10. The ^{1}H NMR spectrum of the resultant PFN$_{18}$-*b*-(PA-*alt*-EGE)$_{20}$ via smart synthesis isolated from the mixture by precipitation in cold toluene.

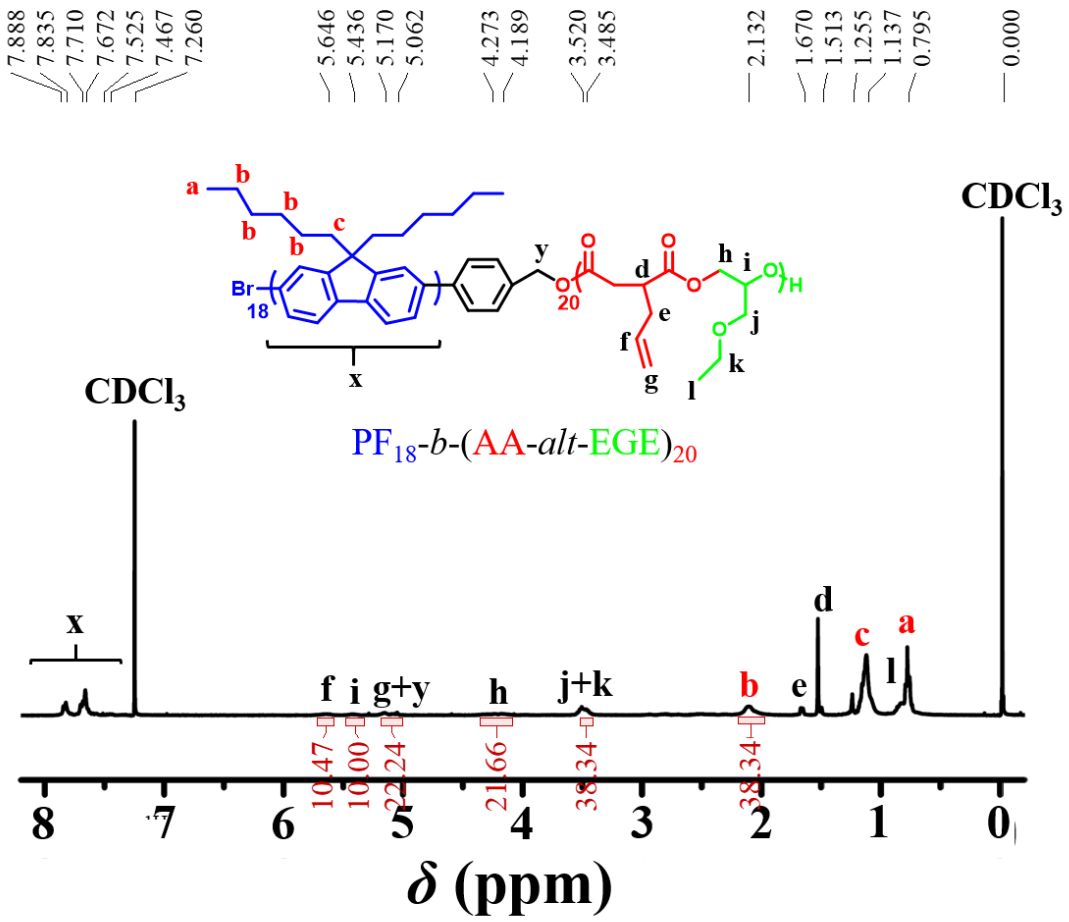

Figure 4.11. The ^{1}H NMR spectrum of the resultant PFN$_{18}$-*b*-(PA-*alt*-EGE)$_{20}$ via smart synthesis isolated from the mixture by precipitation in cold toluene.

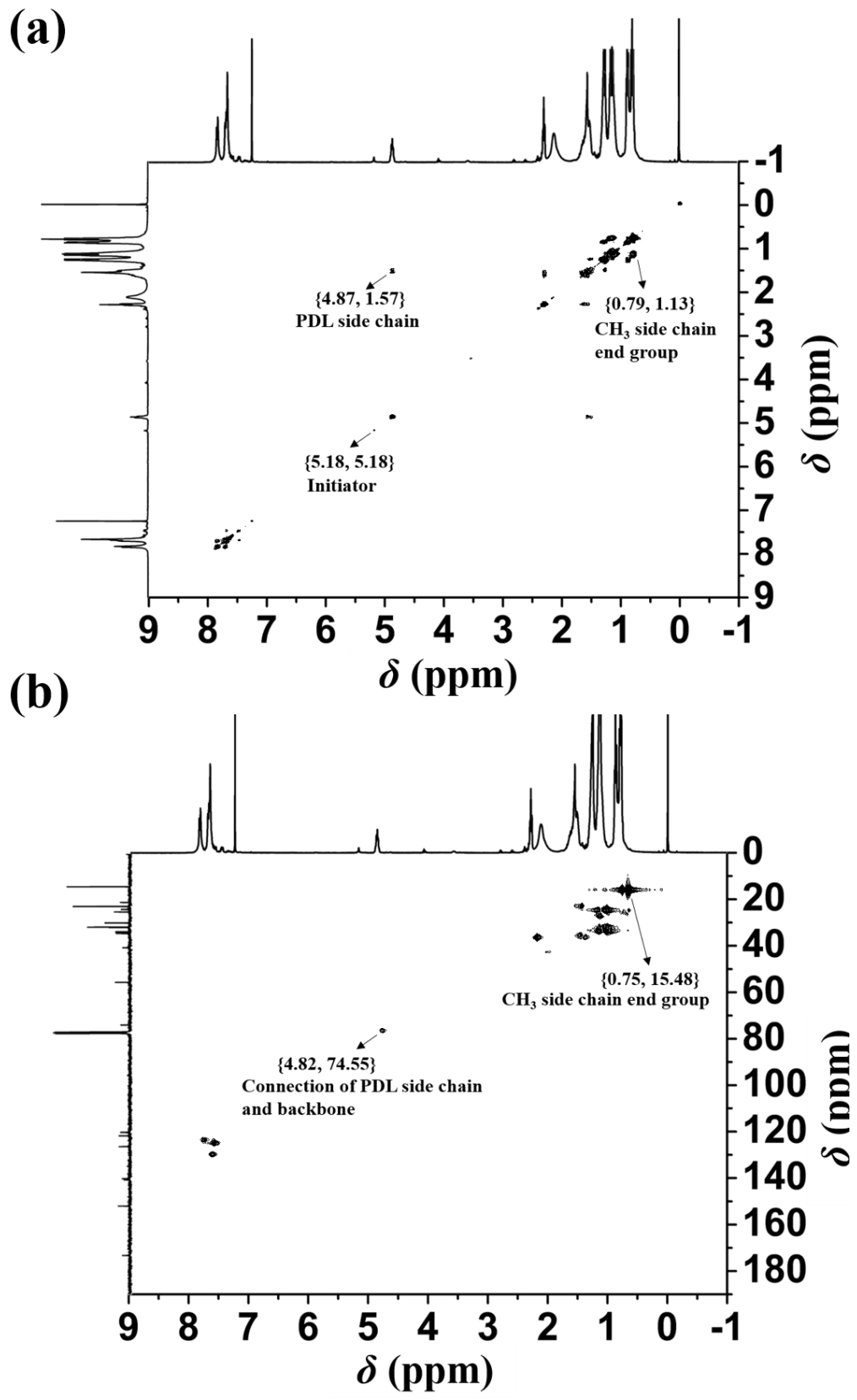

Figure 4.12. The representative ^{1}H, ^{13}C, and 2D NMR spectra of the PFN_{18}-*b*-PDL_{36} in $CDCl_3$.

(a) COSY and (b) HMQC.

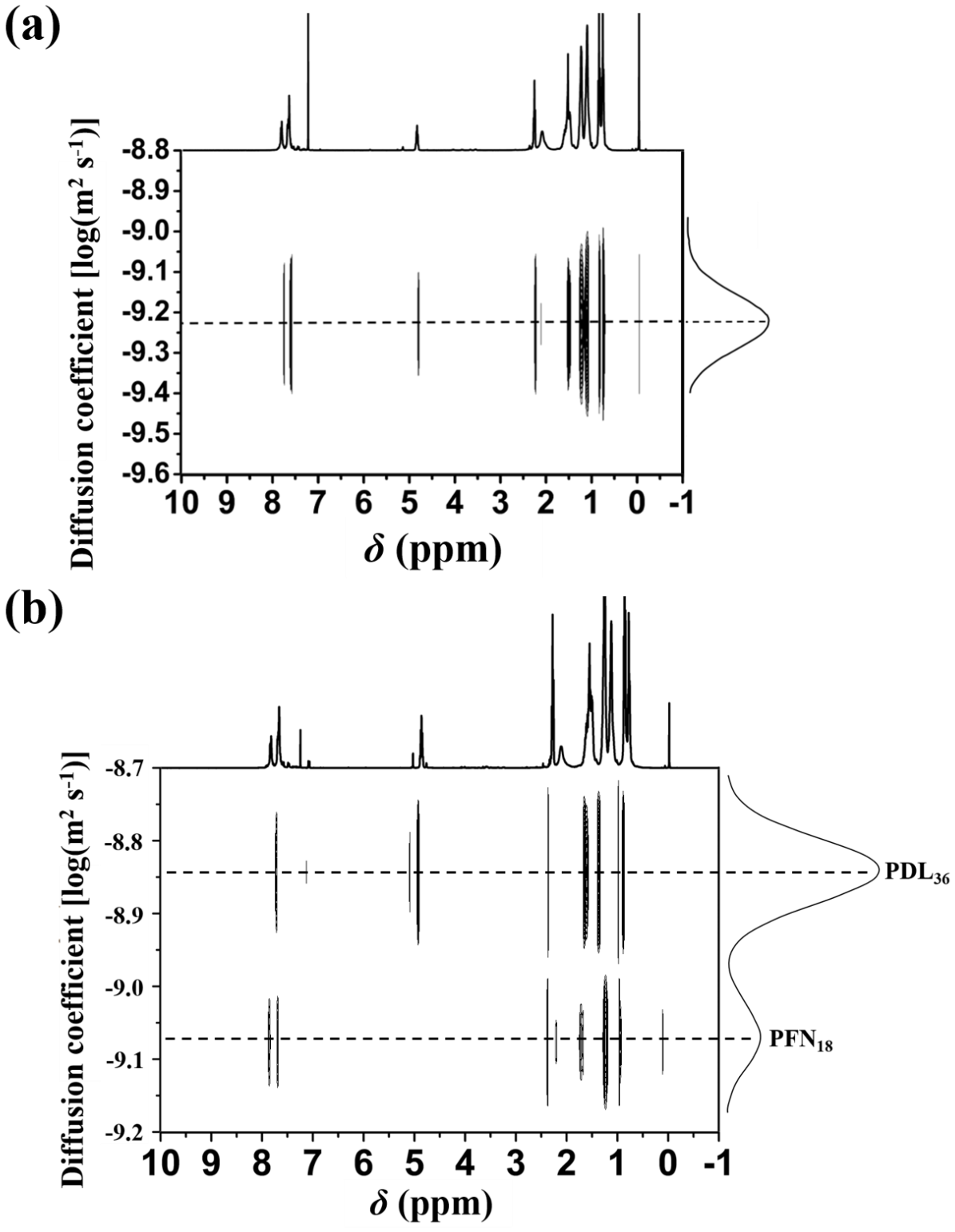

Figure 4.13. The DOSY NMR spectrum of the (a) PFN_{18}-*b*-PDL_{36} and (b) PFN_{18} and PDL_{36} blending sample in $CDCl_3$.

4.3.2 The Physical and Optical Properties of the PFN-b-PDL Thin Films

The thermal behavior of PFN_{18}-*b*-PDL_n is examined through TGA and DSC **(Figure 4.14)** under a nitrogen atmosphere. The thermal parameters are summarized in **Table 4.3**. The homopolymer of PDL and PFN reveals glass transition temperatures (T_g) at −55.2 and 69.1 °C. As displayed in **Figure 4.14b-c**, each PFN_{18}-*b*-PDL_n copolymers exhibited two T_g, which originated from PDL and PFN, respectively. The existence of individual phase transitions is indicated in the immiscibility of the PFN and PDL blocks. Thus, PFN and PDF are segregated into separate domains.

The thin film morphologies of PFN_{18}-*b*-PDL_n copolymers are investigated through synchrotron GIWAXS measurements on as-cast and thermally annealed films (120 °C in vacuum for 1 day). As for PFN_{18} homopolymer, the as-cast film revealed featureless data but the thermally annealed film revealed a set of weak crystalline peaks **(Figure 4.15a,b)**. BCPs crystalline peaks are attributed to the formation of an orthorhombic crystalline structure similar to that of poly(9,9-di-*n*-octyl-2,7-fluorene) (PFO).[28] In addition, a weak peak at approximately 16.8° in both out-of-plane and in-plane directions is observed with a *d*-spacing value of 4.2 Å, which evidence the existence of π-π stacking between PFN chains. However, the relatively weak peak intensities suggest low PFN crystallinity inside the annealed film. A similar result is observed for PFN_{18}-*b*-PDL_{13} **(Figure 4.15c,d)**, with a minor difference in the annealed film, in which the scattering peaks are even weaker than PFN homopolymer suggesting an even

lower crystallinity. As for PFN_{18}-*b*-PDL_{24} and PFN_{18}-*b*-PDL_{36} **(Figure 4.15e-h)**, the as-cast films revealed scattering peaks appearing as halos suggesting that the orientation of PFN crystals is not controlled. Post-annealing, peaks begin to take a similar appearance to that of PFN homopolymer, with PFN_{18}-*b*-PDL_{36} revealing a relatively more similar scattering pattern. AFM is performed to further investigate the phase separation behavior. As shown in **Figure 4.16**, the as-cast films of PFN homopolymer and copolymers are featureless but a fibrillar structure is observed on the surface of thermally annealed films for all BCPs. GIWAXS results ascertain the observed fibril morphological features originating from the tight packing of the PFN blocks promoted by intermolecular π–π interactions and linked PDL blocks offer amorphous matrix around the PF fibers.

To further investigate the correlation between the conformation and optical properties of the studied polymers, the UV–vis absorption and PL spectra of the as-cast thin films are evaluated **(Figure 4.17a)** and summarized in **Table 4.4**. The UV–vis absorption spectra of the as-cast films reveal that both PFN homopolymer and PFN_{18}-*b*-PDL_n copolymers exhibit π–π* transition occurring in the PFN segment at a wavelength of approximately 403 nm. To confirm the luminescence properties, PLQY of as-cast thin films are evaluated **(Figure 4.17b)**. The conjugated BCPs exhibit higher PLQY (32%–37%) than that of PFN homopolymer (24%), which confirms the superior luminescent property of the BCPs for LED devices. The aforementioned result is in agreement with those of previous studies.[21,22] A higher PLQY is

correlated to a large EBE,[28-29] which indicates radiative recombination of excitons at room temperature occurring more efficiently in block copolymer films.

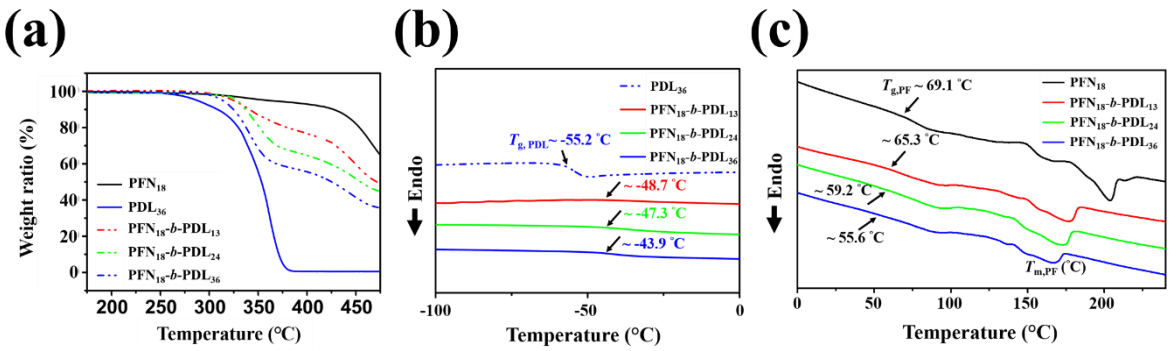

Figure 4.14. (a) The TGA curves of studied polymers under heating rate of 10 °C·min^{-1}. (b) DSC heating of T_g from PDL and (c) PFN at a fixed heating/cooling rate of 10 °C·min^{-1}.

Table 4.3. Thermal properties of studied polymers.

Sample	T_d [a] (°C)	T_g [b] (°C)	T_m [c] (°C)	T_c [d] (°C)
PFN_{18}	341.7	69.1	203.8	143.9
PDL_{36}	270.8	-55.2	--	--
PFN_{18}-*b*-PDL_{13}	302.3	65.3, -58.7	176.7	130.4
PFN_{18}-*b*-PDL_{24}	308.5	55.2, -57.3	172.9	122.3
PFN_{18}-*b*-PDL_{36}	292.5	52.6, -53.9	166.7	124.5

[a]Degradation temperature at the heating/cooling rate of 10°C min^{-1} in thermogravimetric analysis (TGA) in a nitrogen atmosphere. [b]Midpoint temperature of glass transition at a heating rate of 10°C min^{-1} in differential scanning calorimetry (DSC) in a nitrogen atmosphere. [c]Melting temperature. [d]Crystallization temperature at a cooling rate of 10°C min^{-1} in differential scanning calorimetry (DSC) in a nitrogen atmosphere.

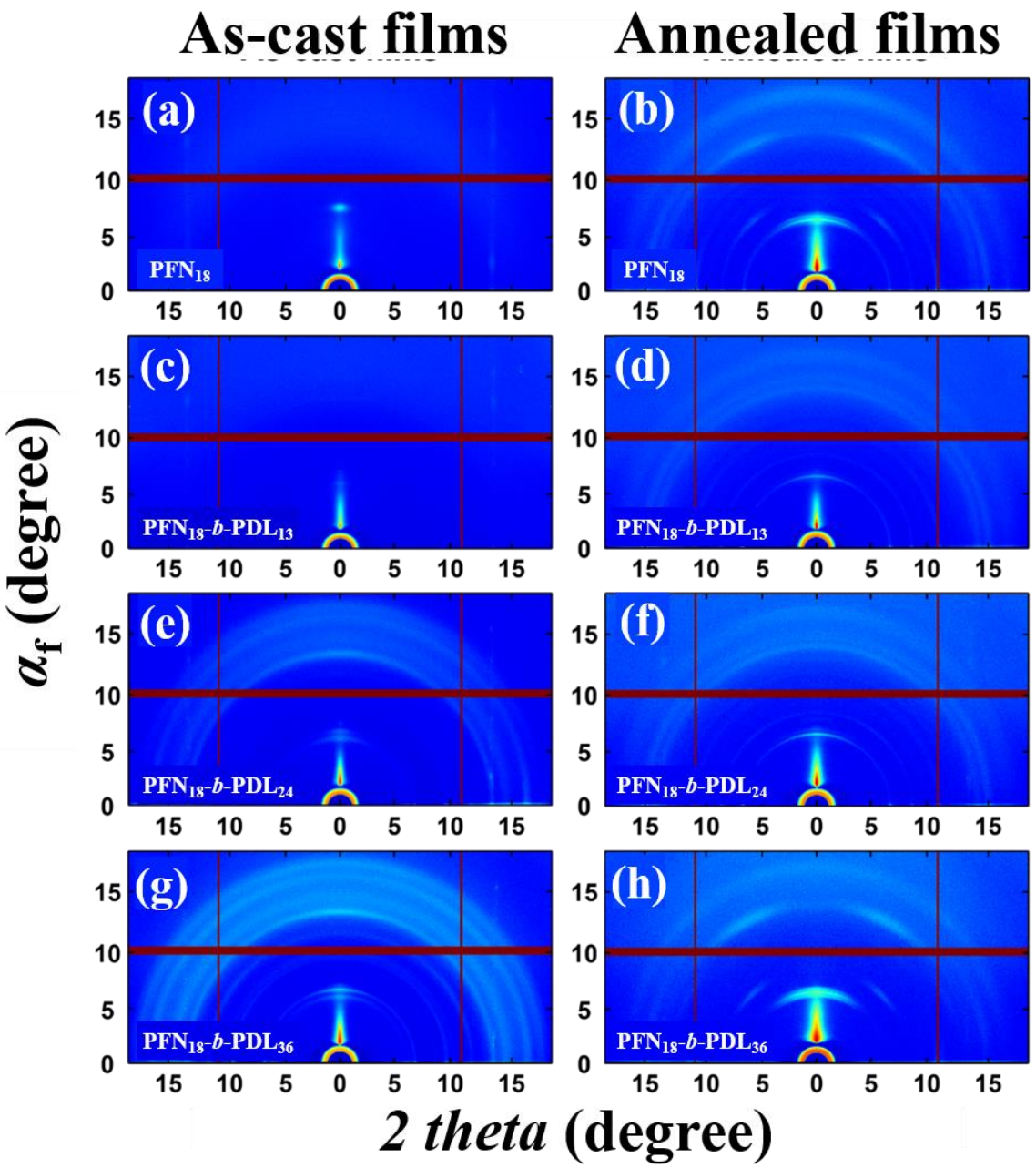

Figure 4.15. Synchrotron GIWAXS data of thin films of block copolymers measured with SDD = 208.3 mm at room temperature using a synchrotron X-ray beam (λ = 0.12359 nm). (a) PFN_{18} as-cast film (α_i = 0.144°). (b) PFN_{18} annealed film (α_i = 0.155°). (c) PFN_{18}-*b*-PDL_{13} as-cast film (α_i = 0.196°). (d) PFN_{18}-*b*-PDL_{13} annealed film (α_i = 0.155°). (e) PFN_{18}-*b*-PDL_{24} as-cast film (α_i = 0.134°). (f) PFN_{18}-*b*-PDL_{24} annealed film (α_i = 0.155°). (g) PFN_{18}-*b*-PDL_{36} as-cast film (α_i = 0.093). h) PFN_{18}-*b*-PDL_{36} annealed film (α_i = 0.165°).

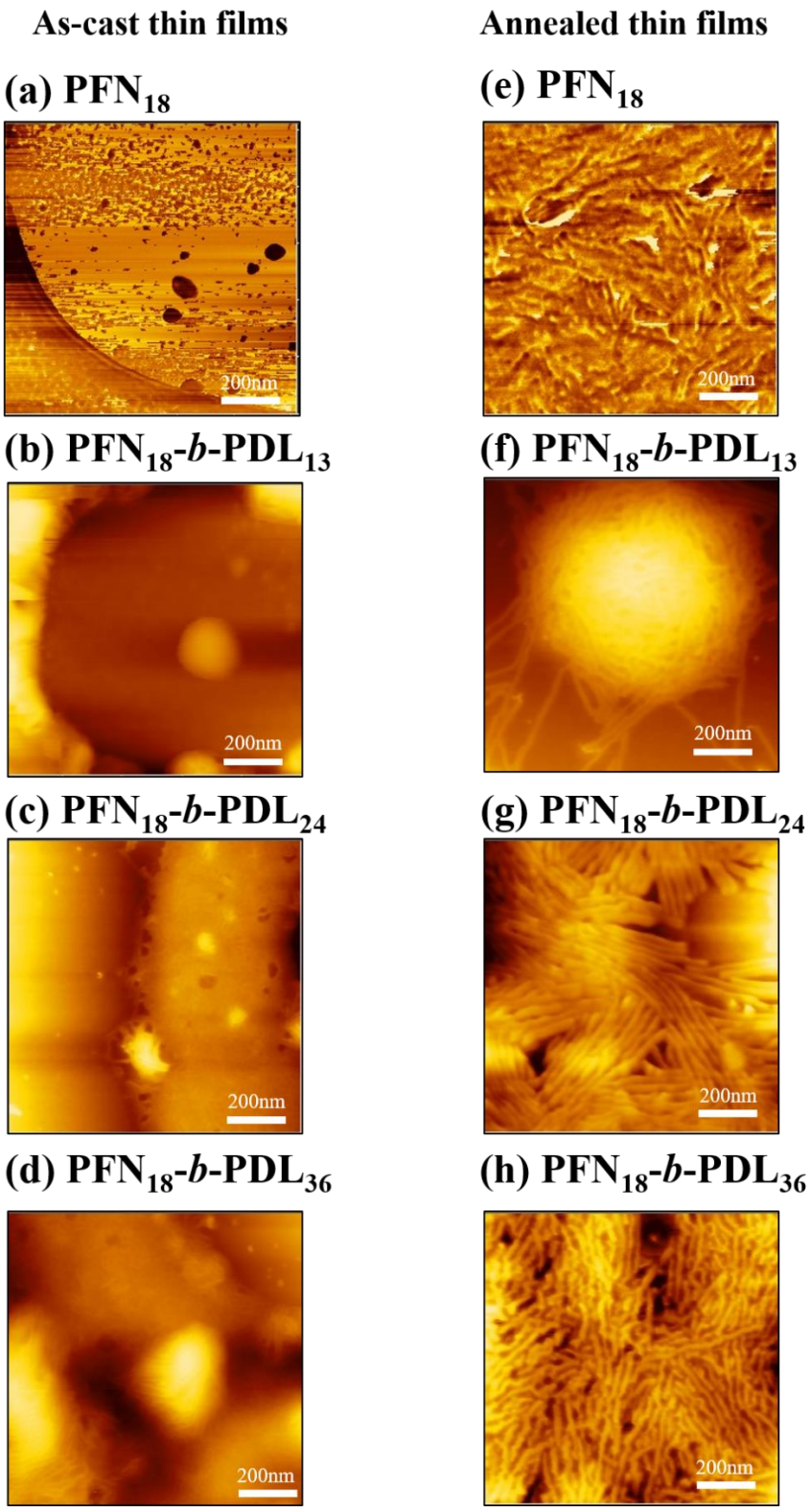

Figure 4.16. The AFM phase images of the as-cast state (a) PFN_{18}, (b) PFN_{18}-*b*-PDL_{13}, (c) PFN_{18}-*b*-PDL_{24}, (d) PFN_{18}-*b*-PDL_{36} and annealing state (e) PFN_{18}, (f) PFN_{18}-*b*-PDL_{13}, (g) PFN_{18}-*b*-PDL_{24}, (h) PFN_{18}-*b*-PDL_{36}.

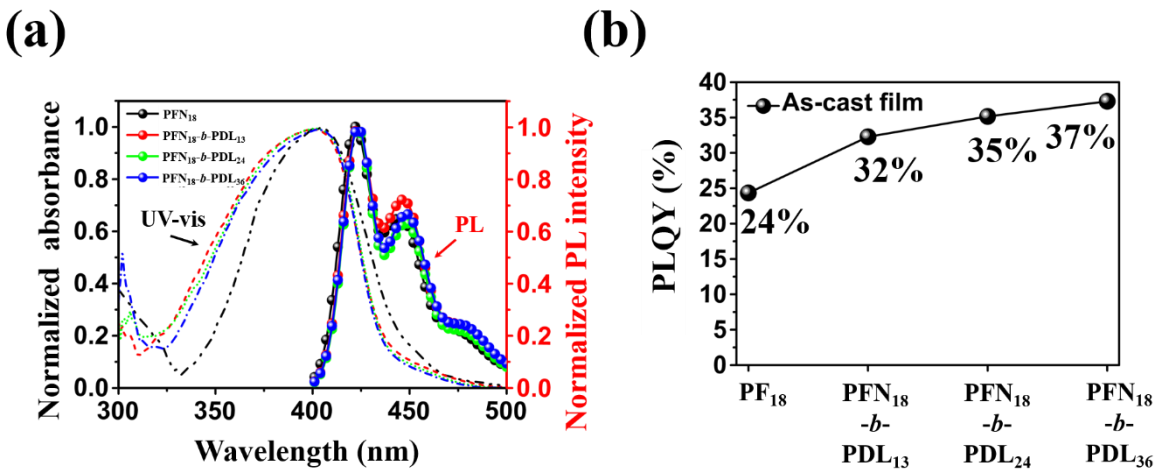

Figure 4.17. (a) UV-vis absorption, PL emission spectra, and (b) PLQY value of as-cast thin film of studied polymers.

Table 4.4. Optical properties of studied polymers.

Sample	Solution [a]		As-cast film [d]		Annealed film [f]	
	λ_{max}^{abs} [b] (nm)	λ_{max}^{PL} [c] (nm)	λ_{max}^{PL} (nm)	PLQY [e] (%)	λ_{max}^{PL} (nm)	PLQY (%)
PFN_{18}	383	420, 441	423, 445	24.33	423, 445	14.43
PDL_{36}	--	--	--	--	--	--
PFN_{18}-*b*-PDL_{13}	383	420, 442	423, 448	32.28	423, 446	28.47
PFN_{18}-*b*-PDL_{24}	383	420, 442	423, 448	35.16	423, 448	25.58
PFN_{18}-*b*-PDL_{36}	383	420, 442	423, 447	37.29	423, 448	22.00

[a]In tetrahydrofuran. [b]Absorption at the longest wavelength. [c]Emission wavelength, excited at 365 nm. [d]The as-cast films of polymers were prepared on a glass substrate by spin-coating polymer solutions in tetrahydrofuran (1 mg mL^{-1}) at 3000 rpm. [e]Absolute PL quantum yield (PLQY) was recorded at an excitation wavelength of 365 nm. [f]The films were annealed at 120 °C in a vacuum for 1 day.

4.3.3 The correlation between PLQY and EBE

Excitons are one of the important factors affecting the performance of an LED device.[30-32] Considering the high PLQY of conjugated BCPs, their EBE plays a critical role in their performance.[29,33] Therefore, temperature-dependent PL measurements are conducted on the PFN homopolymer and PFN_{18}-*b*-PDL_n copolymers to determine their EBE. Both homopolymer and BCPs exhibit a rapid decrease in their PL intensities when increasing temperature from 100 to 300 K **(Figure 4.18)**, indicating a weak attractive force between the electron and a hole in the exciton due to a strong screening effect.[34-35] Furthermore, the integrated PL intensity is fitted with the Arrhenius equation [Equation (1); see **Experimental Section**] to obtain binding energies (E_b) of 40.29, 59.32, 64.99, and 71.91 meV for PFN_{18}, PFN_{18}-*b*-PDL_{13}, PFN_{18}-*b*-PDL_{24}, and PFN_{18}-*b*-PDL_{34}, respectively **(Figure 4.18a)**.

The Arrhenius equation is expressed as follows:

$$n_{PL} = n_{pg} - n_{td} = A(1 - e^{-E_b/kT}) \quad (1)$$

As E_b decreases, PL is quenched, thereby, reducing the recombination of photogenerated charges. This result is consistent with the PLQY results. Moreover, the TR PL spectra **(Figure 4.18b)** and the kinetics are analyzed to investigate the exciton recombination dynamics. All studied samples exhibit exponentially decay PL intensities. PFN homopolymer exhibits a

lifetime (τ_{avg}) of 0.117 ns **(Table 4.5).** PFN_{18}-*b*-PDL_{13}, PFN_{18}-*b*-PDL_{24}, and PFN_{18}-*b*-PDL_{34} exhibit longer τ_{avg} of 0.137, 0.155, and 0.169 ns, respectively. Rapid dissociation and separation of exciton recombinations resulted in a rapid decline in the magnitudes of the fast component (τ_1) (the fitting exponential function is shown in the **Experimental Section**). As τ_{avg} decreases, the electrons in the excited state transitioned to the ground state, which enhanced the nonradiative transition ratio.[36-37] τ_{avg} of PFN_{18}-*b*-PDL_n copolymers are longer than that of the PFN homopolymer because higher EBE of the copolymers stabilizes the bound state. According to previous studies, extremely high EBE can be achieved in crystalline emissive materials by adding low-dielectric-constant organic components.[34] The presence of low-dielectric PDL blocks induces a weak screening effect and increases the attractive force between electrons and holes. In other words, PDL blocks suppress nonradiative recombination and considerably enhance the EBE of the entire block copolymers. Therefore, the author's results indicate that EBE is considerably enhanced by incorporating PDL blocks, as illustrated in **Figure 4.18c**. The corresponding PLQY promoting in the conjugated block copolymers is attributed to the stable bound state for the excitons induced by the low dielectric PDL block. This finding reveals the potential of conjugated BCPs for fabricating efficient and stable LED devices.

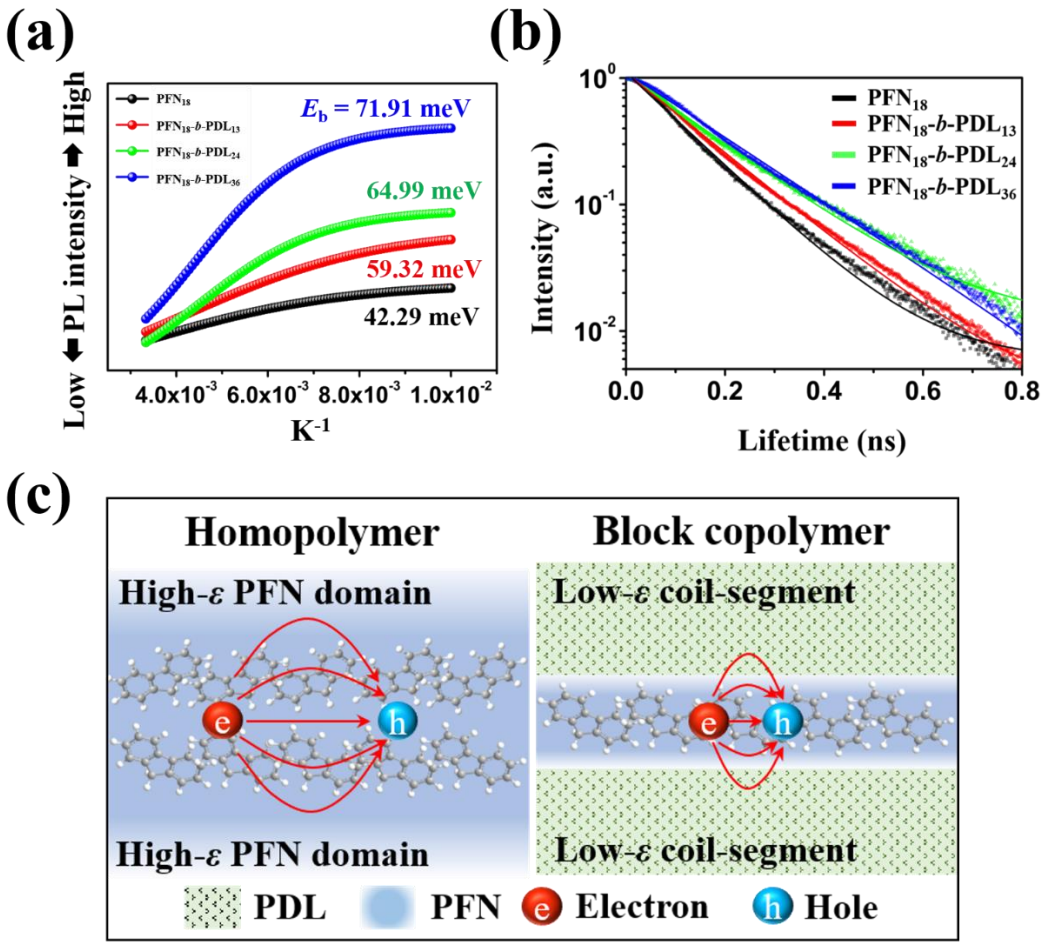

Figure 4.18. (a) Exciton binding energies and (b) TR PL decay fitting curves of studied polymers. (c) Different dielectric constant effect of stable bound state for excitons.

Table 4.5. The time-resolved PL spectra of PFN_{18}-*b*-PDL_n thin films of as-cast state.

Sample	$R^{2\,a}$	$A_1{}^b$	$\tau_1{}^c$	$\tau_{avg}{}^d$
PFN_{18}	0.9966	1.0994	0.1171	0.1171
PFN_{18}-*b*-PDL_{13}	0.9972	1.0929	0.1372	0.1372
PFN_{18}-*b*-PDL_{24}	0.9971	1.0608	0.1547	0.1547
PFN_{18}-*b*-PDL_{36}	0.9965	1.1072	0.1692	0.1692

[a]Regression analysis is constant of the fitting by a single exponential reconvolution of Figure 2d. [b]Number of photons at t = 0. [c]Time constant. [d]An average lifetime.

4.3.4 The performance of stretchable touch-responsive light-emitting diode

The homopolymer and BCPs are fabricated based on the architecture of PU/PEDOT:PSS/PFN$_{18}$-*b*-PDL$_n$/PET/PU with a silver nanowire electrode PU@AgNWs, as displayed in **Figure 4.19a**. The realization of stretchable touch-responsive LEDs involved the following simple concepts. First, only elastic materials are used to withstand the desired total strain. Second, a PET spacer is implanted between the upper electrode and the emissive layer to separate them. Therefore, the device only emits light upon the applied pressure on the upper electrode. The instantaneous light emission in the regions is contacted by a wrench, and emission under 150% strain of PFN$_{18}$-*b*-PDL$_{13}$ LED devices are observed. For practical applications, the operation of stretchable touch-responsive LEDs applied on finger joints is demonstrated and switched on by physical contact between the joint and device upon bending motion.

The luminescence–voltage (*L*–*V*), current density–voltage (*J*–*V*), and current efficiency–voltage (CE–*V*) characteristics are displayed in **Figures 4.19** and **Figure 4.20**, and optimized devices performance are summarized in **Table 4.6**. In as-cast devices using PFN$_{18}$-*b*-PDL$_n$ as the emissive layer show higher EQE$_{as\text{-}cast}$ values (0.054%–0.104%) than using PFN homopolymer (EQE$_{as\text{-}cast}$ = 0.034%) and commercial poly(9,9-di-*n*-octyl-2,7-fluorene) (PFO) homopolymer (EQE$_{as\text{-}cast}$ = 0.039%), as presented in **Table 4.6**. Based on higher PLQY and EBE of block copolymers (PFN$_{18}$-*b*-PDL$_n$), they possess a more stable bound state and a higher

photon emission efficiency than PFN and PFO homopolymers. It is worth noting that current density continuously declines, while EQE drastically decreases with the increasing length of insulating PDL **(Figure 4.19c** and **Figure 4.20d)**. The decline in current density is unfavorable to the recombination event, which results in greatly suppressed emission of PFN_{18}-*b*-PDL_{24} and PFN_{18}-*b*-PDL_{36} devices. Interestingly, PFN_{18}-*b*-PDL_{24} and PFN_{18}-*b*-PDL_{36} devices stop emitting photons after annealing. It can be explained that for these two BCPs the increase in the random conformation of PFN block induced by thermal annealing occurs nearby crystalline regions, which further decreases current density. Hence, the overall resistance within the device becomes too high for proper operation. In contrast, the relatively lower crystallinity of its annealed state and the shortest PDL is sufficiently current/present inside the PFN_{18}-*b*-PDL_{13} device for optimal operation. Therefore, enhanced device performance is achieved by lower crystallinity in PFN_{18}-*b*-PDL_{13}, which results in a minimal increase of PF block with random orientation after annealing and a slightly better orientation with intrinsic high EBE that significantly improve radiative recombinations. Finally, the optimized device with the shortest PDL block (PFN_{18}-*b*-PDL_{13}) exhibited a highly enhanced performance, with a maximum $EQE_{annealing}$ of approximately 0.329% (at 18 V), which is 6 times higher than PFN ($EQE_{annealing}$ = 0.051%) and PFO ($EQE_{annealing}$ = 0.050%) homopolymers.

To understand the correlation between deformation and device performance based on length of PDL block, homopolymer and BCP annealed thin films are characterized with OM **(Figure**

4.21). Furthermore, **Figure 4.22** displays the photographs of annealed PFN and PFN_{18}-*b*-PDL_n LED devices when the emitted light is biased at 19 V under stretching from 0% to 200% strain. Interestingly, only PFN and PFN_{18}-*b*-PDL_{13} devices are functional whereas PFN_{18}-*b*-PDL_{24} and PFN_{18}-*b*-PDL_{36} devices, despite exhibiting improved deformability, suffer failure due to the overwhelming amount of PDL that induces high resistance. PFN_{18}-*b*-PDL_{13} devices show ultra-efficient, touch-responsive performance and high stretchability. These devices demonstrate stable touch-responsive operation at nearly the same level for approximately 300 switch on-off cycles without any sudden decrease in luminance and EQE, as displayed in **Figure 4.23a**. The luminance measured under 0-20% strain cycle and uniaxial strain of 0%-100% are displayed in **Figure 4.23b**. The device exhibits a 13% decrease in luminance at 30% strain, and this indicates the device's wide operational window under high strain. The device retains its comparable performance for 50 stretching cycles, thereby, demonstrating excellent stability and durability from highly repeated strain **(Figure 2.23c)**. All the aforementioned results indicate that the PFN_{18}-*b*-PDL_{13} device demonstrates the highest level of wearable and touch-responsive LED device performance.

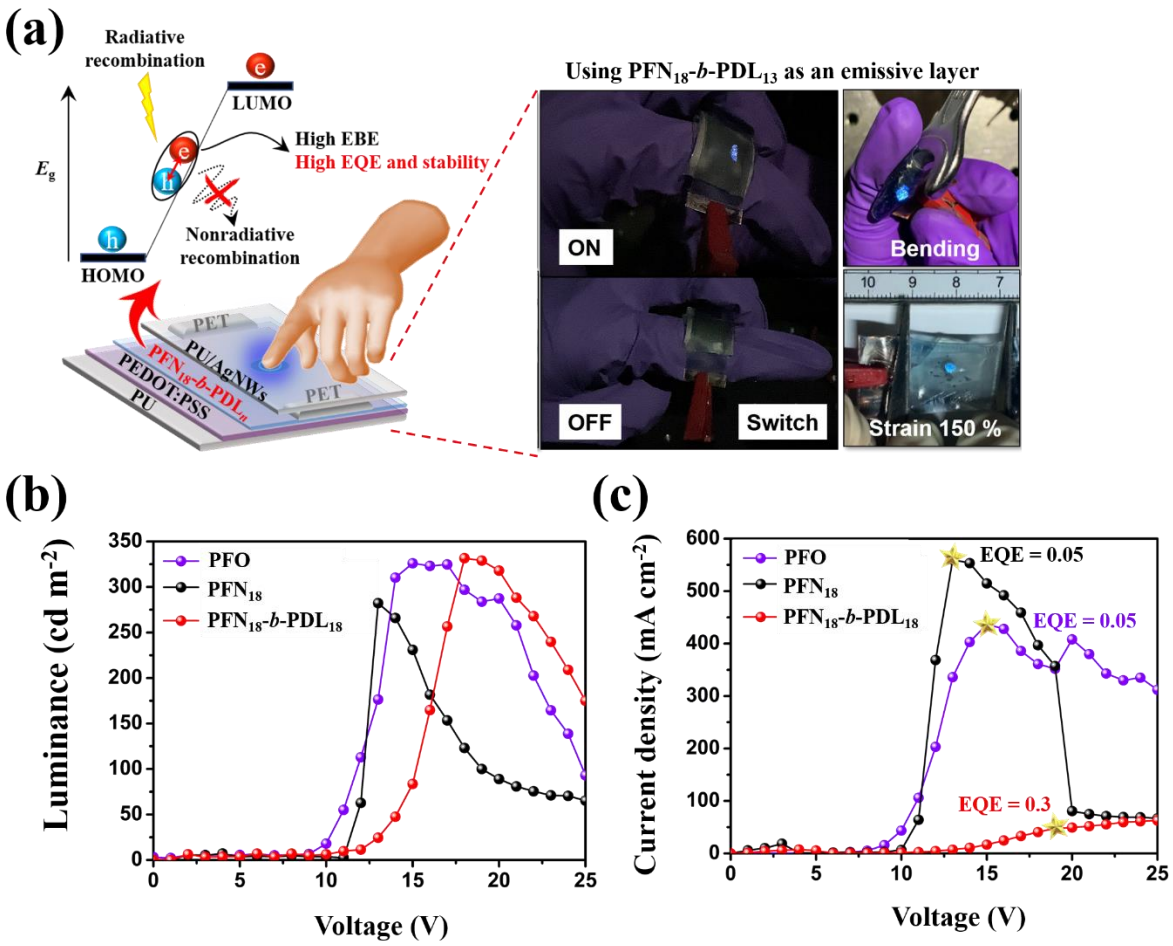

Figure 4.19. (a) schematic of touch-responsive LEDs: Photograph of the bent and touched by a wrench (irregular complex surface), stretched to 150% strain, and attached by the finger using PFN_{18}-*b*-PDL_{13} as an emissive layer (under 19V). (c) *L*-*V* and (d) *J*-*V* characteristics of the touch-responsive LEDs.

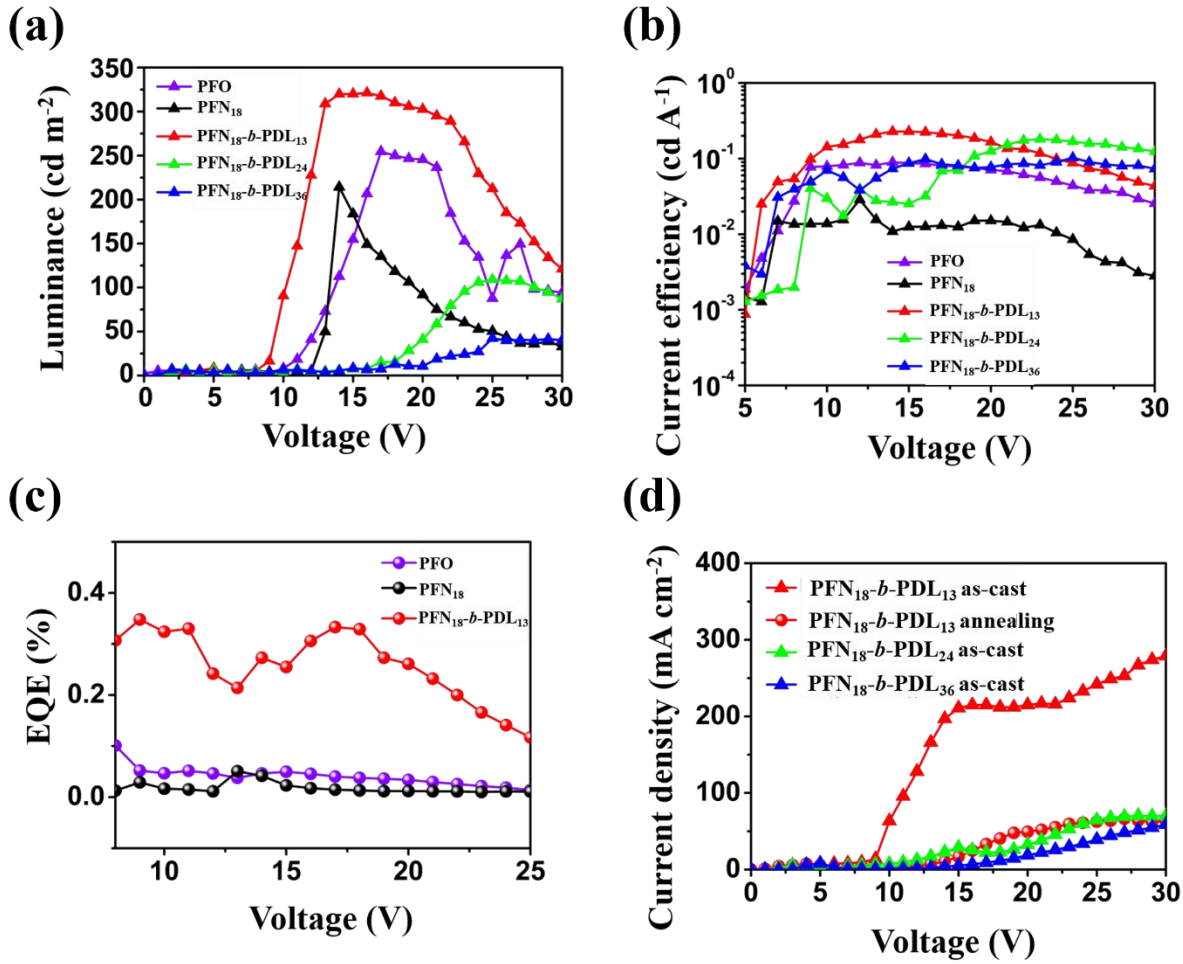

Figure 4.20. (a) *L-V* and (b) *J-V* characteristics of the touch-responsive LEDs. (c) The durable test of luminance and EQE characteristics and (d) luminance under a uniaxial strain from 0 to 100% of the touch-responsive LEDs using PFN_{18}-*b*-PDL_{13} as an emissive layer (under 19V).

Table 4.6. The molecular characteristics, photoelectric properties, and device performance of studied samples.

Sample	Molecular characteristics			Photoelectric properties			Device performances (As-cast film)[b]			Device performances (Annealing film)[b]		
	M_n(k)	$Đ$	ε-DL (wt%)	PLQY (%)	EBE (meV)	τ_{avg}	L_{max} (cd m^{-2})	CE_{max} (cd A^{-1})	EQE (%)	L_{max} (cd m^{-2})	CE_{max} (cd A^{-1})	EQE (%)
PFO	10-40	< 4	0	-	-	-	312.0	0.077	0.034	288.6	0.082	0.036
PFN_{18}	6.30	1.32	0	24.33	42.29	0.117	78.43	0.029	0.021	277.9	0.100	0.081
PFN_{18}-*b*-PDL_{13}	7.40	1.23	30	32.28	59.32	0.137	395.9	0.186	0.084	331.6	0.722	0.292
PFN_{18}-*b*-PDL_{24}	10.1	1.25	40	35.16	64.99	0.155	15.3	0.033	0.037	-	-	-
PFN_{18}-*b*-PDL_{36}	12.8	1.31	48	29.39	71.91	0.169	40.4	0.103	0.054	-	-	-

[a]The sample was an emissive layer of the device. [b]The device performances were recorded at the highest EQE voltage. Device structure: PU/PEDOT:PSS/sample/PET/PU@AgNWs. Annealing condition: 120℃ one day under vacuum state.

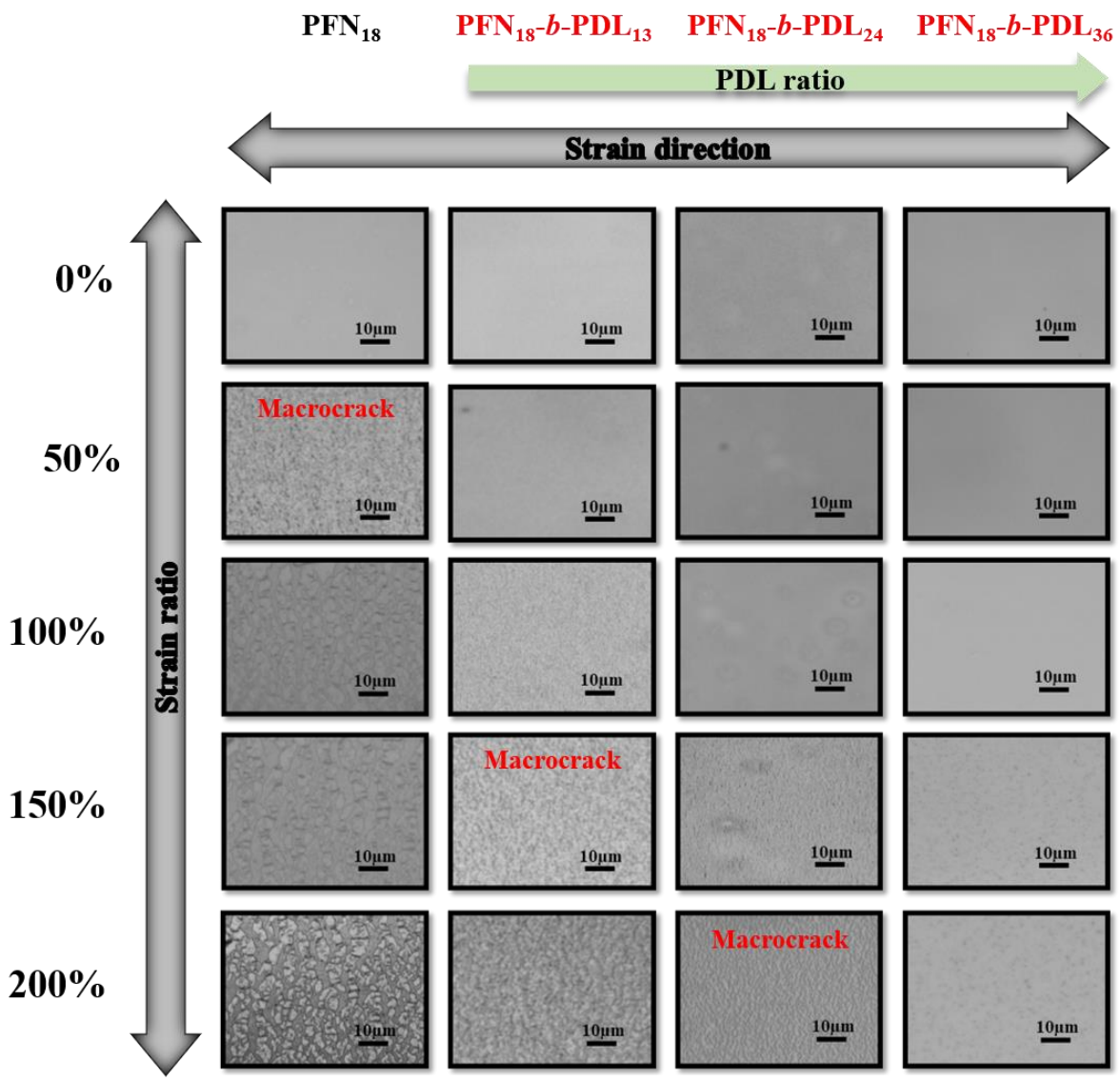

Figure 4.21. The OM images of the studied polymers of as-cast film at the strain of 0, 50, 100, 150%, and 200%.

Figure 4.22. Photos of LED at strains of 0, 50, 100, 150%, 200%, and 250% respectively. (a) PFN_{18} (b) PFN_{18}-*b*-PDL_{13} (c) PFN_{18}-*b*-PDL_{24} (d) PFN_{18}-*b*-PDL_{36}.

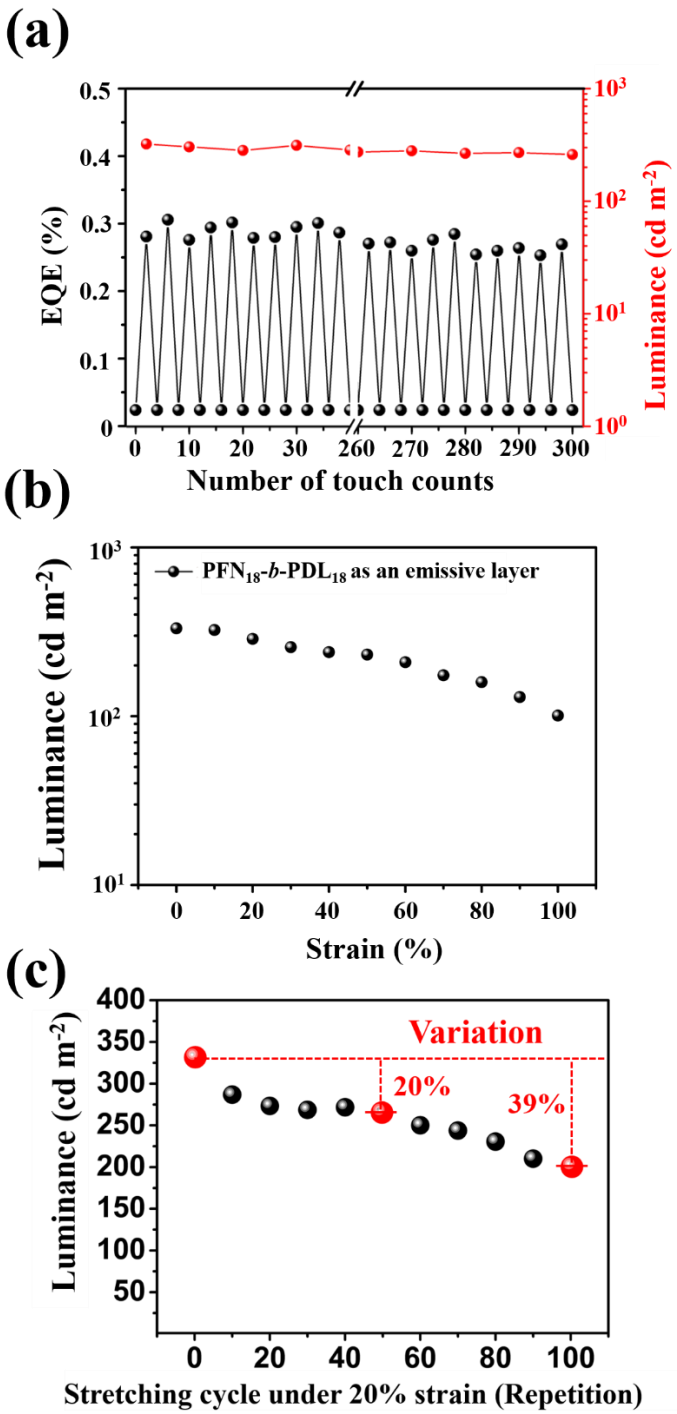

Figure 4.23. (a) The durable test of luminance and EQE characteristics and (b) luminance under a uniaxial strain from 0 to 100% of the touch-responsive LEDs using PFN_{18}-*b*-PDL_{13} as an emissive layer (under 19V). (c) Luminance-stretching cycle characteristics of the touch-responsive LEDs after repetitive stretching cycles at 20% strain.

4.4 Conclusion

In this chapter, the author successfully prepares a series of PF-based BCPs, namely PFN_{18}-*b*-PDL_n, PF_{18}-*b*-(PA-*alt*-EGE)$_{20}$, and PF_{18}-*b*-(AA-*alt*-EGE)$_{20}$ through a smart one-pot synthesis. A commercially available difunctional initiator is used for inducing both ROP and SCTP for PDL and PFN blocks, respectively. The smart polymerization procedure is utilized for quick and efficient synthesis of BCPs with various PDL lengths controlled by varying the polymerization time. Moreover, the author reveals that the BCP strategy can considerably enhance EBE compared to PFN due to the incorporation of a short insulating PDL segment. The PFN_{18}-*b*-PDL_n devices exhibit excellent radiative recombination because of their stable bound state induced by high EBE. Among BCPs, PFN_{18}-*b*-PDL_{13} achieves the highest EQE = 0.329%, which is 6 times higher than that of the PFN and PFO homopolymers. Therefore, highly stable and flexible touch-responsive LEDs with ultra-high efficiency are fabricated with PFN_{18}-*b*-PDL_{13}. The findings of this study reveal that conjugated BCPs with even a small coil block can enhance the performance of wearable optoelectronics.

4.5 References

1. Qiang, L.; Ma, Z.; Zheng, Z.; Yin, R.; Huang, W., Novel Photo-Crosslinkable Light-Emitting Rod/Coil Copolymers: Underlying Facile Material for Fabricating Pixelated Displays. *Macromolecular rapid communications* **2006,** *27* (20), 1779-1786.
2. Wang, J.-T.; Saito, K.; Wu, H.-C.; Sun, H.-S.; Hung, C.-C.; Chen, Y.; Isono, T.; Kakuchi, T.; Satoh, T.; Chen, W.-C. J. N. A. M., High-performance stretchable resistive memories using donor–acceptor block copolymers with fluorene rods and pendent isoindigo coils. **2016,** *8* (8), e298-e298.
3. Fischer, C. S.; Baier, M. C.; Mecking, S. J. J. o. t. A. C. S., Enhanced brightness emission-tuned nanoparticles from heterodifunctional polyfluorene building blocks. **2013,** *135* (3), 1148-1154.
4. Li, J.-J.; Wang, J.-J.; Zhou, Y.-N.; Luo, Z.-H. J. R. A., Synthesis and characterization of polyfluorene-based photoelectric materials: the effect of coil segment on the spectral stability. **2014,** *4* (38), 19869-19877.
5. Yu, Y.-Y.; Huang, C.-Y. J. J. o. N., Morphological Transformation and Photophysical Properties of Polyfluorene-Based Luminescent Rod-Coil Block Copolymers. **2016,** *2016*.
6. Zhao, X.; Deng, K.; Liu, F.; Zhang, X.; Yang, H.; Peng, J.; Liu, Z.; Ma, L.; Wang, B.; Wei, H. J. A. B. S.; Engineering, Fabrication of conjugated amphiphilic triblock copolymer for drug delivery and fluorescence cell imaging. **2018,** *4* (2), 566-575.
7. Deng, K.; Zhao, X.; Liu, F.; Peng, J.; Meng, C.; Huang, Y.; Ma, L.; Chang, C.; Wei, H. J. A. B. S.; Engineering, Synthesis of Thermosensitive Conjugated Triblock Copolymers by Sequential Click Couplings for Drug Delivery and Cell Imaging. **2019,** *5* (7), 3419-3428.
8. Chiu, Y.-C.; Chen, Y.; Kuo, C.-C.; Tung, S.-H.; Kakuchi, T.; Chen, W.-C. J. A. a. m.; interfaces, Synthesis, morphology, and sensory applications of multifunctional rod–coil–coil triblock copolymers and their electrospun nanofibers. **2012,** *4* (7), 3387-3395.
9. Jin, Z.; Fan, H., Self-assembly of nanostructured block copolymer nanoparticles. *Soft Matter* **2014,** *10* (46), 9212-9219.
10. Lee, Y.-H.; Yen, W.-C.; Su, W.-F.; Dai, C.-A., Self-assembly and phase transformations of π-conjugated block copolymers that bend and twist: from rigid-rod nanowires to highly curvaceous gyroids. *Soft Matter* **2011,** *7* (21), 10429-10442.
11. Saito, K.; Isono, T.; Sun, H.-S.; Kakuchi, T.; Chen, W.-C.; Satoh, T., Rod–coil type miktoarm star copolymers consisting of polyfluorene and polylactide: precise synthesis and structure–morphology relationship. *Polym. Chem.* **2015,** *6* (39), 6959-6972.
12. Kipp, D.; Mok, J.; Strzalka, J.; Darling, S. B.; Ganesan, V.; Verduzco, R., Rational Design of Thermally Stable, Bicontinuous Donor/Acceptor Morphologies with Conjugated Block Copolymer Additives. *ACS Macro Lett.* **2015,** *4* (9), 867-871.
13. Tao, Y.; Ma, B.; Segalman, R. A., Self-assembly of rod− coil block copolymers and their

application in electroluminescent devices. *Macromolecules* **2008,** *41* (19), 7152-7159.
14. Shaw, P. E.; Ruseckas, A.; Samuel, I. D., Exciton diffusion measurements in poly (3-hexylthiophene). *Adv. Mater.* **2008,** *20* (18), 3516-3520.
15. Sim, M.; Shin, J.; Shim, C.; Kim, M.; Jo, S. B.; Kim, J.-H.; Cho, K., Dependence of Exciton diffusion length on crystalline order in conjugated polymers. *J. Phys. Chem. C* **2014,** *118* (2), 760-766.
16. Hsieh, H. C.; Chen, J. Y.; Lee, W. Y.; Bera, D.; Chen, W. C., Stretchable fluorescent polyfluorene/acrylonitrile butadiene rubber blend electrospun fibers through physical interaction and geometrical confinement. *Macromol. Rapid Commun.* **2018,** *39* (5), 1700616.
17. Hsieh, H.-C.; Wu, N.; Chuang, T.-H.; Lee, W.-Y.; Chen, J.-Y.; Chen, W.-C., Eco-friendly Polyfluorene/Poly (butylene succinate) Blends and Their Electronic Device Application on Biodegradable Substrate. *ACS Appl. Polym. Mater.* **2020,** *2*, 2469–2476.
18. Tian, Y.; Chen, C.-Y.; Yip, H.-L.; Wu, W.-C.; Chen, W.-C.; Jen, A. K.-Y., Synthesis, nanostructure, functionality, and application of polyfluorene-block-poly (N-isopropylacrylamide) s. *Macromolecules* **2010,** *43* (1), 282-291.
19. Jiang, D.-H.; Kobayashi, S.; Jao, C.-C.; Mato, Y.; Isono, T.; Fang, Y.-H.; Lin, C.-C.; Satoh, T.; Tung, S.-H.; Kuo, C.-C. J. P., Light Down-Converter Based on Luminescent Nanofibers from the Blending of Conjugated Rod-Coil Block Copolymers and Perovskite through Electrospinning. **2020,** *12* (1), 84.
20. Huber, S.; Mecking, S. J. M., Straightforward Synthesis of Conjugated Block Copolymers by Controlled Suzuki–Miyaura Cross-Coupling Polymerization Combined with ATRP. **2019,** *52* (15), 5917-5924.
21. Hsieh, H.-C.; Hung, C.-C.; Watanabe, K.; Chen, J.-Y.; Chiu, Y.-C.; Isono, T.; Chiang, Y.-C.; Reghu, R. R.; Satoh, T.; Chen, W.-C. J. P. C., Unraveling the stress effects on the optical properties of stretchable rod-coil polyfluorene-poly (n-butyl acrylate) block copolymer thin films. **2018,** *9* (27), 3820-3831.
22. Au-Duong, A.-N.; Wu, C.-C.; Li, Y.-T.; Huang, Y.-S.; Cai, H.-Y.; Jo Hai, I.; Cheng, Y.-H.; Hu, C.-C.; Lai, J.-Y.; Kuo, C.-C. J. M., Synthetic Concept of Intrinsically Elastic Luminescent Polyfluorene-Based Copolymers via RAFT Polymerization. **2020**.
23. Kobayashi, S.; Fujiwara, K.; Jiang, D.-H.; Yamamoto, T.; Tajima, K.; Yamamoto, Y.; Isono, T.; Satoh, T., Suzuki–Miyaura Catalyst-Transfer Polycondensation of Triolborate-Type Fluorene Monomer: Toward Rapid Access to Polyfluorene-Containing Block and Graft Copolymers from Various Macroinitiators. *Polym. Chem.* **2020,** *00*, 1-3.
24. Kim, Y. Y.; Ree, B. J.; Kido, M.; Ko, Y. G.; Ishige, R.; Hirai, T.; Wi, D.; Kim, J.; Kim, W. J.; Takahara, A., High-Performance n-Type Electrical Memory and Morphology-Induced Memory-Mode Tuning of a Well-Defined Brush Polymer Bearing Perylene Diimide Moieties. *Adv. Electron. Mater.* **2015,** *1* (10), 1500197.
25. Lee, B.; Park, Y.-H.; Hwang, Y.-T.; Oh, W.; Yoon, J.; Ree, M., Ultralow-k nanoporous

organosilicate dielectric films imprinted with dendritic spheres. *Nat. Mater.* **2005,** *4* (2), 147-150.

26. Ree, B. J.; Satoh, Y.; Isono, T.; Satoh, T., Bicyclic Topology Transforms Self-Assembled Nanostructures in Block Copolymer Thin Films. *Nano Lett.* **2020,** *20* (9), 6520-6525.

27. Ree, M. J. M. r. c., Probing the Self-Assembled Nanostructures of Functional Polymers with Synchrotron Grazing Incidence X-Ray Scattering. *Macromol. Rapid Commun.* **2014,** *35* (10), 930-959.

28. Wang, H.; Zhang, X.; Wu, Q.; Cao, F.; Yang, D.; Shang, Y.; Ning, Z.; Zhang, W.; Zheng, W.; Yan, Y., Trifluoroacetate induced small-grained CsPbBr 3 perovskite films result in efficient and stable light-emitting devices. *Nat. Commun.* **2019,** *10* (1), 1-10.

29. Woo, H. C.; Choi, J. W.; Shin, J.; Chin, S.-H.; Ann, M. H.; Lee, C.-L., Temperature-dependent photoluminescence of CH3NH3PbBr3 perovskite quantum dots and bulk counterparts. *J. Phys. Chem. Lett.* **2018,** *9* (14), 4066-4074.

30. Janssen, R. A.; Nelson, J., Factors limiting device efficiency in organic photovoltaics. *Adv. Mater.* **2013,** *25* (13), 1847-1858.

31. Stranks, S. D.; Hoye, R. L.; Di, D.; Friend, R. H.; Deschler, F., The physics of light emission in halide perovskite devices. *Adv. Mater.* **2019,** *31* (47), 1803336.

32. Yang, B.; Han, K., Charge-carrier dynamics of lead-free halide perovskite nanocrystals. *Acc. Chem. Res.* **2019,** *52* (11), 3188-3198.

33. Maultzsch, J.; Pomraenke, R.; Reich, S.; Chang, E.; Prezzi, D.; Ruini, A.; Molinari, E.; Strano, M.; Thomsen, C.; Lienau, C., Exciton binding energies in carbon nanotubes from two-photon photoluminescence. *Phys. Rev. B* **2005,** *72* (24), 241402.

34. Cheng, B.; Li, T.-Y.; Maity, P.; Wei, P.-C.; Nordlund, D.; Ho, K.-T.; Lien, D.-H.; Lin, C.-H.; Liang, R.-Z.; Miao, X. J. C. P., Extremely reduced dielectric confinement in two-dimensional hybrid perovskites with large polar organics. **2018,** *1* (1), 1-8.

35. Lan, Z. A.; Zhang, G.; Chen, X.; Zhang, Y.; Zhang, K. A.; Wang, X., Reducing the Exciton Binding Energy of Donor–Acceptor-Based Conjugated Polymers to Promote Charge-Induced Reactions. *Angew.e Chem. Int.* **2019,** *58* (30), 10236-10240.

36. Wang, L.; McCleese, C.; Kovalsky, A.; Zhao, Y.; Burda, C., Femtosecond time-resolved transient absorption spectroscopy of CH3NH3PbI3 perovskite films: evidence for passivation effect of PbI2. *J. Am. Chem. Soc.* **2014,** *136* (35), 12205-12208.

37. Leng, M.; Yang, Y.; Chen, Z.; Gao, W.; Zhang, J.; Niu, G.; Li, D.; Song, H.; Zhang, J.; Jin, S. J. N. l., Surface passivation of bismuth-based perovskite variant quantum dots to achieve efficient blue emission. **2018,** *18* (9), 6076-6083.

Chapter 5

Conclusions

Polyfluorene-based (PF-based) conjugated block copolymers (BCPs) are emerging as a promising class of materials for understanding and controlling processes associated with light-emitting diodes (LEDs). The extensive interest in BCPs originates not only from their potential technological advantages but also from their ability to naturally self-assemble into periodic ordered nanostructures further affecting the performance of LEDs. Incorporating these self-assemble materials into optoelectronic device fabrication processes or directly into the device will lead to new insights into structure-property relationships and perhaps, ultimately, increases device efficiency. Flexible and wearable displays, one of the most desirable requisites of electronic devices, have emerged with rod-coil BCPs as a technology for their capability to revolutionize device and fashion industries in collaboration with state-of-the-art electronics. Nevertheless, challenges remain for the rod-coil BCP approaches, because rod-coil BCPs LEDs suffer from much lower performance than those fabricated on the fully conjugated copolymers. To achieve a fundamental comprehension of improving flexible LED performance by using rod-coil BCPs, a simple overview of the methods used and the expected benefits of PF-based rod-coil BCP in flexible LEDs is given in this dissertation. A summary of the important achievements and scientific insights from the present study is as follows:

Chapter 2 "Facile Preparation of Cu/Ag Core/Shell Nanofiber as High Flexible Transparent Conductive Electrodes for Polyfluorene Light-Emitting Diode Devices"

Novel transparent conductive electrodes (TCEs) with copper (Cu)/silver (Ag) nanofibers (NFs) with core/shell nanostructures for poly(9,9-di-*n*-octyl-2,7-fluorene) (PFO) light-emitting diode (LED) are successfully fabricated via using a combination of chemical reduction and electrospinning (ES). Although serval researchers have reported different materials, which have been identified as novel materials for replacing rigid indium tin oxide (ITO) and metal in TCEs, these TCEs suffer from practical disadvantages, such as extremely complicated process, expensive instrumentation, and unable to mass-produce. The electroless plating method to coat an Ag layer on the Cu-NFs, which is a facile and low-cost way to prepare TCEs. The metal NFs of different architectures exhibit various degrees of conductivity and follow the order random type > crossed type > aligned type, but the order with respect to transmittance (*T*) is inverse. The aligned type NFs exhibit a high *T* of 82%, and the random ones exhibit a low sheet resistance (*R*s) of 102 Ω sq^{-1} (the best value is 7.85 Ω sq^{-1}). The present study demonstrates that TCEs based on Cu/Ag core/shell NFs have considerable flexibility, transparency, and conductivity and can be applied to the flexible PFO LEDs, thus demonstrating their practical utility.

Chapter 3 "Light Down-Converter Based on the Blending of Polyfluorene Block Copolymers with Perovskite through Electrospinning"

A novel strategy for the preparation of high luminance light down-converter LED by

combining PFN_{24}-*b*-PBA_{90} rod-coil BCPs with perovskite quantum dots ($CsPbBr_3$ QDs), namely $CsPbBr_3$@PFN_{24}-*b*-PBA_{90} through electrospinning is demonstrated. The major drawback of utilizing PF homopolymer is its vulnerability when stretched due to its rigidity. To address this point, coil block PBA is incorporated into BCPs to enhance overall stretchability. By using $CsPbBr_3$@PFN_{24}-*b*-PBA_{90} NF film, the color-tunable light down-converter LEDs can be successfully fabricated using only a single layer on a commercial ultraviolet (UV) chip (λ_{max} = 380 nm) due to the energy transfer from commercial UV LED chip and PF-block (donor) to perovskite QD (acceptor). It is a novel and simple method to fabricate high luminance and color-tunable by blending perovskite in the polymer fiber. The results of the present study suggest that PF-based rod-coil BCPs have the potential to achieve high stretchability as well as favorable fluorescent properties for versatile applications that require outstanding optical properties.

Chapter 4 "Smart Synthesis of Polyfluorene-Based Block Copolymers Accelerates Design and Fabrication of Flexible Light-Emitting Diode Devices"

A series of PFN_{18}-*b*-PDL_n rod-coil BCPs are synthesized through a smart one-pot procedure that involves simple purification for fabricating touch-responsive LEDs. In PF-based rod-coil BCP, whose soft block has a high dielectric constant (ε), the screen effect is largely reduced, and the exciton binding energy (EBE) is higher than that in PFN homopolymer. As a result,

efficient radiative recombination and high photoluminescence quantum yield (PLQY) can be achieved, as clearly indicated from experimental data. Furthermore, PFN_{18}-*b*-PDL_{13} specifically exhibits external quantum efficiency (EQE) that is 6 times higher than PFN and PFO homopolymer. By using PF-based rod-coil BCP as an emissive layer, ultrahigh flexible and efficient light-emitting diode (LED) devices can be fabricated and showed the potential for the next generation of electronic applications.

In conclusion, the author demonstrates the TCEs based on Cu/Ag core/shell NFs have considerable flexibility, transparency, and conductivity and can be applied to the flexible PFO LEDs, thus demonstrating their practical utility, as shown in Chapter 2. However, the rigid PFO showed unfavorable to overall flexibility and performance of the device, which highlights the importance of research finding high PLQY and flexible emissive materials. To meet this issue, Chapter 3 exhibits PF-based rod-coil BCPs to achieve high stretchability as well as favorable fluorescent properties for versatile applications that require outstanding optical properties. Surprisingly, the PF-based rod-coil BCPs exhibit higher PLQY than their respective homopolymer. However, the specific discussions regarding this phenomenon has not been reported yet. Furthermore, the laborious rod-coil BCP synthetic procedures and the complexity of purification are limiting mass production. To address these limitations, Chapter 4 describes the smart one-pot synthesis to achieve impressive breakthroughs in forming diverse rod-coil

BCPs and further demonstrates the importance of robust stretchable wearable LED fabrication and wearable electronic fabrication. In addition, high PLQY can be achieved in rod-coil BCPs by using a low dielectric constant coil block. The results obtained from the present investigation offer detailed insight and fundamental comprehension of improving flexible LED performance by using PF-based rod-coil BCPs. Therefore, the author believes that the present dissertation offers better guidance to the fabrication of the PF-based BCPs, while leads to further development of highly stable and efficient LED based on the PF-based BCPs.